



VALIDATION OF TURBULENCE MODELS
FOR THE BEGGAR CODE
IN UNSTEADY FLOWS

THESIS

Kevin Gregory Storm, Second Lieutenant, USAF

AFIT/GAE/ENY/05-M22

DEPARTMENT OF THE AIR FORCE
AIR UNIVERSITY

AIR FORCE INSTITUTE OF TECHNOLOGY

Wright-Patterson Air Force Base, Ohio

APPROVED FOR PUBLIC RELEASE; DISTRIBUTION UNLIMITED.

The views expressed in this thesis are those of the author and do not reflect the official policy or position of the United States Air Force, Department of Defense, or the United States Government.

VALIDATION OF TURBULENCE MODELS
FOR THE BEGGAR CODE
IN UNSTEADY FLOWS

THESIS

Presented to the Faculty
Department of Aeronautics and Astronautics
Graduate School of Engineering and Management
Air Force Institute of Technology
Air University
Air Education and Training Command
In Partial Fulfillment of the Requirements for the
Degree of Master of Science in Aeronautical Engineering

Kevin Gregory Storm, B.S.
Second Lieutenant, USAF

March, 2005

VALIDATION OF TURBULENCE MODELS
FOR THE BEGGAR CODE
IN UNSTEADY FLOWS

Kevin Gregory Storm, B.S.
Second Lieutenant, USAF

Approved:

/signed/

11 Mar 2005

LtCol Raymond C. Maple, PhD (Chairman)

date

/signed/

11 Mar 2005

Dr Ralph A. Anthenien (Member)

date

/signed/

11 Mar 2005

Maj Richard J. McMullan, PhD (Member)

date

Abstract

Validation of the turbulence models in the CFD code Beggar for unsteady turbulent flow is discussed. Six validation cases of the code are considered, three cases with the intent of validating the code without the turbulence model and three cases to validate the turbulence model itself. The code validation cases include a vortex in an inviscid atmosphere, a laminar cylinder, and a laminar shock-tube. The turbulence model validation cases include a $2D$ oscillating airfoil, a $3D$ cylinder and a turbulent cavity. Finally, a more realistic simulation of a simplified store is examined. The turbulence models considered are the Baldwin-Lomax, Spalart-Allmaras, and a Detached Eddy Simulation (DES) model. The conclusions made deal with necessary prerequisites to properly simulating unsteady turbulent flow and model selection. The prerequisites necessary in the Beggar code are a second order temporal discretization and the calculation of at least three Newton dt-iterations per time step. The Baldwin-Lomax model was found to predict separation early, leading to a breakdown of the flow structure. The Spalart-Allmaras model was found to not properly simulate unsteady turbulent flow. A recommendation of whether to use the DES model was not made due to time and computational constraints and temporary problems within the Beggar code.

Acknowledgements

I would like to thank Dr Bobby Nichols, whose previous work is the foundation of this entire document. I would like to thank the Computational Aeromechanics Team at Eglin AFB, FLA. Especially Robert Moran and Bruce Jolly for their assistance in the operation of Beggar and Magdi Rizk and Alex Dobrinski for their insight into the the Beggar code. I would like to thank LtCol Raymond Maple for his assistance and guidance as my advisor in this research effort. Finally, I would like to thank my family and friends for seeing me through these turbulent times.

Kevin Gregory Storm

Table of Contents

	Page
Abstract	iv
Acknowledgements	v
List of Figures	viii
List of Tables	xiv
List of Abbreviations	xv
Nomenclature	xvi
I. INTRODUCTION	1
1.1 Research Goals	3
1.2 Prior Research	3
1.2.1 Beggar History	3
1.2.2 Other Validation Efforts	4
1.3 Research Approach	6
1.3.1 Non-Turbulent Study	6
1.3.2 Turbulent Study	7
1.3.3 Store Separation Study	7
1.4 Document Organization	8
II. BACKGROUND AND THEORY	9
2.1 General Aerodynamic Flow	9
2.2 Beggar Implementation	11
2.3 Turbulence	14
2.4 Turbulence Modeling	17
2.5 Baldwin-Lomax	18
2.6 Spalart-Allmaras	21
2.7 Detached Eddy Simulation	23
2.7.1 Beggar Implementation	23
III. NON-TURBULENT STUDY	25
3.1 Inviscid Convecting Vortex	26
3.1.1 Case Presentation	26
3.1.2 Results	29
3.2 Shock-Tube	40
3.2.1 Case Presentation	40
3.2.2 Results	41
3.3 2D Vortex Shedding Cylinder	45
3.3.1 Case Presentation	45
3.3.2 Results	47
3.4 Conclusions	52

	Page
IV. TURBULENT STUDY	53
4.1 2D Oscillating Airfoil	53
4.1.1 Case Presentation	53
4.1.2 Results	57
4.2 3D Vortex Shedding Cylinder	67
4.2.1 Case Presentation	67
4.2.2 Results	67
4.3 Turbulent Cavity	75
4.3.1 Case Presentation	75
4.3.2 Results	77
4.4 Conclusions	83
V. GENERIC STORE SIMULATION	84
5.1 Case Presentation	84
5.2 Results	85
VI. SUMMARY AND RECOMMENDATIONS	91
6.1 Summary	91
6.2 Recommendations	92
Appendix A. Results from Non-Turbulent Cases	93
A.1 Inviscid Convecting Vortex	93
A.2 2D Vortex Shedding Cylinder	112
Appendix B. Results from Turbulent Cases	117
B.1 Turbulent Cavity	117
Bibliography	127
Vita	130

List of Figures

Figure		Page
1	Velocity with respect to time at a point in turbulent flow.	15
2	Turbulent energy spectrum.	15
3	Initial vortex in the coarse 81x81 grid	28
4	Vortex - Initial Pressure Contours	30
5	Vortex - Steger-Warming - 1st Order Temporal - Pressure Contours After 6 Cycles	31
6	Vortex - Steger-Warming - 2nd Order Temporal - Pressure Contours After 6 Cycles	31
7	Vortex - Roe - 1st Order Temporal - Pressure Contours After 6 Cycles	32
8	Vortex - Roe - 2nd Order Temporal - Pressure Contours After 6 Cycles	32
9	Cycle vs Minimum Pressure - Coarse Grid	34
10	Cycle vs Minimum Pressure - Fine Grid	35
11	Cycle vs Δx - Roe - Coarse Grid - 1st Order Temporal	35
12	Cycle vs Δy - Roe - Coarse Grid - 1st Order Temporal	36
13	Cycle vs Δx - Roe - Coarse Grid - 2nd Order Temporal	36
14	Cycle vs Δy - Roe - Coarse Grid - 2nd Order Temporal	37
15	Cycle vs Δx - Steger-Warming - Coarse - 1st Order Temporal	37
16	Cycle vs Δy - Steger-Warming - Coarse Grid - 1st Order Temporal .	38
17	Cycle vs Δx - Steger-Warming - Coarse Grid - 2nd Order Temporal .	38
18	Cycle vs Δy - Steger-Warming - Coarse Grid - 2nd Order Temporal .	39
19	2D Viscous Shock-Tube Grid	40
20	Shock-Tube Density at Non-Dimensional Time $t = 0.2$	42
21	Zoomed in Image of Figure 20 at Trailing Edge of Expansion Fan . .	43
22	Shock-Tube Density at Non-Dimensional Time $t = 0.2$ - Halved Time Step comparison	43
23	Shock-Tube Density at Non-Dimensional Time $t = 0.2$ - Newton com- parison	44

Figure		Page
24	Maximum Error in Density vs Number of Newton dt-iterations	44
25	2D Vortex Shedding Laminar Cylinder grid.	46
26	Mach contours of vortex shedding laminar cylinder	48
27	Lift vs Time	49
28	PSD of St from Lift - Temporal Order Comparison	49
29	PSD of St from Lift - RHS Comparison	50
30	PSD of St from Lift - Roe - 1st Order Temporal	50
31	Average Peak Lift vs dt-iteration	51
32	NACA 0015 Grid	54
33	NACA 0015 Grid - Zoomed in on Trailing Edge	55
34	Cartesian Grid	55
35	$\alpha_o = 4.0^\circ$ - Lift Coefficient vs α	59
36	$\alpha_o = 4.0^\circ$ - Drag Coefficient vs α	60
37	$\alpha_o = 4.0^\circ$ - Pitching Moment Coefficient vs α	60
38	u Velocity - $\alpha = 5.22^\circ$ - Downstroke- Baldwin-Lomax	61
39	u Velocity - $\alpha = 5.22^\circ$ - Downstroke- Spalart-Allmaras	62
40	$\alpha_o = 4.0^\circ$ - Pitching Moment Coefficient vs α - Half Time Comparison	62
41	$\alpha_o = 11.0^\circ$ - Lift Coefficient vs α	63
42	$\alpha_o = 11.0^\circ$ - Drag Coefficient vs α	63
43	$\alpha_o = 11.0^\circ$ - Pitching Moment Coefficient vs α	64
44	Instantaneous Vorticity - $\alpha_o = 11.0^\circ$ - $\alpha = 13.97^\circ$ Downstroke - Baldwin-Lomax	64
45	Instantaneous Vorticity - $\alpha_o = 11.0^\circ$ - $\alpha = 13.97^\circ$ Downstroke - Spalart-Allmaras	65
46	Instantaneous Vorticity - $\alpha_o = 11.0^\circ$ - $\alpha = 13.97^\circ$ Downstroke - DES .	66
47	C_p vs Time	69
48	PSD of St	70
49	Instantaneous Total Pressure Plot - Baldwin-Lomax	70

Figure		Page
50	Instantaneous Total Pressure Plot - Spalart-Allmaras	71
51	Instantaneous Total Pressure Plot - DES	71
52	Instantaneous Vorticity Plot - Baldwin-Lomax	72
53	Instantaneous Vorticity Plot - Spalart-Allmaras	72
54	Instantaneous Vorticity Plot - DES	73
55	Velocity Parallel to the Cylinder - Baldwin-Lomax	73
56	Velocity Parallel to the Cylinder - Spalart-Allmaras	74
57	Velocity Parallel to the Cylinder - DES	74
58	Bay Grids	76
59	Sound Pressure Level Spectrum at the K16 Location - Medium Grid	78
60	Average Pressure Coefficient on the Cavity Ceiling - Coarse Grid . .	79
61	Average Pressure Coefficient on the Cavity Ceiling - Medium Grid . .	79
62	Average Pressure Coefficient on the Cavity Ceiling - Fine Grid	79
63	Vorticity - Baldwin-Lomax - Medium Cavity Grid	80
64	Vorticity - Spalart-Allmaras - Medium Cavity Grid	81
65	Vorticity - DES - Medium Cavity Grid	82
66	Initial Store Orientation	85
67	Roll Time History	87
68	Pitch Time History	87
69	Yaw Time History	87
70	Pressure at $t = 7.62 \times 10^{-3}$ sec - Baldwin-Lomax	88
71	Pressure at $t = 7.62 \times 10^{-3}$ sec - Spalart-Allmaras	88
72	Pressure at $t = 7.62 \times 10^{-3}$ sec - DES	89
73	Pressure Coefficient Along Store Body	89
74	Pressure Coefficient Along Midspan of Store Fin	90
75	Cycle vs Minimum Pressure - Coarse Grid	93
76	Cycle vs Minimum Pressure - Fine Grid	94
77	Cycle vs Minimum Pressure - Coarse Grid - Halved Time Step	94

Figure		Page
78	Cycle vs Minimum Pressure - Fine Grid - Halved Time Step	95
79	Cycle vs Δx - Roe - Coarse Grid - 1st Order Temporal	96
80	Cycle vs Δy - Roe - Coarse Grid - 1st Order Temporal	96
81	Cycle vs Δx - Roe - Coarse Grid - 2nd Order Temporal	97
82	Cycle vs Δy - Roe - Coarse Grid - 2nd Order Temporal	97
83	Cycle vs Δx - Steger-Warming - Coarse Grid - 1st Order Temporal .	98
84	Cycle vs Δy - Steger-Warming - Coarse Grid - 1st Order Temporal .	98
85	Cycle vs Δx - Steger-Warming - Coarse Grid - 2nd Order Temporal .	99
86	Cycle vs Δy - Steger-Warming - Coarse Grid - 2nd Order Temporal .	99
87	Cycle vs Δx - Roe - Fine Grid - 1st Order Temporal	100
88	Cycle vs Δy - Roe - Fine Grid - 1st Order Temporal	100
89	Cycle vs Δx - Roe - Fine Grid - 2nd Order Temporal	101
90	Cycle vs Δy - Roe - Fine Grid - 2nd Order Temporal	101
91	Cycle vs Δx - Steger-Warming - Fine Grid - 1st Order Temporal . . .	102
92	Cycle vs Δy - Steger-Warming - Fine - 1st Order Temporal	102
93	Cycle vs Δx - Steger-Warming - Fine - 2nd Order Temporal	103
94	Cycle vs Δy - Steger-Warming - Fine Grid - 2nd Order Temporal . .	103
95	Cycle vs Δx - Roe - Coarse Grid - 1st Order Temporal - Halved Time Step	104
96	Cycle vs Δy - Roe - Coarse Grid - 1st Order Temporal - Halved Time Step	104
97	Cycle vs Δx - Roe - Coarse Grid - 2nd Order Temporal - Halved Time Step	105
98	Cycle vs Δy - Roe - Coarse Grid - 2nd Order Temporal - Halved Time Step	105
99	Cycle vs Δx - Steger-Warming - Coarse Grid - 1st Order Temporal - Halved Time Step	106
100	Cycle vs Δy - Steger-Warming - Coarse Grid - 1st Order Temporal - Halved Time Step	106

Figure		Page
101	Cycle vs Δx - Steger-Warming - Coarse Grid - 2nd Order Temporal - Halved Time Step	107
102	Cycle vs Δy - Steger-Warming - Coarse Grid - 2nd Order Temporal - Halved Time Step	107
103	Cycle vs Δx - Roe - Fine Grid - 1st Order Temporal - Halved Time Step	108
104	Cycle vs Δy - Roe - Fine Grid - 1st Order Temporal - Halved Time Step	108
105	Cycle vs Δx - Roe - Fine Grid - 2nd Order Temporal - Halved Time Step	109
106	Cycle vs Δy - Roe - Fine Grid - 2nd Order Temporal - Halved Time Step	109
107	Cycle vs Δx - Steger-Warming - Fine Grid - 1st Order Temporal - Halved Time Step	110
108	Cycle vs Δy - Steger-Warming - Fine - 1st Order Temporal - Halved Time Step	110
109	Cycle vs Δx - Steger-Warming - Fine - 2nd Order Temporal - Halved Time Step	111
110	Cycle vs Δy - Steger-Warming - Fine Grid - 2nd Order Temporal - Halved Time Step	111
111	PSD of St for Lift - Roe - 1st Order Temporal	112
112	PSD of St for Lift - Roe - 2nd Order Temporal	113
113	PSD of St for Lift - Steger-Warming - 1st Order Temporal	113
114	PSD of St for Lift - Steger-Warming - 2nd Order Temporal	114
115	Average Peak Drag vs dt-iteration	114
116	Average Drag vs dt-iteration	115
117	Average Peak Lift vs dt-iteration	115
118	Average Strouhal Number from Lift vs dt-iteration	116
119	Sound Pressure Level Spectrum at the K16 Location - Coarse Grid	117
120	Sound Pressure Level Spectrum at the K16 Location - Medium Grid	118
121	Sound Pressure Level Spectrum at the K16 Location - Fine Grid	118

Figure		Page
122	Sound Pressure Level Spectrum at the K18 Location - Coarse Grid .	119
123	Sound Pressure Level Spectrum at the K18 Location - Medium Grid	119
124	Sound Pressure Level Spectrum at the K18 Location - Fine Grid . . .	120
125	Vorticity - Baldwin-Lomax - Medium Cavity Grid	120
126	Vorticity - Spalart-Allmaras - Medium Cavity Grid	121
127	Vorticity - DES - Medium Cavity Grid	122
128	Vorticity - Baldwin-Lomax - Fine Cavity Grid	123
129	Vorticity - Spalart-Allmaras - Fine Cavity Grid	124
130	Vorticity - Baldwin-Lomax - Fine Cavity Grid - Front	125
131	Vorticity - Spalart-Allmaras - Fine Cavity Grid - Front	126

List of Tables

Table		Page
1	Test cases	6
2	Inviscid convecting vortex initial conditions - non-dimensional values	27
3	Shock-tube example initial conditions - non-dimensional values	41
4	Vortex shedding laminar cylinder example initial conditions	45
5	2D oscillating airfoil example initial conditions	54
6	Average computation time for various turbulence models for the oscillating airfoil case	59
7	Vortex shedding turbulent cylinder example initial conditions	67
8	Force coefficient and Strouhal number data	68
9	Average computation times for various turbulence models for the 3D cylinder case	69
10	Turbulent cavity grid specifications	75
11	Turbulent cavity example initial conditions	75
12	Average computation times for various turbulence models for the turbulent cavity case	78
13	Store jettison initial conditions	84
14	Store jettison time step per iteration	85
15	Wall clock times for various turbulence models for the store jettison case	86

List of Abbreviations

Abbreviation		Page
AFSEO	Air Force Seek Eagle Office	1
AFB	Air Force Base	1
USAF	United States Air Force	1
CFD	Computational Fluid Dynamics	1
CAT	Computational Aeromechanics Team	1
DES	Detached Eddy Simulation	1
RANS	Reynolds Averaged Navier-Stokes	3
LES	Large Eddy Simulation	3
DNS	Direct Numerical Simulation	3
RHS	right hand side	12
PSD	Power Spectrum Density	47

Nomenclature

α	angle of attack	7
\bar{U}	contravariant velocity	9
\mathbf{g}	acceleration due to gravity	11
δ_{ij}	Kronecker delta	11
ϵ	dissipation	16
η	Kolmogorov length	16
Γ	vortex strength	27
λ	coefficient of bulk viscosity	11
λ	period	45
\mathcal{V}	volume	9
ν	viscosity	16
ρ	density	11
A	area	11
a	speed of sound	10
D	diameter	45
E_t	total energy	11
f	frequency	14
M	Mach Number	45
R	distance from vortex center	27
R_c	core radius of vortex	27
Re	Reynolds number	16
Re_t	turbulent Reynolds number	16
S_{ij}	strain rate tensor	18
St	Strouhal Number	45
U	freestream velocity	45
u, v, w	cartesian velocity components	11
V	velocity	11

VALIDATION OF TURBULENCE MODELS

FOR THE BEGGAR CODE

IN UNSTEADY FLOWS

I. INTRODUCTION

The Air Force Seek Eagle Office (AFSEO), Eglin Air Force Base (AFB), FL, is the United States Air Force (USAF) authority for weapons certification efforts. AFSEO performs test and evaluation for aircraft/store compatibility certification and uses Computational Fluid Dynamics (CFD) to support this process. The CFD code that the Computational Aeromechanics Team (CAT) has produced and implements is Beggar. Determining the flow about an aircraft/store combination can be extremely difficult. Complicated geometry such as pylons, launchers, and internal weapons bays can create severe acoustic and aerothermodynamic environments, which are challenging to simulate numerically. The additional challenge of rapidly and accurately simulating the trajectory of a store separation in a high-volume simulation environment is beyond the capabilities of most CFD programs. Beggar was specifically designed to excel under these conditions.

The USAF requirement for numerous, simultaneous and quick-reaction solutions for a wide variety of stores and aircraft increases the need for a fast and simple turbulence model. For this reason, the CAT has used the Baldwin-Lomax (1) algebraic model for most of its turbulent simulations. Although the CAT believes that the Baldwin-Lomax model has provided good results for their applications, industry has been moving towards more sophisticated models, such as the Spalart-Allmaras(34) one-equation model and the $k - \epsilon$ and $k - \omega$ (46) two-equation models.

After an initial evaluation of turbulence models, the CAT recently chose to include a Spalart-Allmaras one-equation model with the option for Detached Eddy Simulation (DES) in the Beggar code. This research effort will address the validation of the new model and will compare Spalart-Allmaras and Baldwin-Lomax results for a variety of simple test cases. In addition, a sample store will be considered with both turbulence models. Conclusions will

be drawn on the abilities of the Baldwin-Lomax and Spalart-Allmaras models to properly simulate store separation problems.

As an algebraic model, Baldwin-Lomax does not include any additional differential equations to solve for the Reynolds stresses (39). This makes it a computationally inexpensive model, which is a desirable quality for a production engineering code. A detailed description can be found in Section 2.5. Baldwin-Lomax has been shown to properly simulate flat plate boundary layers(1). Although it has also been noted that algebraic models are unreliable for separation flow(45), comparisons with measurements from two experiments show agreement in the prediction of separation and reattachment points within about one boundary-layer thickness(1). Baldwin-Lomax has also proven itself excellent for attached boundary layers, however it is not applicable to free-shear flows.

Because it does not include additional differential equations, the Baldwin-Lomax model cannot account for turbulent transport. In some cases, however, turbulent viscosity which exists upstream from a point may significantly influence the solution at that point. Without transport, the solution will be poor. A simple example of this is a circular arc bump in a two-dimensional channel. Baldwin-Lomax predicts almost no eddy viscosity on the bump where models with transport show significant eddy viscosity over the bump(19). This problem may also be present during store separation when stores at high angles of attack experience flow separation. In some cases however, such as attached boundary layer flows, Baldwin-Lomax can give as good if not better results than more complex models.

The one-equation Spalart-Allmaras model includes a transport equation derived using empiricism and arguments of dimensional analysis(34). For more details on the implementation of Spalart-Allmaras, see reference (34). Spalart-Allmaras is a relatively fast and numerically forgiving model. It was made with airfoils in mind. For other cases, specifically round jets, Spalart-Allmaras may not perform well(33). The Spalart-Allmaras model predicts skin friction for attached boundary layers as well as algebraic models. With the exception of jets, Spalart-Allmaras also predicts free-shear flows well.(45) For attached flow, the Baldwin-Lomax model in Beggar should perform as well as, if not better than, the Spalart-Allmaras model. For free-shear, such as flow over a cavity, we would expect the Spalart-Allmaras model to outperform Baldwin-Lomax.

Both the Baldwin-Lomax and Spalart-Allmaras models are Reynolds Averaged Navier-Stokes (RANS) models which use temporal averaging. Large Eddy Simulation (LES) is an alternate modeling approach that uses spatial averaging. Since large eddies cannot form near walls, LES does not perform well near walls without refining the grid to a Direct Numerical Simulation (DNS) scale. However, in the wake region, LES performs well. Baldwin-Lomax and Spalart-Allmaras perform well near walls, but since they are based on the distance from the wall they tend to not perform well in wake regions. The DES model attempts to combine the best of the two models. It implements the RANS model, but adds spatial filtering to allow direct calculation of large eddies in the wake.

1.1 *Research Goals*

The main goal of this research is to determine which turbulence model, Baldwin-Lomax, Spalart-Allmaras, or DES, will perform best for the CAT. To ensure that model can function, the following prerequisite options will be investigated:

1. 1st or 2nd order temporal discretization
2. Roe or Steger-Warming method for calculating fluxes
3. Number of Newton dt-iterations to perform per time step

Additional considerations while evaluating the previous options are artificial dissipation, how well calculated data matches experiment or theoretical data, and cpu-time required to perform the computation. For example, if the DES marginally outperforms the Baldwin-Lomax model, but takes three times the cpu-time, using DES would not be advisable in a production code such as Beggar.

1.2 *Prior Research*

1.2.1 Beggar History. Being a production code, there has been a fair amount already written about Beggar(4, 6, 12, 11, 14, 26, 28, 29, 30, 42). Rizk, Ellison, and Prewitt(30) give a good overview of the utility of Beggar. Beggar has been designed primarily to calculate flow interactions with moving rigid bodies, where the bodies may also interact. To accomplish this, Beggar uses an overset, or “Chimera”, grid system. Each object has its own grids with its own mass. Some grid dynamics may be set by the user. For example,

a three grid system includes a store with a fin falling in a large cartesian background grid. The user may specify that the fin grid will stay attached to the store grid. Furthermore, the user may specify that while staying attached, the fin grid will rotate about a specified axis, to pitch the fin for example. Beggar then determines the best points that each interpolation cell should get information from in each overset grid.

Westmoreland(42) discusses a comparison between using inviscid and viscous solvers to simulate store separations. Westmoreland simulated a jettison flight test of the sample store. He found that when the two solvers were run on stationary stores, substantial differences in aerodynamic loads were found in areas of separation and boundary layer growth. However, when the store was released, the inertial forces and externally applied loads were two orders of magnitude larger than the aerodynamic forces. Therefore the trajectory of the store was not influenced by the choice of using an inviscid or viscous solver. Noack and Jolly(26) obtained similar results simulating the release of a JDAM from an F-18C aircraft.

If the major choice of either an inviscid and viscous solver does not change the trajectory of a store, there is little chance that the choice of which turbulence model to use will have any other effect besides a dramatic increase in the required computing resources. The case of store trajectory or release is not the only situation that the AFSEO simulates, however. There are other cases, such as a store falling from a bay, where aerodynamic forces will have significant effects, in which this analysis have more direct applicability.

1.2.2 Other Validation Efforts. This document closely follows the turbulence model validation methods of Dr Robert Nichols(22) . Nichols stresses that before a turbulence model can be validated, the Navier-Stokes solver must be tested to ensure that the code has the capability to properly simulate a time accurate calculation. Dr Nichols places large emphasis on ensuring that no solver component has too much artificial dissipation. He has validated codes that use a Newton iteration time step method similar to Beggar. When validating these codes, many simulations have been run while varying the number of Newton dt-iterations to determine the minimum number required to accurately compute a time accurate simulation. Nichols concludes that to simulate a time accurate flow the following solver options are necessary:

1. Second order time derivatives: to lower numerical dissipation
2. Numerical flux algorithms with low dissipation: to reduce numerical dissipation
3. Subiteration scheme to improve local convergence: to allow larger time steps
4. A rapidly converging inner algorithm: to reduce cpu-time

Test cases to validate the DES model have been taken from references (23) and (21). In reference (23) a two dimensional oscillating pitching airfoil and a turbulent cavity are both examined. The oscillating airfoil is a NACA-0015 oscillating $\pm 4.2^\circ$ around an angle of attack of $\alpha = 11^\circ$ at a Reynolds number of $Re = 1.95 \times 10^6$. At these conditions, separation occurs during the downstroke cycle. Using a time step of 2.2×10^{-5} seconds, Nichols and Nelson found that the RANS turbulence models did not show any signs of shedding eddies, while the DES model did have shedding eddies. Similar effects were found in the turbulent cavity, where much more unsteady motion was apparent with the DES model than with the RANS model.

The test case taken from reference (21) is a 3D circular cylinder in cross-flow. Nichols attempts a grid convergence study, but notes that the finer a grid is, the smaller the turbulent length scales are which can be captured by the grid. This continues until the smallest of the turbulent length scales is reached. Currently, it is not feasible computationally to arrive at grids this fine. Therefore, a true grid convergence study could not have been performed. To attempt to check grid convergence, the average drag coefficient was recorded for three cylinder grids of varying levels of refinement. Nichols found that the DES model did not reach grid convergence with the three grids. In his temporal study, Nichols found that 200 time steps per shedding frequency are necessary for temporal accuracy using second order temporal discretization and a hybrid RANS/LES model. Similar to the turbulent cavity and oscillating airfoil, Nichols found that the LES model showed weak eddies in the far wake where the RANS models damped them out.

In another study, Nichols and Nelson(18) studied the effectiveness of a hybrid RANS/LES model they developed and made comparisons to the DES model. Their model implemented a $k - \epsilon$ model to account for subgrid scale turbulence. The test case in (18) was a compressible mixing layer where one layer was subsonic and the other was supersonic. Nichols and Nelson found that both the Nichols-Nelson and DES models showed drastic improvements

over the RANS models. Their results matched well with traditional LES models. They would not make further conclusions, as no single source of error could be identified.

Séror, Rubin, Peigin, and Epstein(32) discussed the validation of a Spalart-Allmaras turbulence model in a CFD code called “NES”. Their paper provides insight into validating the Spalart-Allmaras model without being overshadowed by the validation of the DES model. Similar to Beggar, the default turbulence model in NES was Baldwin-Lomax. Due to the difficulty in the fine grid resolution required by Baldwin-Lomax and the poor results it gave, Séror et al. decided to include the Spalart-Allmaras model. The test case they ran was a 2D RAE2822 supercritical airfoil at transonic flight conditions. Séror et al found that the Spalart-Allmaras model more accurately predicted the shock location than the Baldwin-Lomax model, and therefore improved the prediction of lift and drag. They also noted that there was much variation in the wake between the two models.

1.3 Research Approach

Validation of the additional turbulence models is broken down into two main components: a non-turbulent study and a turbulent study. The individual cases are shown in Table 1.

Table 1: Test cases

Case	Study
Convecting Vortex	Non-Turbulent
Shock-Tube	Non-Turbulent
2D Vortex Shedding Cylinder	Non-Turbulent
2D Oscillating Airfoil	Turbulent
3D Vortex Shedding Cylinder	Turbulent
Turbulent Cavity	Turbulent

In addition to these problems, the turbulence models will be applied to a store separation problem. Results will be used to determine the effects of using one-equation or algebraic turbulence models on simulating store separation.

1.3.1 Non-Turbulent Study. The non-turbulent study includes three test cases including a convecting vortex, a shock-tube, and a 2D vortex shedding cylinder. These cases are presented in order of difficulty.

The first case examined in the process of validating the turbulence model is a vortex convecting in an inviscid atmosphere. The inviscid convecting vortex is a quick simulation to run to check the numerical dissipation in each component of the code.

The shock-tube and $2D$ cylinder cases are simulated with the intention of determining the proper number of Newton dt-iterations to use. Both of these cases are quick to solve, allowing many different solver option combinations to be simulated.

1.3.2 Turbulent Study. The turbulent study has three test cases consisting of a $2D$ oscillating airfoil, a $3D$ vortex shedding cylinder, and a turbulent cavity.

The first turbulent case is a simple oscillating $2D$ airfoil. Two initial angle's of attack, α_o , are examined, $\alpha_o = 4.0^\circ$ and $\alpha_o = 11^\circ$. With the $\alpha_o = 4^\circ$, the angle of attack is always small enough that the flow remains attached to the airfoil throughout the simulation. This case will be used as another check to see that the solver can accurately model a time accurate simulation. The larger α_o will have separation off the top of the airfoil, which will provide insight into the turbulence models effect on separated flow.

A vortex shedding turbulent cylinder is more difficult than the $2D$ case. With $Re > 180$, the flow can no longer be approximated as $2D$. Numerical data will be compared to experimental data.

An unsteady simulation of the Weapons Internal Carriage and Separation (WICS) weapons bay will also be simulated. Experimental data has been gathered at two specific points inside the cavity. Care will be taken to ensure that the CFD grid will have a data point that matches where the experimental data was taken. CFD data will then be compared to the experimental data. A grid convergence study will be performed for this case.

1.3.3 Store Separation Study. Although important for validation, the previous cases are all very simple, and do not apply directly to everyday production simulations. To have some idea of the effects that the different turbulence models will have on a more realistic case, a sample store jettison will be simulated. As the turbulence model will have the most effect on the store when inertial effects are minimal, the initial motion of a store falling from rest will be considered separate from when the store has significant inertia. The

time step will then be gradually increased to allow the store to move a noticeable distance in a reasonable amount of time steps.

1.4 Document Organization

First a background will be presented to familiarize the reader with the terminology used in this document. Chapter II will start with the governing equations of aerodynamic flow. Then a description of how Beggar implements these equations is given. A brief introduction to turbulence follows, ending with how turbulence is modeled in CFD codes. Chapter III is dedicated to checking Beggar to ensure it has the capability of properly simulating time accurate flow. Results will be given along with the presentation of the case. When that has been done, the turbulence validation cases will be presented in Chapter IV. Again, results will be included with the presentation of the case. Chapter V will present the sample store jettison simulation and results. Finally, some conclusions and recommendations will be given in Chapter VI.

II. BACKGROUND AND THEORY

2.1 General Aerodynamic Flow

For most of the test cases used to validate the new turbulence models in the Beggar code, the Navier-Stokes equations will be used to solve the flow physics.

Historically speaking, the Navier-Stokes equations are the viscous conservation of momentum equations derived from Newton's second law and the deformation law for a newtonian fluid(43). However, in CFD the name Navier-Stokes is given to the set of equations including the conservation of mass, momentum and energy. The Beggar code is a finite volume solver, which uses the integral form of the Navier-Stokes equations:

$$\int_{\mathcal{V}} \frac{\partial Q}{\partial t} d\mathcal{V} + \int_A (F_c - F_v) dA = 0 \quad (1)$$

where

$$Q = \begin{Bmatrix} \rho \\ \rho u \\ \rho v \\ \rho w \\ E_t \end{Bmatrix}, \quad F_c = \begin{Bmatrix} \rho U \\ \rho U u + p n_x \\ \rho U v + p n_y \\ \rho U w + p n_z \\ (E_t + p)U \end{Bmatrix}, \quad F_v = \begin{Bmatrix} 0 \\ [\tau^T \cdot \hat{n}] \\ \theta_x n_x + \theta_y n_y + \theta_z n_z \end{Bmatrix},$$

and

$$\theta_i = u_j \tau_{ij} + k \frac{\partial T}{\partial x_i} \quad (2)$$

is the work done by the viscous stresses and the heat conduction of the fluid(2), $U = \mathbf{V} \cdot \hat{n}$ is the contravariant velocity, and τ is the stress tensor defined from the deformation law for a Newtonian fluid given by:

$$\tau_{ij} = \mu \left(\frac{\partial u_i}{\partial x_j} + \frac{\partial u_j}{\partial x_i} \right) + \delta_{ij} \lambda \nabla \mathbf{V} \quad (3)$$

which, using Stokes hypothesis ($\lambda = -\frac{2}{3}\mu$), reduces to:

$$\tau_{ij} = \mu \left(\frac{\partial u_i}{\partial x_j} + \frac{\partial u_j}{\partial x_i} - \frac{2}{3} \delta_{ij} \nabla \mathbf{V} \right) \quad (4)$$

Equation 4 is valid for fluids, including most gases, with the following properties as noted by Stokes(43):

1. There is a linear relationship between stress and strain.
2. An isotropic fluid is assumed.
3. As strain rates approach zero, the shear stresses will approach zero and the normal stresses will equal the static pressure
4. Body forces are absent.

While Beggar uses dimensional quantities to calculate body-to-body and flow-to-body interactions, the flow solver is non-dimensional. To non-dimensionalize the Navier-Stokes equations, the values shown in Equation 5 are inserted into Equation 1. The non-dimensional quantities in Equation 5 are represented with an asterisk.

$$\begin{aligned} \rho &= \rho^* \rho_\infty & E_t &= E_t^* \rho_\infty a_\infty^2 & p &= p^* \rho_\infty a_\infty^2 & t &= t^* \frac{L_{\text{ref}}}{a_\infty} \\ u &= u^* a_\infty & v &= v^* a_\infty & w &= w^* a_\infty \end{aligned} \tag{5}$$

Situations exist where viscosity does not play a significant role in determining the flow properties. For example, in high Reynolds number flows, the inertial effects outweigh the viscous effects. In these cases viscosity is only important in a thin layer that lies on body surfaces. The region outside of this boundary layer may be treated as inviscid with no spatial temperature gradient effects. For these situations, the Navier-Stokes equations may be simplified by eliminating all viscous terms, which results in the Euler equations. The Euler equations are:

$$\int_{\mathcal{V}} \frac{\partial Q}{\partial t} d\mathcal{V} + \int_A F_c dA = 0 \tag{6}$$

where F_c and Q are the same as in Equation 1. The convecting vortex case is solved with the Euler equations in place of the Navier-Stokes equations. The fact that the Euler equations do not include any effects from viscosity will be exploited to help determine which CFD

solver options to use. Further discussion of the convecting vortex case can be found in Section 3.1.

The equations described above are the basis of general aerodynamic flow. The Navier-Stokes equations include everything needed to solve turbulent flow. However, to solve for turbulent flow using only the Navier-Stokes equations is very problematic and is rarely done. This is described in Section 2.4.

2.2 Beggar Implementation

The Navier-Stokes equations (Equation 1) are continuous and can be solved at all points in a flow at all times. However, an exact general solution to the Navier-Stokes equations has not been found and is not expected to be found any time soon. Therefore, they are solved numerically. To do this, the Navier-Stokes equations are discretized to be solved at specific times and locations. An implicit discretization of Equation 1 is given by:

$$\frac{\partial Q^{n+1}}{\partial t} \mathcal{V} + \sum_i (F_{c_i}^{n+1} - F_{v_i}^{n+1}) |A_i| = 0 \quad (7)$$

where $\frac{\partial Q^{n+1}}{\partial t}$ is the time discretization of the the change in the conserved variables Q in the cell volume \mathcal{V} with respect to time and the second term is the sum of the fluxes through the sides of the cell. Superscript n is the specific time step. It is difficult to compute the fluxes at time $n + 1$. To simplify the computation, the fluxes are linearized in time which results in(15):

$$F_c^{n+1} = F_c^n + \frac{\partial F_c}{\partial Q} \Delta Q^{n+1} \quad (8)$$

$$F_v^{n+1} = F_v^n + \frac{\partial F_v}{\partial Q} \Delta Q^{n+1} \quad (9)$$

Substituting equations 8 and 9 into equation 7 gives

$$\frac{\partial Q^{n+1}}{\partial t} \mathcal{V} + \Sigma \left(\frac{\partial F_c}{\partial Q} - \frac{\partial F_v}{\partial Q} \right) \Delta Q^{n+1} |A| + \Sigma (F_c^n - F_v^n) |A| = 0 \quad (10)$$

Pulling $|A|$ into F and simplifying gives

$$\frac{\partial Q^{n+1}}{\partial t} \mathcal{V} + \left(\frac{\partial \mathcal{R}}{\partial Q} \right)^n \Delta Q^{n+1} = -\mathcal{R}^n \quad (11)$$

where $\frac{\partial Q^{n+1}}{\partial t}$ is the time discretization of the conserved variables, $\frac{\partial \mathcal{R}}{\partial Q}$ is the implicit operator, or Jacobian, which is derived using first order Steger-Warming fluxes (30), and \mathcal{R}^n is the explicit term commonly referred to as the “right hand side” (RHS)

Two different time discretizations are compared in this study, the first order backward Euler time discretization and the second order three point backward time discretization. The backward Euler time discretization method is given as(30):

$$\frac{\partial Q^{n+1}}{\partial t} = \frac{Q^{n+1} - Q^n}{\Delta t} \quad (12)$$

and the three point backward time(8) discretization is given as:

$$\frac{\partial Q^{n+1}}{\partial t} = \frac{3Q^{n+1} - 4Q^n + Q^{n-1}}{2\Delta t} \quad (13)$$

The three point backwards time discretization is a higher order and generally more accurate method than the backward Euler time, but it requires storing all of the conserved variables for the two previous time steps whereas the backward Euler time method only requires storing the previous time step.

Two different methods for calculating the right hand side are included in Beggar, and each will be tested; the second order Roe(31) and second order Steger-Warming(36) methods. Both of these methods are flux splitting methods. The Steger-Warming method splits the fluxes into negative and positive contributions based on eigenvalues. The Roe method(2) is an approximate Riemann solver that splits the difference of the fluxes.

Accurately calculating each time step is critical to unsteady flows. To ensure that each time step has been computed accurately, Beggar solves a user specified number of Newton dt-iterations for each time step. Newton’s method(44) for a vector function $G(x) = 0$ is given as:

$$G'(x^m)(x^{m+1} - x^m) = -G(x^m) \quad (14)$$

where superscript m is the Newton dt-iteration and $G'(x)$ is the Jacobian matrix given by:

$$G'(x) = \begin{bmatrix} a_{11}(x) & a_{12}(x) & \dots & a_{1,k}(x) \\ a_{21}(x) & a_{22}(x) & \dots & a_{2,k}(x) \\ \cdot & \cdot & & \\ \cdot & \cdot & & \\ \cdot & \cdot & & \\ a_{k1}(x) & a_{k2}(x) & \dots & a_{k,k}(x) \end{bmatrix} \quad (15)$$

where

$$a_{ij}(x) = \frac{\partial G_i(x)}{\partial x_j}. \quad (16)$$

Rearranging Equation 11 to resemble Equation 14 leads to:

$$\left(\frac{\partial R}{\partial Q}\right)^{n,m} \Delta Q^{n+1,m+1} = - \left[\mathcal{V} \frac{\partial Q^{n+1,m}}{\partial t} + R^{n,m} \right] \quad (17)$$

where

$$\Delta Q^{n+1,m+1} = Q^{n+1,m+1} - Q^{n+1,m} \quad (18)$$

To solve for $Q^{n+1,m+1}$, the $\Delta Q^{n+1,m+1}$ term must be isolated. This would involve inverting the Jacobian, whose dimensions may be on the order of millions. Inverting a matrix this large is intractable. Beggar avoids inverting the Jacobian by solving for $Q^{n+1,m+1}$ iteratively using the Symmetric Gauss-Seidel method. The Gauss-Seidel method solves the equation:

$$[A]\mathbf{x} = \mathbf{b} \quad (19)$$

for \mathbf{x} iteratively by breaking $[A]$ into an upper and a lower triangle and solving

$$x_i^{k+1} = b_i - L_i(\mathbf{x}^{k+1}) - U_i(\mathbf{x}^k) \quad (20)$$

where

$$L_i(\mathbf{x}^{k+1}) = \sum_{j=1}^{i-1} A_{i,j} x_j^{k+1} \quad (21)$$

and

$$U_i(\mathbf{x}^k) = \sum_{j=i+1}^{j_{max}} A_{i,j} x_j^k \quad (22)$$

where $k + 1$ implies an updated value. Alternating starting from the first element and the last element makes the process “symmetric.” The Symmetric Gauss-Seidel iterations are hereafter referred to as inner iterations. Equation 20 is solved iteratively until convergence criteria is met or the user set maximum number of Symmetric Gauss-Seidel iterations is computed.

2.3 Turbulence

Before turbulence modeling is discussed, a brief introduction to turbulence is presented. Turbulence is an important aspect of computational fluid dynamics since most engineering flows are turbulent. In non-turbulent flows, random fluctuations in the flow are damped out by viscous forces. In turbulent flow, the inertial forces overpower the viscous forces and the random fluctuations are no longer damped out, and actually grow. These fluctuations become an important characteristic of the flow, communicating with neighboring fluctuations and creating vortices of different scales, which also communicate with each other via an energy cascade.

Figure 1 shows a typical time history of velocity measured at a single point in a turbulent flow. It illustrates the different scales that are present in a turbulent flow. There is a lot of high frequency turbulence which appears as noise in the figure. If the sampling rate was reduced to filter out the high frequency turbulence, the general shape of the curve would still remain. This shape would be the largest turbulent scale, known as the integral scale. By sampling more frequently, smaller patterns will appear on the larger shape, similar to zooming in on a fractal. There is a limit when sampling more frequently will not produce any more patterns and the curve will smooth out. At this sampling rate the smallest turbulent scale, known as the Kolmogorov scale, can be determined.

Figure 2 displays important characteristics of the different length scales. On the abscissa is the frequency, f , which is inversely proportional to wavelength. Therefore, the smaller the abscissa value, the larger the length scale. From largest to smallest, the three main turbulent length scales are the integral scale, the Taylor scale, and the Kolmogorov

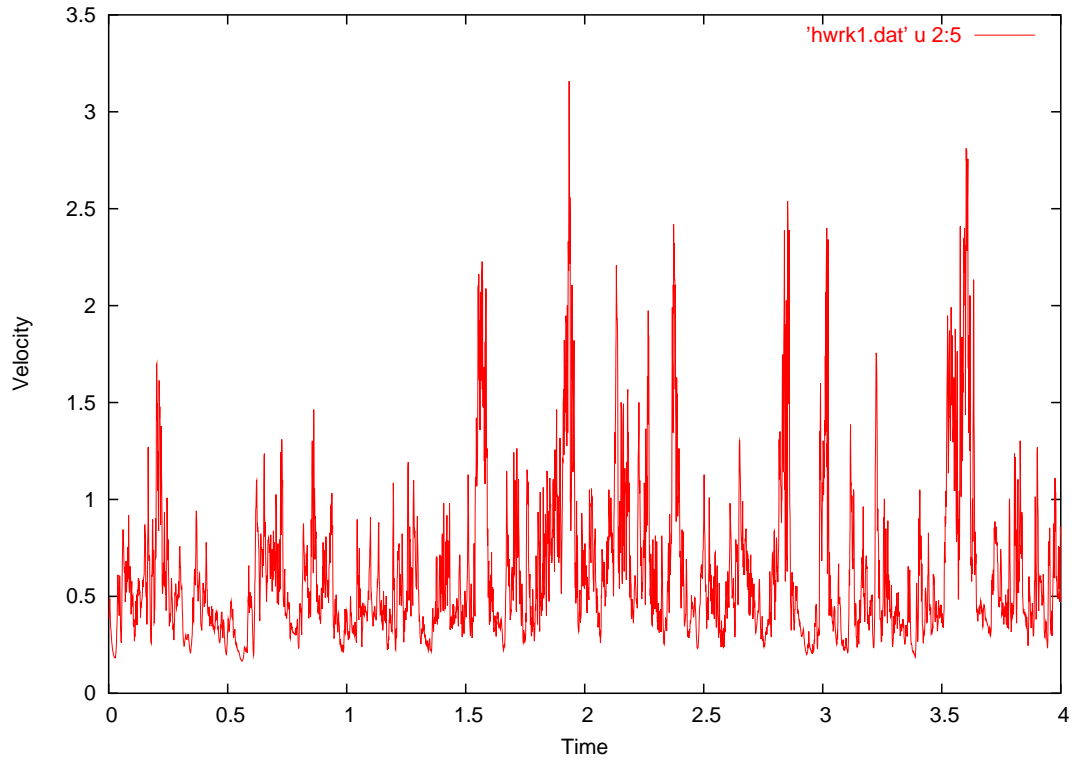


Figure 1: Velocity with respect to time at a point in turbulent flow.

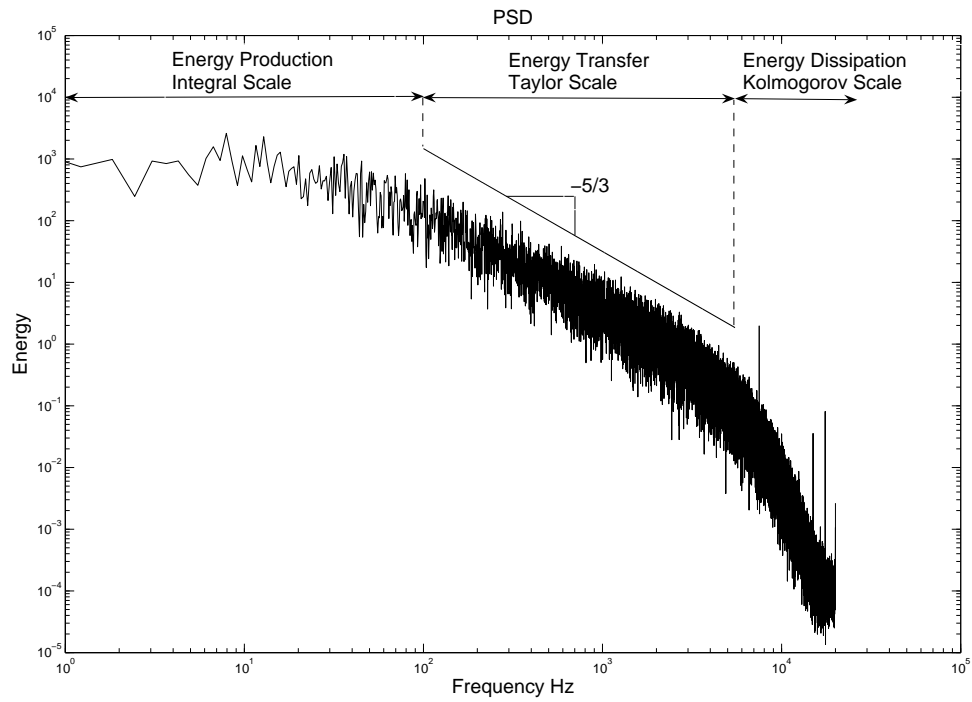


Figure 2: Turbulent energy spectrum.

scale. Each scale appears in its own range in Figure 2. The integral scale is where turbulence obtains its energy. The integral scale interacts with the mean shear and gains kinetic energy from it.

Following the integral scale is the Taylor scale, which resides in the middle range known as the inertial range. In this range energy is transferred from larger scale eddies to smaller scale eddies without significant losses from viscosity. Using known information about the small scale and the large scale and performing a dimensional analysis,(16) Andrei Kolmogorov derived the Kolmogorov power law,

$$E(\lambda, t) = C\bar{\epsilon}^{\frac{2}{3}}f^{-\frac{5}{3}} \quad (23)$$

where E is energy, $\bar{\epsilon}$ is dissipation and f is frequency. As seen in Figure 2, the inertial range has a constant slope with a value of $f^{-\frac{5}{3}}$ on an energy spectrum plot, verifying the Kolmogorov power law. The Kolmogorov power law has been verified so well that the inertial range is defined as the region on a power spectrum density plot with a slope of $-\frac{5}{3}$.

The third scale has been named after Kolmogorov. The Kolmogorov scale is the smallest scale. At this size, the eddies are too small to have enough inertia to overcome viscosity. Energy is then transferred from kinetic energy to heat via viscous dissipation. The Kolmogorov scale is dependent on two things, the energy it receives from the larger eddies and the viscosity of the fluid. Combining these two variables in such a way that results in units of length gives the Kolmogorov length scale, η , where

$$\eta = \left(\frac{\nu^3}{\bar{\epsilon}}\right)^{\frac{1}{4}} \propto Re_t^{-\frac{3}{4}} \quad (24)$$

and

$$Re_t = u'L/\nu \quad (25)$$

The Kolmogorov scale appears at the far right of the power spectrum density plot shown in Figure 2.

The Navier-Stokes equations contain everything needed to solve over all ranges and scales of a turbulent flow. The process of solving turbulence using nothing but the Navier-

Stokes equations is referred to as Direct Numerical Simulation (DNS). A DNS solution requires a mesh that is fine enough to capture the smallest length scales and a time step small enough to capture its frequency. Equation 24 shows that the Kolmogorov scale gets smaller as the Reynolds number grows. Even at moderate Reynolds numbers the Kolmogorov scale is so small that only the simplest of cases can be simulated. For this reason, turbulence modeling is used.

2.4 Turbulence Modeling

Turbulence is a chaotic and complex phenomenon. Fluctuations occurring in the flow do not follow a set pattern. For this reason, turbulence is best described mathematically with statistics. One approach is to model the flow in terms of the sum of a time averaged component and a fluctuating component, as shown in Equation 26. An overbar denotes a time averaged value while a fluctuation component is denoted with an apostrophe.

$$\begin{aligned} u &= \bar{u} + u' & \rho &= \bar{\rho} + \rho' \\ v &= \bar{v} + v' & p &= \bar{p} + p' \\ w &= \bar{w} + w' & T &= \bar{T} + T' \end{aligned} \tag{26}$$

Equation 27 shows rules for averaging. Inserting the values in Equation 26 into Equation 1 and averaging the resulting expression using the rules in Equation 27 results in the RANS equations. The RANS equations assume that turbulent time scales are much smaller than the characteristic time of the flow. Since this study will be using RANS models to simulate unsteady flow, care must be taken to ensure that the unsteady characteristic time is orders of magnitude larger than the averaging time. Otherwise, the unsteady effects will be averaged out.

$$\begin{aligned} \overline{f'} &= 0 & \overline{\bar{f}} &= \bar{f} & \overline{f'g} &= \bar{f}\bar{g} & \overline{f'g'} &= 0 \\ \overline{f+g} &= \bar{f} + \bar{g} & \frac{\partial \bar{f}}{\partial s} &= \frac{\partial \bar{f}}{\partial s} & \overline{fg} &= \bar{f}\bar{g} + \overline{f'g'} & \overline{\int f ds} &= \int \bar{f} ds \end{aligned} \tag{27}$$

The RANS equations can be simplified by applying Morkovin's hypothesis(2), which states that the fluctuating components of density are much smaller than the average density,

$\rho' \ll \bar{\rho}$. When Morkovin's hypothesis is applied to the RANS equations all the fluctuating terms except one drop out of the equations. This new term, shown in Equation 28, is called the Reynolds stress tensor. The Reynolds stress tensor captures the influence of the turbulent fluctuations on the mean flow. Being a symmetric tensor, the Reynolds stress tensor adds 6 new unknowns to the Navier-Stokes equations.

$$\overline{\rho u'_i u'_j} = \begin{pmatrix} \overline{\rho u' u'} & \overline{\rho u' v'} & \overline{\rho u' w'} \\ \overline{\rho u' v'} & \overline{\rho v' v'} & \overline{\rho v' w'} \\ \overline{\rho u' w'} & \overline{\rho v' w'} & \overline{\rho w' w'} \end{pmatrix} \quad (28)$$

A further simplification of the RANS equations is the Boussinesq assumption(1). Boussinesq assumed that the Reynolds stress is similar to the laminar viscous stresses and may be written as

$$-\overline{\rho u'_i u'_j} = 2\mu_t S_{ij} \quad (29)$$

where

$$S_{ij} = \frac{1}{2} \left(\frac{\partial U_i}{\partial x_j} + \frac{\partial U_j}{\partial x_i} \right) \quad (30)$$

is the strain rate tensor. Therefore, the Reynolds stress tensor is reduced to computing one new variable, the turbulent viscosity μ_t . Now, the same Navier-Stokes equations as used for laminar flow shown in Equation 1 may be used for the turbulent simulations with the RANS turbulence models, except the μ in Equation 4 is replaced with the sum of the laminar and turbulent viscosities, $\mu = \mu_l + \mu_t$. Finding a value for μ_t is the goal of the turbulence model. The two turbulence models under consideration in Beggar, the Spalart-Allmaras and Baldwin-Lomax models, both use the Boussinesq assumption.

2.5 *Baldwin-Lomax*

The Baldwin-Lomax model(1) is a “zero-equation” model which provides an algebraic closure for the Reynolds Averaged Navier-Stokes (RANS) equations based on the Boussinesq assumption. Baldwin-Lomax uses Prandtl's(43) mixing length theory, which by analogy with kinetic theory relates the turbulent viscosity to some turbulent length scale and a

velocity gradient:

$$\mu_t \simeq \rho l^2 \frac{\partial u}{\partial y} \quad (31)$$

where l is the “mixing-length”. Since turbulence is a continuum phenomena(43), the mixing-length is much larger than the mean free path of the fluid particle.

The Baldwin-Lomax model breaks the spectrum of turbulent eddies into two regions, the inner “near wall” region and an outer “wake” region. The viscosity in the inner region is calculated with a formula based on Prandtl’s mixing length theory known as the Prandtl-Van Driest(1) formula for the inner layer,

$$(\mu_t)_{inner} = \rho l^2 |\omega| \quad (32)$$

where ω is the magnitude of vorticity

$$|\omega| = \sqrt{\left(\frac{\partial u}{\partial y} - \frac{\partial v}{\partial x}\right)^2 + \left(\frac{\partial v}{\partial z} - \frac{\partial w}{\partial y}\right)^2 + \left(\frac{\partial w}{\partial x} - \frac{\partial u}{\partial z}\right)^2} \quad (33)$$

Prandtl and Karman(43) found that within the inner layer, the mixing-length was strongly dependent on the distance to the wall according to the following

$$l \propto \begin{cases} y^2 & \text{in the viscous sub-layer } (y^+ < 5) \\ ky & \text{in the overlap layer } (y^+ < 300) \end{cases} \quad (34)$$

where

$$y^+ = \frac{\sqrt{\rho_w T_w}}{\mu_w} y \quad (35)$$

Using this knowledge, a curve was generated that had the form of $l \propto y$ with a damping function added to fit the parabolic curve for $y^+ < 5$. This inner mixing-length is given by

$$l = ky \left(1 - e^{-y^+/A^+}\right) \quad (36)$$

where k is the Karman constant given as(9)

$$k = 0.41$$

and

$$A^+ = 26$$

which is optimized for zero pressure gradient simulations.

The turbulent viscosity in the outer region is given by

$$(\mu_t)_{outer} = KC_{cp}\rho F_{wake}F_{Kleb}(y) \quad (37)$$

where the Clauser constant is

$$K = 0.0168$$

and

$$C_{cp} = 1.6$$

$$F_{wake} = \min(y_{max}F_{max}, C_{wk}y_{max}u_{dif}^2/F_{max}) \quad (38)$$

$$C_{wk} = 1.0$$

Baldwin and Lomax used a value of $C_{wk} = 0.25$, but Swanson and Turkel (38) found that this value performs poorly in transonic flows over an airfoil. Swanson and Turkel recommend using $C_{wk} = 1.0$. F_{max} and y_{max} are determined from

$$F(y) = y|\omega| \left(1 - e^{-y^+/A^+}\right) \quad (39)$$

with F_{max} being the largest value in a particular profile (constant stream-wise location) and y_{max} being the cross-flow location of that maximum. In wakes the exponential term in Equation 39 is set equal to zero(1). The Klebanoff intermittence factor is

$$F_{Kleb}(y) = \left[1 + 5.5 \left(\frac{C_{Kleb}y}{y_{max}}\right)^6\right]^{-1} \quad (40)$$

This provides a correction for the intermittence in the boundary between the turbulent and laminar flow regions. Baldwin and Lomax optimized C_{Kleb} and agreed that $C_{Kleb} = 0.3$ was the best value for separated flow(1). It is common practice to use $C_{cp} = 1.6$. The

minimum velocity magnitude:

$$u_{dif} = |\mathbf{V}|_{max} - |\mathbf{V}|_{min} \quad (41)$$

is zero except in wakes.

Baldwin-Lomax is a simple to implement model that provides good results in attached turbulent flow(45). However, there is no turbulent transport, meaning that the upwind turbulence is not felt downwind. A turbulence model which includes turbulent transport is the Spalart-Allmaras one-equation model.

2.6 *Spalart-Allmaras*

The Spalart-Allmaras turbulence model is a one-equation model, meaning that it adds one partial differential equation that must be solved along with the Navier-Stokes equations. Along with the new equation comes another variable that must be computed. The new variable in the Spalart-Allmaras model is $\tilde{\nu}$, a working variable with units equivalent to that of viscosity. The new equation introduced by Spalart and Allmaras, like most transport models, is similar to the species equation for reacting flow(34). The Spalart-Allmaras model was derived from empiricism, dimensional analysis, and Galilean invariance. It was developed with wall bounded flows in mind(7). The specific equation solved in the Spalart-Allmaras model is:

$$\frac{\partial \tilde{\nu}}{\partial t} + U_i \frac{\partial \tilde{\nu}}{\partial x_i} = \frac{1}{\sigma} [\nabla \cdot ((\nu + \tilde{\nu} \nabla \tilde{\nu}) + C_{b2}(\nabla \tilde{\nu})^2] + P(\tilde{\nu}) - D(\tilde{\nu}) \quad (42)$$

After solving Equation 42, the turbulent viscosity μ_t may then be found from

$$\mu_t = \rho \tilde{\nu} f_{v1}(\chi) \quad (43)$$

where

$$\chi \equiv \frac{\tilde{\nu}}{\nu} \quad and \quad \mu = \rho \nu$$

The viscous damping function, f_{v1} , is given by:

$$f_{v1} = \frac{\chi^3}{\chi^3 + C_{v1}^3}, \quad (44)$$

$P(\tilde{\nu})$ in Equation 42 is the production term, given by:

$$P(\tilde{\nu}) = C_{b1} \left(S + \frac{\tilde{\nu}}{\kappa^2 d^2} f_{v2} \right) \quad (45)$$

where S is the magnitude of vorticity and

$$f_{v2} = 1 - \frac{\chi}{1 + \chi f_{v1}}. \quad (46)$$

The destruction term in Equation 42, $D(\tilde{\nu})$, is given as

$$D(\tilde{\nu}) = C_{w1} f_w \left(\frac{\tilde{\nu}}{d} \right)^2 \quad (47)$$

where

$$f_w = g \left[\frac{1 + C_{w3}^6}{g^6 + C_{w3}^6} \right]^{1/6} \quad (48)$$

and

$$g = r + C_{w2}(r^6 - r) \quad (49)$$

and

$$r \equiv \frac{\tilde{\nu}}{(S\kappa^2 d^2 + \tilde{\nu} f_{v2})} \quad (50)$$

In both Equation 45 and Equation 47, d is the distance to the closest wall. The remaining unknowns in the Spalart-Allmaras model are constants which were determined numerically or via matching empirical data, as shown below.

$$C_{b1} = 0.1355 \quad C_{b2} = 0.622 \quad \sigma = \frac{2}{3} \quad C_{v1} = 7.1$$

$$C_{w1} = \frac{C_{b1}}{\kappa^2} + \frac{(1 + C_{b2})}{\sigma} \quad C_{w2} = 0.3 \quad C_{w3} = 2.0 \quad \kappa = 0.41$$

2.7 Detached Eddy Simulation

The third and final turbulence model considered in this document is the Detached Eddy Simulation (DES) model. DES is a hybrid of the Spalart-Allmaras model combined with similar spatial filtering styles of Large Eddy Simulation (LES). All temporally averaged RANS turbulence models, include Baldwin-Lomax and Spalart-Allmaras, place the responsibility of capturing turbulence completely on the model. All scales of turbulence, from the smallest to the largest, must be accounted for by these models. LES models, on the other hand, break the turbulent eddies into two scales, a grid realized region and a subgrid region. The larger scales of turbulence, which are able to exist away from solid boundaries, are usually larger than the grid spacing. As mentioned before, the Navier-Stokes equations include everything necessary to simulate turbulence, as long as the grid spacing is fine enough to capture the eddies and the time step is small enough to capture the turbulent frequencies. The large turbulent eddies away from a wall are often large enough that they will be captured by a reasonably fine grid. Therefore, applying a RANS turbulence model will compute the energy of the grid resolved eddies twice, once from the Navier-Stokes equations and again with the turbulence model. To correct for this, the DES model combines the Spalart-Allmaras RANS model with a spatial filtering function. As seen in Equation 47, the turbulent destruction term of the Spalart-Allmaras model is inversely proportional to the square of the distance to the nearest wall, d . Away from a wall, this term will approach zero while the production term will approach a constant non-zero value. To account for turbulent destruction away from a wall, the DES model replaces d in the Spalart-Allmaras model equations with \tilde{d} where

$$\tilde{d} = \min(d, C_{\text{DES}}\Delta) \quad (51)$$

where d is still the distance to the nearest wall, Δ is the largest grid spacing of the cell, and C_{DES} is an empirically determined constant set to $C_{\text{DES}} = 0.65$.

2.7.1 Beggar Implementation. The turbulence models in Beggar are solved along with the flow equations. Therefore, the turbulent variable is updated every Newton iteration. Then the flow equations are solved. Baldwin-Lomax is an algebraic model, so it explicitly calculates and updates the turbulent variable each time step. Because Spalart-Allmaras solves a differential equation, it is broken up into Jacobian and right hand side

term like the flow equations and solved in the same manner as the flow equations. The DES model is solved in the same manner as Spalart-Allmaras.

III. NON-TURBULENT STUDY

There are certain prerequisites that any CFD simulation must meet before any turbulence model can perform well. The code cannot have overwhelming artificial dissipation, or the effects of turbulent viscosity will be masked. Time steps and grid cells must not be too large, or the steep gradient will not be captured. Finally, each time step must be sufficiently converged, or time accuracy will be lost. Some of these prerequisites are not necessary when modeling steady flow, but are critical for unsteady turbulent flow. The cases in this chapter are designed to ensure that these prerequisites are met.

Three non-turbulent cases will be examined; a vortex convecting in an inviscid atmosphere, a viscous shock-tube, and a $2D$ cylinder in crossflow. As described in Section 2.2, the Roe and Steger-Warming methods are included in Beggar to solve the right hand side term, which is a primary factor of artificial dissipation. Each of the three cases will examine the differences between the Roe and Steger-Warming discretization schemes to approach a recommendation on which should be used in unsteady turbulent cases. The best method will be used in the three turbulent cases in Chapter IV, because the time needed to run these cases for both schemes would exceed the time available to finish this study.

As described in Section 2.2, Beggar uses a Newton iteration scheme to converge each time step. The shock-tube and $2D$ cylinder cases were used to evaluate various numbers of Newton dt-iterations. Determining the number of dt-iterations is an important aspect of the non-turbulent cases. Unlike steady-state calculations, when converging each time step is not an important consideration, each time step must be converged to properly simulate unsteady flow. For unsteady Beggar computation, the user specifies both the number of Newton dt-iterations and the maximum number of Gauss-Seidel inner iterations. Convergence criteria may also be set on the Gauss-Seidel inner iterations. Unless there is a good deal of variation, for example initially imposing the wall boundary conditions, the maximum number of Gauss-Seidel inner iterations is rarely used. However, the specified number of Newton dt-iterations is always used. Each Newton iteration is computationally expensive. The amount of accuracy gained from each additional Newton dt-iteration drops logarithmically.

All three of the non-turbulent cases are two-dimensional. However, Beggar is a three-dimensional code. Therefore, all three grids actually have dimensions of $nxm \times 3$. To force

a 2D computation, tangent boundary conditions were applied to both outside layers, which means that the flow equations were only solved at the middle layer of nodes.

3.1 *Inviscid Convecting Vortex*

3.1.1 Case Presentation. The first case examined in the process of validating the turbulence model is a vortex convecting in an inviscid atmosphere. The inviscid atmosphere is modeled using the Euler equations which do not include any viscous terms. Therefore, any dissipation can be attributed to numerical fluxes, and is artificial. For steady state solutions, this artificial dissipation may be desirable. The increased dissipation may damp out undesirable unsteady effects. However, time-accurate solutions are dependent on these unsteady effects, and too much artificial dissipation could corrupt the simulation. The inviscid convecting vortex is a quick simulation to run to check the numerical dissipation in each component of the code.

A traversing inviscid vortex case was simulated several times while using different solver option combinations each time. The following solver option combinations were used:

1. 2nd order Roe right hand side with 1st order backwards Euler time step
2. 2nd order Steger-Warming right hand side with 1st order backwards Euler time step
3. 2nd order Roe right hand side with 2nd order three point backwards time step
4. 2nd order Steger-Warming right hand side with 2nd order three point backwards time step

The first order backwards Euler time scheme is less accurate than the second order three point backwards and is expected to have more numerical dissipation. Similarly, the Roe method is more accurate than Steger-Warming and should provide less numerical dissipation.

Assuming a unit vortex core radius, the non-dimensional equations for generating the initial velocities and pressure are(24):

$$u = u_{\infty} - \frac{\Gamma}{2\pi} \exp\left(\frac{1}{2}(1 - R^2)\right) \Delta y \quad (52)$$

$$v = \frac{\Gamma}{2\pi} \exp\left(\frac{1}{2}(1 - R^2)\right) \Delta x \quad (53)$$

and

$$p = \left(\frac{T^{\gamma_{\infty}}}{S_{\infty}}\right)^{\frac{1}{\gamma-1}} \quad (54)$$

where

$$T = T_{\infty} - \frac{\gamma - 1}{2\gamma_{\infty}} \left(\frac{\Gamma}{2\pi}\right)^2 \left[\exp\left(\frac{1}{2}(1 - R^2)\right)\right]^2, \quad (55)$$

$$S_{\infty} = \frac{p_{\infty}}{\rho_{\infty}^{\gamma_{\infty}}}, \quad T_{\infty} = \frac{p_{\infty}}{\rho_{\infty}}, \quad p_{\infty} = \frac{\rho_{\infty} c_{\infty}^2}{\gamma_{\infty}},$$

and R is the distance from the center of the vortex, c_{∞} is the speed of sound and Δx and Δy are the x and y positions with respect to the center of the vortex, respectively. The strength of the vortex is given by Γ . The initial conditions used are given in Table 2.

Table 2: Inviscid convecting vortex initial conditions - non-dimensional values

Property	Value
M_{∞}	0.5
Re	2.0×10^5
Γ	5.0
c_{∞}	1.0
ρ_{∞}	1.0
γ_{∞}	1.4
Solver Options: 2nd Order Spatial Discretization Steger-Warming Jacobians	

The effect of a vortex is negligible at a distance of 5 times the core radius from the center of the vortex. Therefore, with a vortex core radius of 1.0, the effects of the vortex will be negligible at a distance of 5.0 from the center. From this knowledge, grids with equal length sides of 10 vortex core radii were created. All cases were run on both a coarse grid and a fine grid. The coarse grid has dimensions of 81x81 while the fine grid has dimensions of 161x161. The general spacing of the coarse grid with respect to the vortex can be seen in Figure 3. However, since Beggar is a cell centered code, all of its output is also cell centered. Therefore, the gridlines seen in Figure 3 intersect at cell centers rather than gridpoints. This gives the illusion that the initial center of the vortex lies in a cell center, when actually the initial center of the vortex lies at the gridpoint with coordinates (5.0,5.0). In hindsight, the

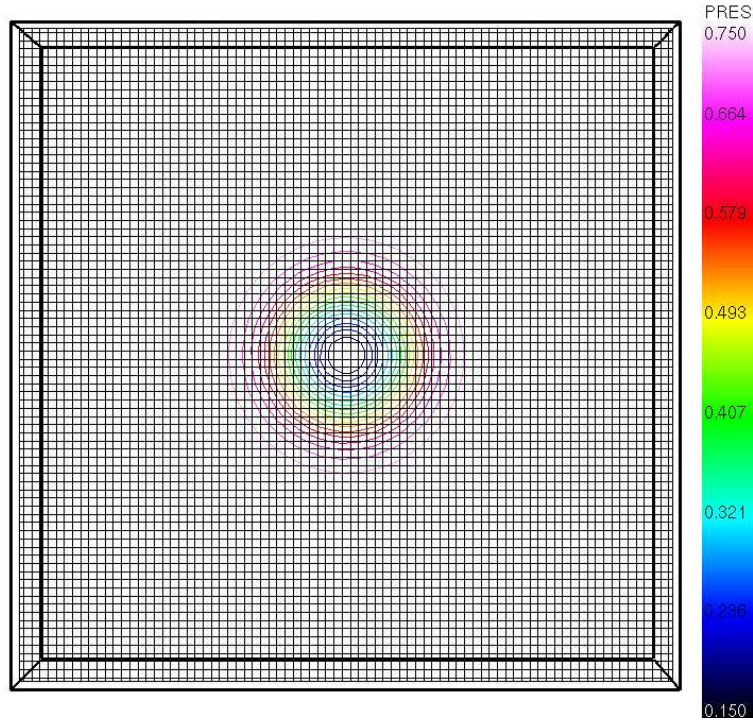


Figure 3: Initial vortex in the coarse 81x81 grid

vortex center should have been placed at a cell center. That way Beggar would have had the capability of exactly predicting the y-location of the center of the vortex. With the center of the vortex being placed at a node and Beggar being a cell-centered code, the best Beggar can do is to predict the center of the vortex $\frac{1}{2}$ cell from its true location.

As mentioned previously, the vortex was initially centered at the middle of the grid. The vortex then convected in the x direction at the set Mach number. Periodic boundary conditions were applied on all boundaries. Therefore, when the vortex passes through one boundary and instantaneously appears on the opposite boundary. A cycle is complete when the vortex returns to its original position. Two time steps were investigated. The larger and smaller time steps have non-dimensional values of 0.04 and 0.02, respectively. With these time step sizes, 500 and 1000 time steps respectively are necessary for the vortex to traverse the length of the grid and return to its original position. Each time step was converged using three Newton dt-iterations. Each Newton dt-iteration was converged using at most

60 symmetric Gauss-Seidel inner iterations. If the inner iterations reached the convergence criteria, then not all 60 iterations were calculated.

Pressure was used to indirectly measure the errors in the solution. As can be seen in Equations 54 and 55, the pressure is minimum at the center of the vortex. After each time step, the minimum pressure was located. The magnitude and location were both stored. Therefore, there are two items to measure error:

1. Change in minimum pressure from initial value
2. Deviation of the minimum pressure from theoretical location of vortex center

3.1.2 Results. The results for the inviscid vortex case are shown in Figures 4 to 18. Figures 4 to 8 show data at an exact point in time. Figures 9 to 18 show continuous data from zero to six cycles.

In Figures 4 to 8, only the contours and the grid outline appear; the grid has been removed to give a better view of the contours. Figure 4 shows the initial pressure contours and the direction of vortex convection. Figures 5 to 8 show pressure contours after six cycles for each of the solver combinations. An exact solution would result in an unchanged vortex after each cycle. Artificial dissipation can be qualitatively seen by the expansion of the inner ring of the pressure contour plots. Other numerical errors can be seen in the distortion of the shape of the vortex.

Figure 5 shows the 1st order temporal - Steger-Warming RHS combination. It has a good deal of dissipation as the innermost pressure contour ring has expanded a relatively large amount. The shape of the vortex has also been moderately distorted. The vortex shape resembles more of an ellipse than a circle.

Figure 6 shows the 2nd order temporal - Steger-Warming RHS combination. It has an innermost pressure contour almost identical to the initial vortex. The circular shape is maintained throughout most of the core of the vortex. However, the outermost rings of the vortex are highly distorted.

Figure 7 shows the 1st order temporal - Roe RHS combination. Similar to Figure 5, it has noticeable artificial dissipation as seen in the expansion of the innermost pressure

contour. Unlike Figure 5, however, Roe did not distort the general shape of the vortex. It still much resembles a circle until the outermost contour.

Figure 8 shows the 2^{nd} order temporal - Roe RHS combination. This combination has compacted the whole vortex, reducing the core radius and strength of the vortex. The circular shape of most of the inner contours was maintained. The outermost contours are distorted, no longer resembling a circle in the least. Furthermore, the position of the vortex is noticeably different. The vortex appears to be centered along the abscissa, but has traversed about one vortex core radius along the ordinate.

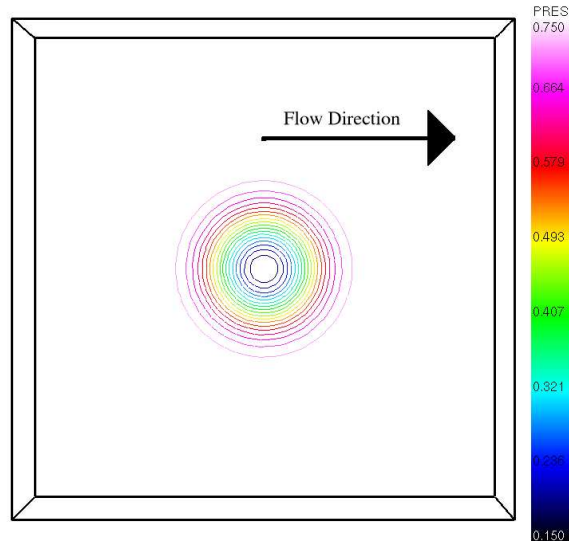


Figure 4: Vortex - Initial Pressure Contours

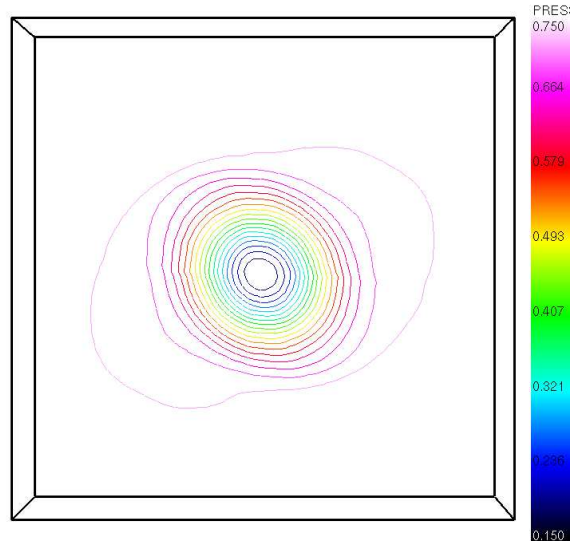


Figure 5: Vortex - Steger-Warming - 1st Order Temporal - Pressure Contours After 6 Cycles

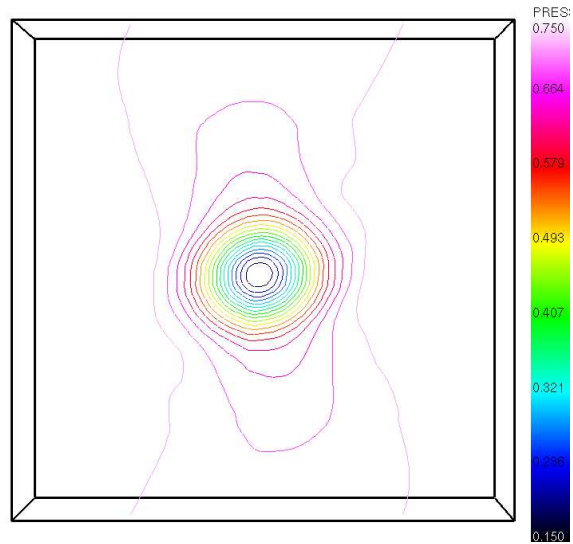


Figure 6: Vortex - Steger-Warming - 2nd Order Temporal - Pressure Contours After 6 Cycles

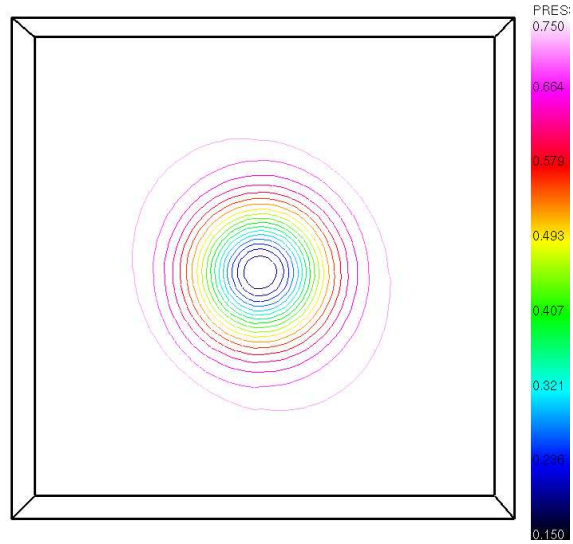


Figure 7: Vortex - Roe - 1st Order Temporal - Pressure Contours After 6 Cycles

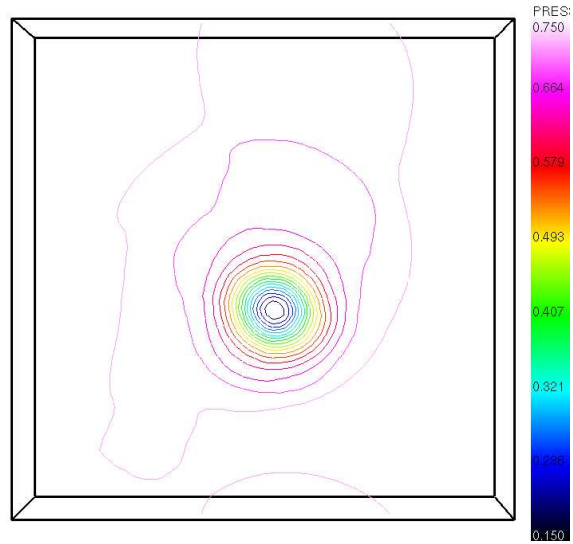


Figure 8: Vortex - Roe - 2nd Order Temporal - Pressure Contours After 6 Cycles

Figures 9 to 18 show continuous data from the initial vortex to when the vortex has traversed six cycles. At each time step, the minimum pressure and its x and y coordinates were found. Figures 9 and 10 show the minimum pressure as the vortex traverses. Recalling that the minimum pressure should be located at the center of the vortex, the x and y coordinates of the minimum pressure at each time step were used as the vortex center to find the Δx and Δy of the vortex from its theoretical location. Figures 11 to 18 show various deviations as the vortex traverses. Because the true center of the vortex passes through grid-points lying on the $y = 5.0$ axis and Beggar is a cell-centered instead of node-centered scheme, the best Δy obtainable is either $\Delta y = +0.5$ cells or $\Delta y = -0.5$ cells. The computed x values as well lie at discrete points whereas the theoretical vortex center will lie between grid-points. Therefore, the best Δx obtainable will range from $-0.5 < \Delta x < 0.5$ cells, depending on the theoretical position of the vortex.

Figure 9 compares Roe and Steger-Warming, 1st and 2nd order combinations on the coarse grid. The initial slope of the curves are greater for both 1st order cases, indicating more numerical dissipation. This difference in slope shows the necessity of a second order time discretization. Within the first two cycles, the error of the 1st order time discretization on the coarse mesh was about two times greater than the 2nd order time discretization with the Steger-Warming method and about four times greater with the Roe method. Comparing the different RHS methods, Roe has a smaller initial slope than Steger-Warming for both the 1st and 2nd order temporal discretization schemes. Similar results were obtained with the fine grid, shown in Figure 10, except at about five cycles Roe with the 2nd order temporal scheme has a drastic jump in minimum pressure and apparently becomes unstable. Similar results were observed with the halved time step. All plots can be seen in Appendix A.1.

Figures 11 and 12 shows that the vortex center moved -0.75 cells in the x direction while staying as on track as numerically possible in the y direction for the 1st order temporal - Roe RHS combination.

Figures 13 and 14 shows the 2nd order temporal - Roe RHS combination. The vortex starts to traverse a little slower than theory until the fifth cycle. Then the vortex suddenly speeds up and the Δx goes from one cell behind to 3 cells ahead of the theoretical location. Similarly, the y position is as true as possible until the sixth cycle. Then the vortex starts

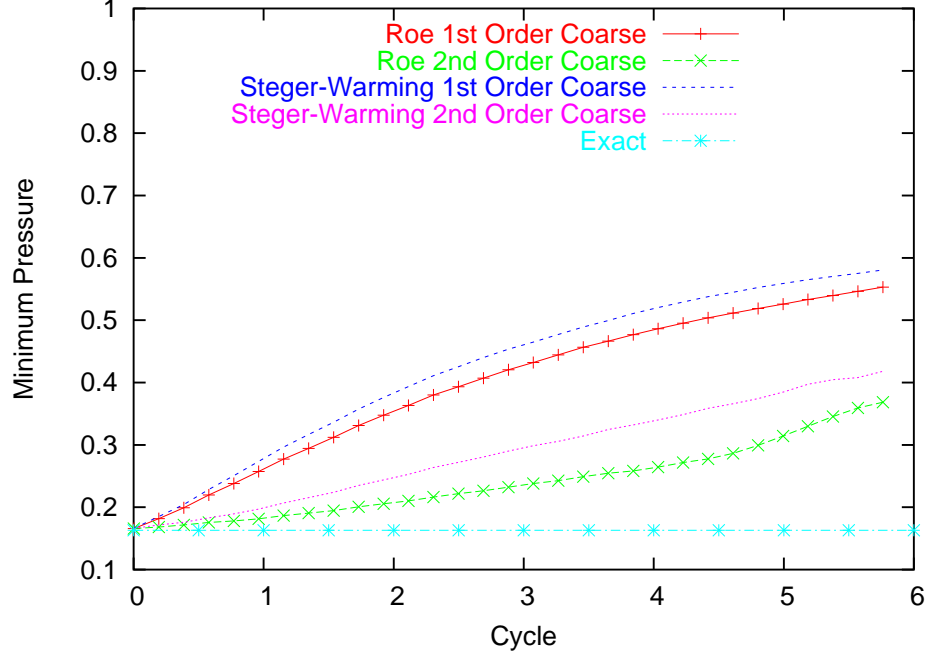


Figure 9: Cycle vs Minimum Pressure - Coarse Grid

traversing in the negative y direction. The calculated vortex center moved more than six cells in the y direction between the fifth and sixth cycle. This shows that the 2nd order temporal - Roe RHS combination has inherent instabilities. Roe treats $2D$ problems as two $1D$ problems, resulting in maximum error 45° from these axes(41). This combined with the second order temporal discretization could be causing the instability.

Figures 15 and 16 shows that the vortex center moved an average of -0.5 cells in the x direction for the 1st order temporal - Steger-Warming RHS combination. The calculated y position was predicted perfectly until the sixth cycle, when it moved one cell down from the theoretical position.

Figures 17 and 18 shows that the vortex center deviated about one cell in the x direction in five cycles before starting to return to its true position for the 2nd order temporal - Steger-Warming RHS combination. The calculated y position was predicted perfectly except near the completion of the fifth cycle when it moved one cell down from the theoretical position.

The fine grid and the halved time-step simulations gave similar results, which can be seen in Appendix A.1.

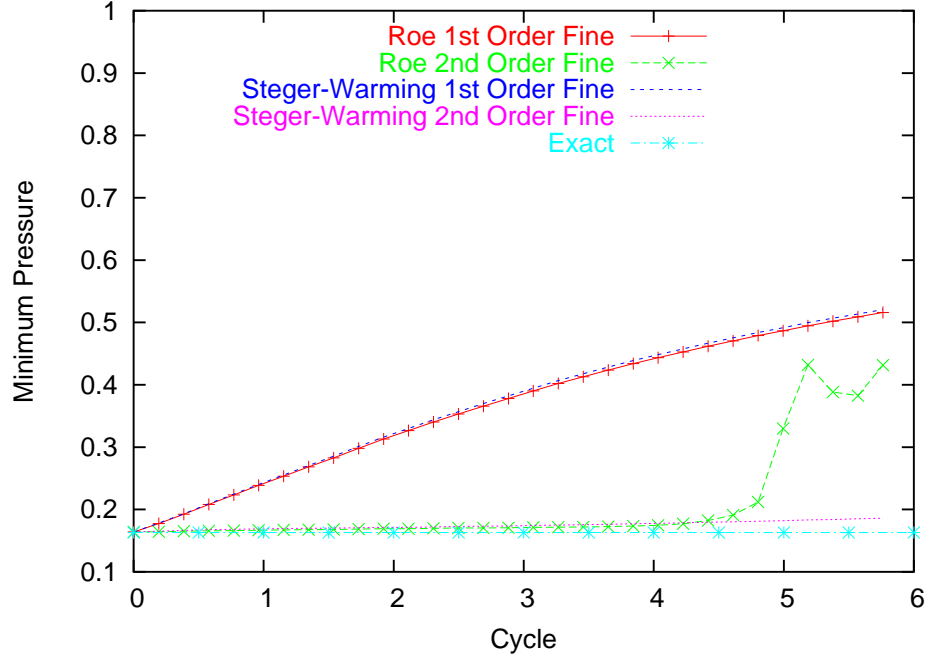


Figure 10: Cycle vs Minimum Pressure - Fine Grid

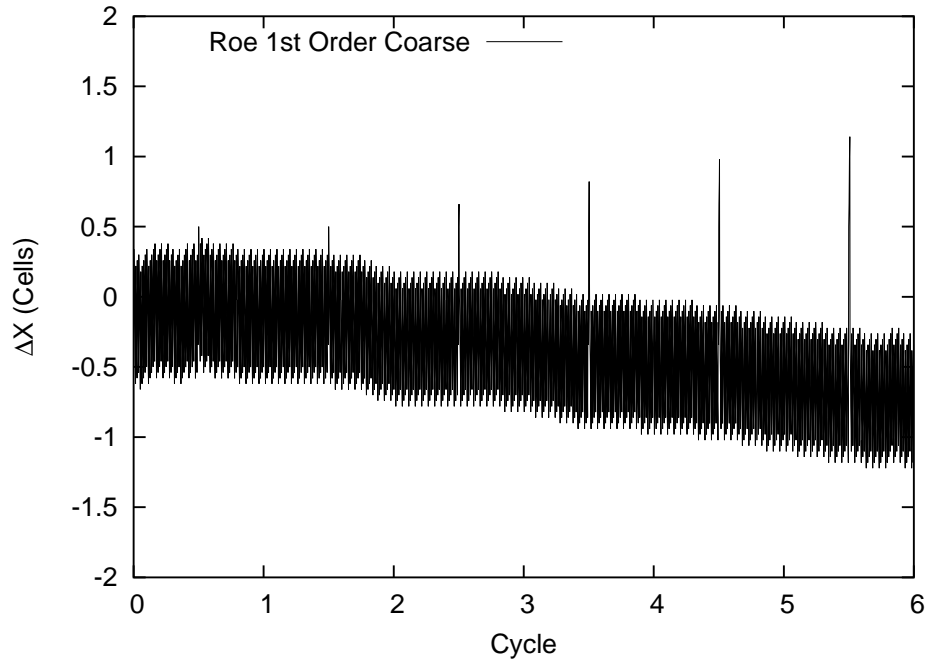


Figure 11: Cycle vs Δx - Roe - Coarse Grid - 1st Order Temporal

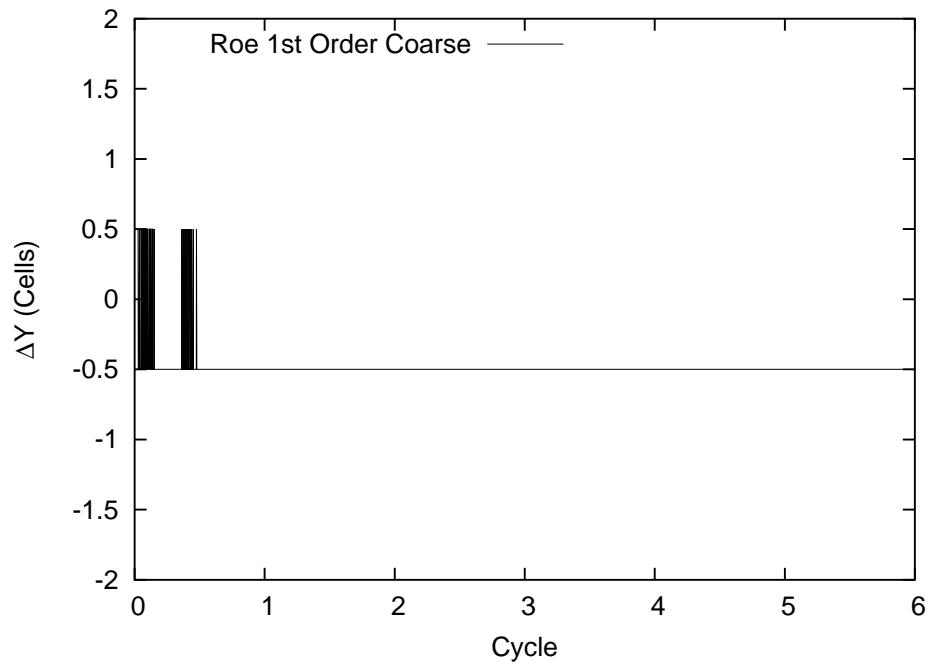


Figure 12: Cycle vs Δy - Roe - Coarse Grid - 1st Order Temporal

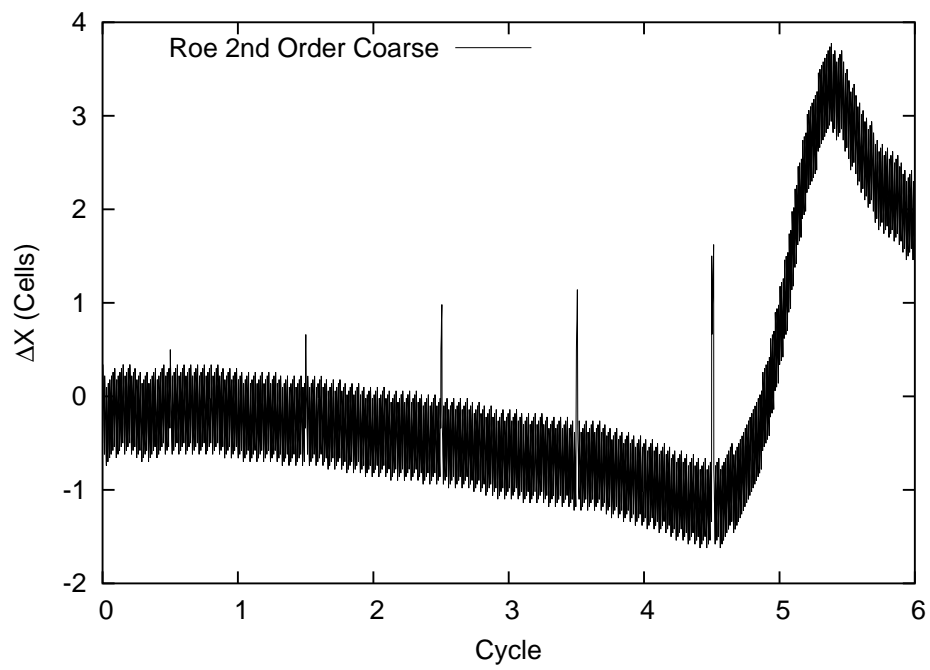


Figure 13: Cycle vs Δx - Roe - Coarse Grid - 2nd Order Temporal

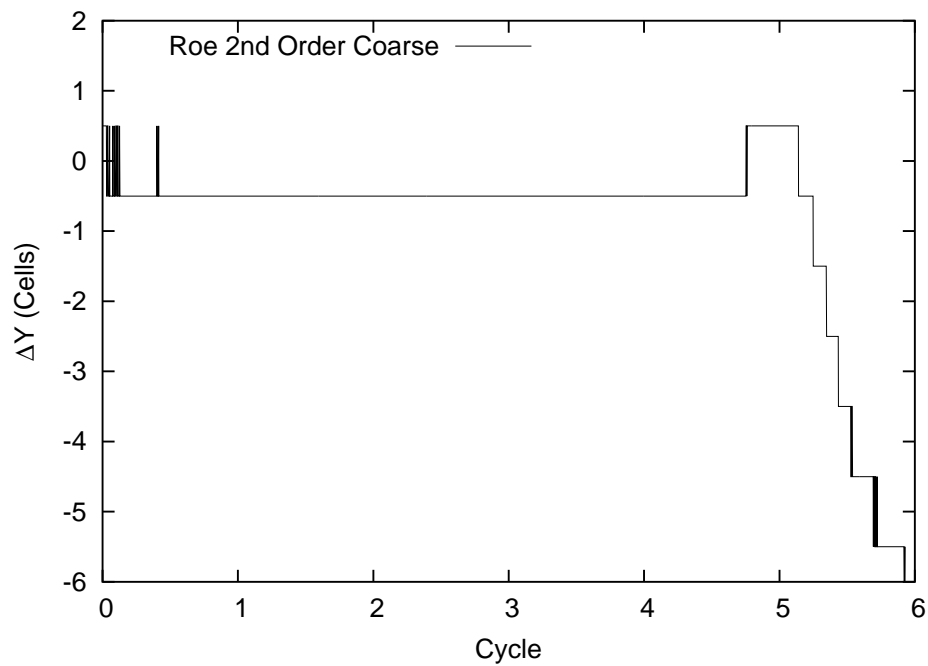


Figure 14: Cycle vs Δy - Roe - Coarse Grid - 2nd Order Temporal

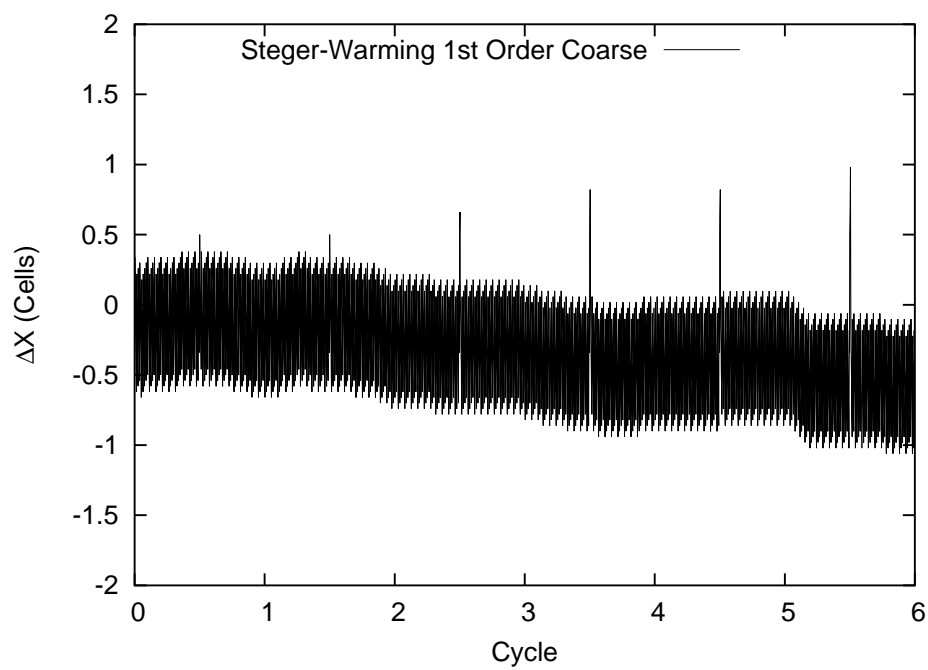


Figure 15: Cycle vs Δx - Steger-Warming - Coarse - 1st Order Temporal

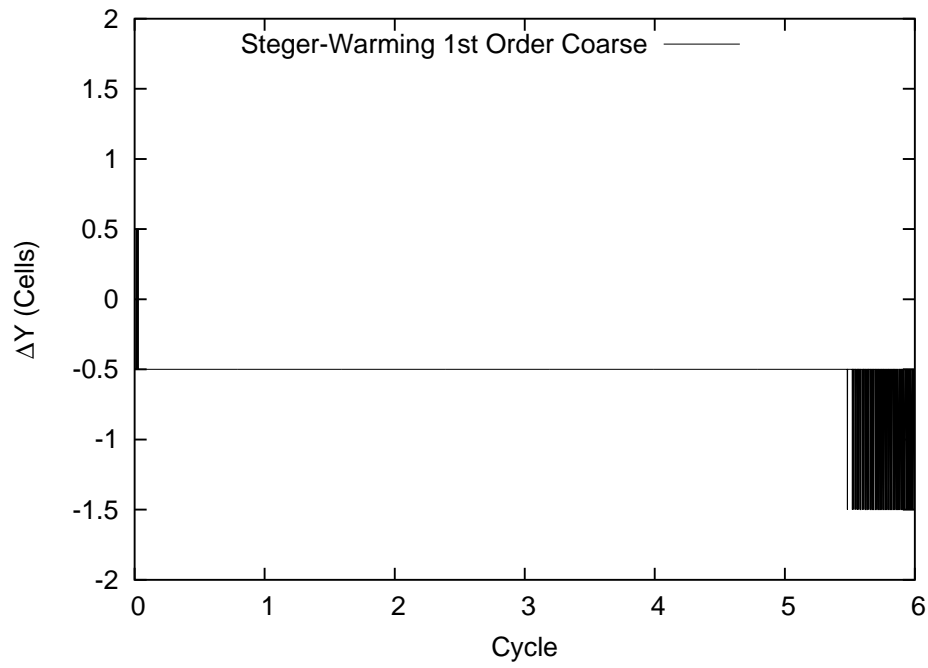


Figure 16: Cycle vs Δy - Steger-Warming - Coarse Grid - 1st Order Temporal

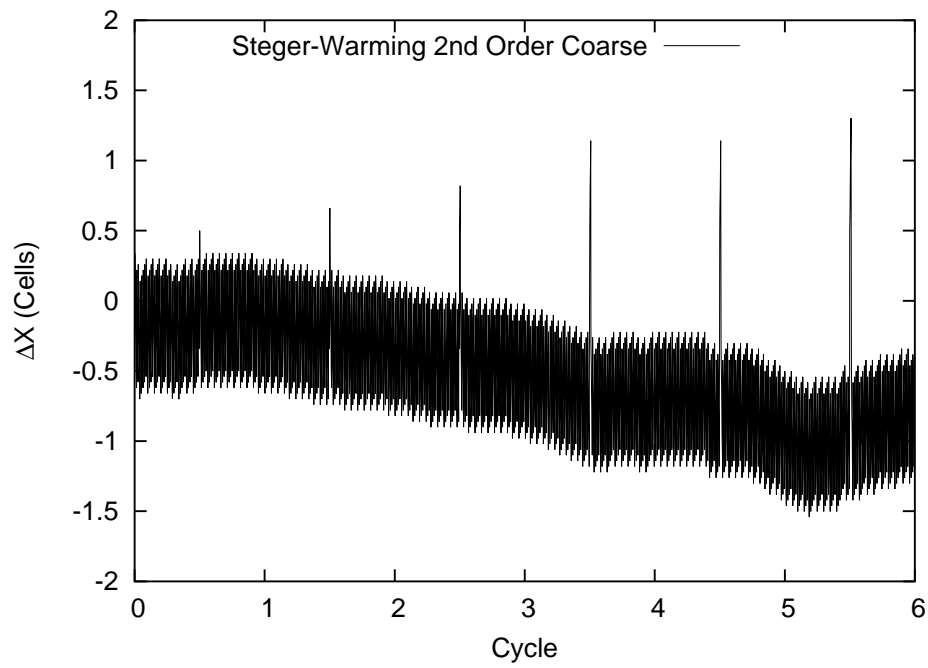


Figure 17: Cycle vs Δx - Steger-Warming - Coarse Grid - 2nd Order Temporal

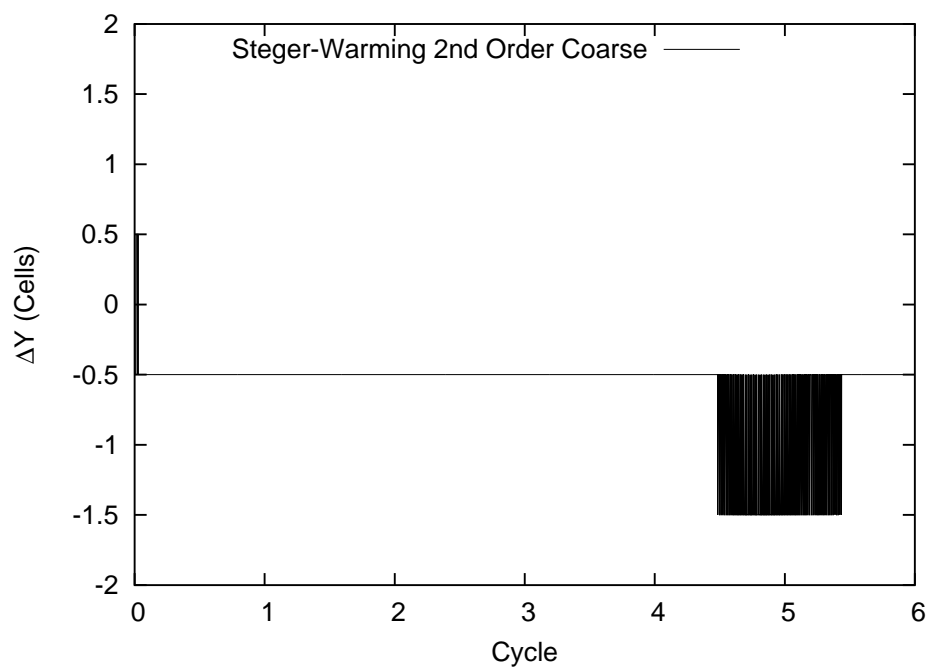


Figure 18: Cycle vs Δy - Steger-Warming - Coarse Grid - 2nd Order Temporal

3.2 Shock-Tube

3.2.1 Case Presentation. The second case in the non-turbulent study is the shock-tube or 'Riemann' problem(39). The theoretical data for the shock-tube is an exact solution of the Euler equations that can be obtained from any compressible flow textbook. This case is interesting because it contains a moving shock, a growing expansion fan, and a contact discontinuity. To slightly increase the difficulty of the problem, viscous laminar Navier-Stokes equations were solved in the simulation. This was accomplished by having a two dimensional grid with a wall boundary condition on the top and bottom. Figure 19 shows the viscous shock-tube grid, which has dimensions of 101x81. The viscous spacing off the axial wall can also be seen in Figure 19, which has an initial wall spacing of 0.09% of the total height of the grid. The center of the shock tube along the axial direction is far enough from the walls that viscous effects will be minimal and will be nearly inviscid. Data is gathered from this location as it will best match the inviscid theoretical data.

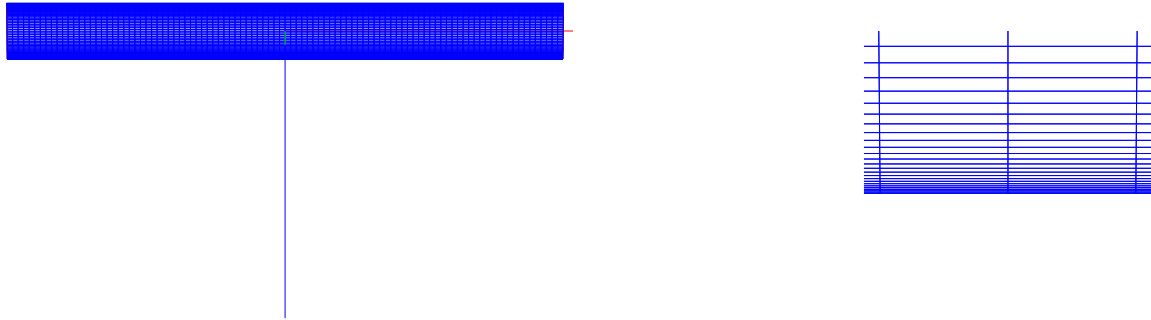


Figure 19: 2D Viscous Shock-Tube Grid

The shock-tube is simulated by dividing the long rectangular grid shown in Figure 19 into left and right regions. The left and right regions are then initialized using different values for density, pressure, and/or temperature. Both regions are initialized to have zero initial velocity. This imitates a shock-tube directly after the diaphragm has been broken. The non-dimensional values used in this case are shown in Table 3.

Table 3: Shock-tube example initial conditions - non-dimensional values

Property	Left Region	Right Region
ρ	1.0	0.1
p	1.0	0.1
Mach	0.0	0.0
Solver Options: 2nd Order Spatial Discretization Steger-Warming Jacobians		

The shock-tube case was used to perform the three following items:

1. Investigate differences between the Roe and Steger-Warming discretization schemes
2. Determine the optimal number of Newton dt-iterations to use in future calculations

To test that the solution is independent of the time step, two time steps will be used. The larger and smaller non-dimensional time steps are 0.00125 and 0.000625, respectively. All data was recorded at a non-dimensional time of 0.2 which corresponds to 160 and 320 time steps, respectively.

The most important aspect to this case is the Newton dt-iteration test. This case was run with one, three, five, ten, twenty, and fifty Newton dt-iterations. The fifty Newton dt-iterations runs were used as reference solutions to compute errors.

3.2.2 Results. The results for the shock-tube case are shown in Figures 20 to 24.

Figure 20 shows a density plot at non-dimensional time 0.2 along the centerline of the shock tube. Both the 1st and the 2nd order time discretization methods accurately predict the location of the expansion fan, contact discontinuity and the shock. Roe does a better job than Steger-Warming at capturing the shock and contact discontinuities, and more sharply predicts the beginning and end of the expansion fan. Figure 21 shows a zoomed in view of the trailing edge of the expansion fan.

Figure 22 shows that halving the time step and doubling the number of time iterations will result in the same solution, proving that the converged time step size has been used. Figure 23 compares a 1 Newton dt-iteration per time step simulation to a 50 Newton dt-iterations per time step simulation. For this simple problem, 1 Newton dt-iteration results in as good of a solution as 50 Newton dt-iterations.

Figure 24 shows the results of the Newton dt-iteration study. For this study, the 50 Newton dt-iterations per time step simulation was used as a reference to calculate the percent errors of the other simulations using an L_∞ norm calculation. Instead of being an error with respect to theory or experimental data, this error is Newton convergence error. Furthermore, as can be seen in Figure 23, both the 1 and 50 Newton dt-iterations per time step simulations gave almost the same answer. Therefore, the error plots presented here are used only to determine Newton dt-iteration convergence, not to determine if a certain number of Newton dt-iterations is within an error bounds. All of the curves in Figure 24 show the same trends; they all plateau at 5 Newton dt-iterations. Error data gathered from pressure was plotted and gave similar results. It is concluded that more than 5 dt-iterations is superfluous. The error curve breaks between 3 and 5 Newton dt-iterations. Before 3 Newton dt-iterations the the curve is steep enough that using less than 3 Newton dt-iterations per time step may result in poorly converged time steps. The conclusion is reached that between 3 and 5 Newton dt-iterations should be calculated per time iteration.

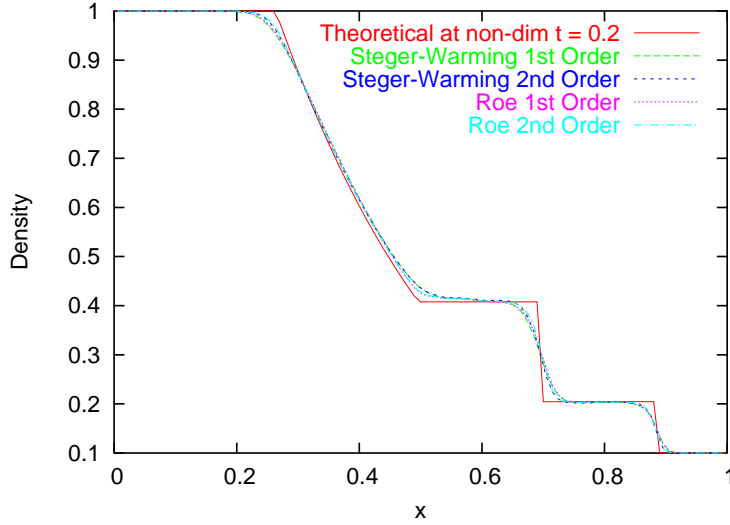


Figure 20: Shock-Tube Density at Non-Dimensional Time $t = 0.2$

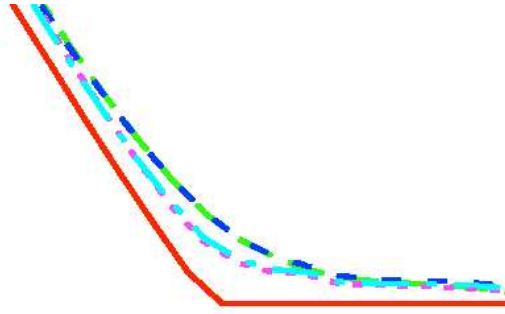


Figure 21: Zoomed in Image of Figure 20 at Trailing Edge of Expansion Fan

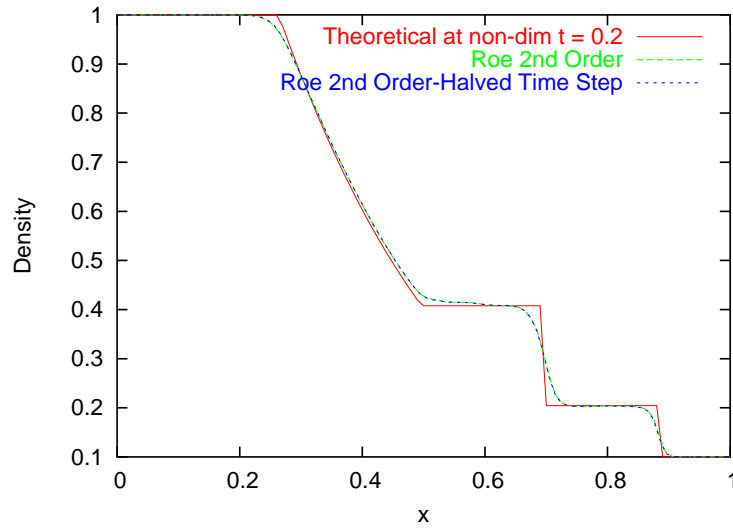


Figure 22: Shock-Tube Density at Non-Dimensional Time $t = 0.2$ - Halved Time Step comparison

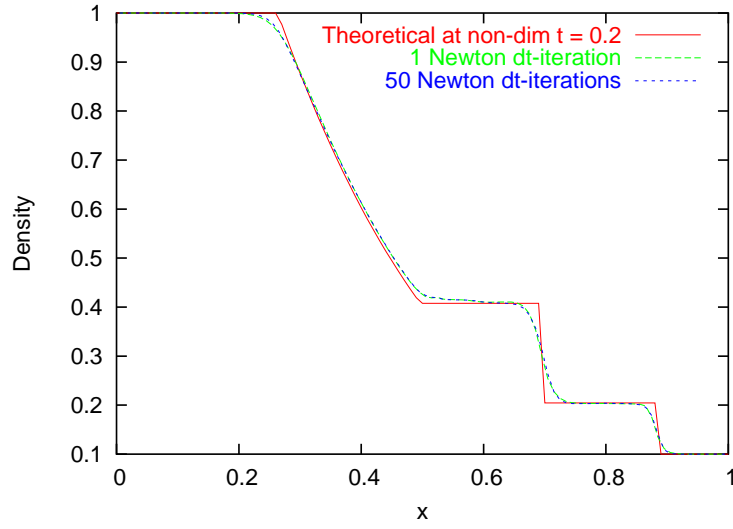


Figure 23: Shock-Tube Density at Non-Dimensional Time $t = 0.2$ - Newton comparison

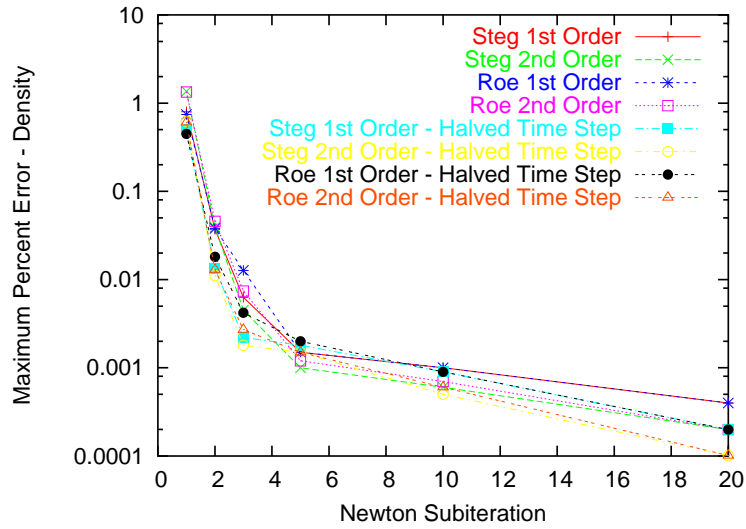


Figure 24: Maximum Error in Density vs Number of Newton dt-iterations

3.3 2D Vortex Shedding Cylinder

3.3.1 Case Presentation. The shock-tube provided insight into the ability of the code to accurately solve time resolved problems, but it is a very simple case. In order to more fully validate the code, more complex problems need to be considered. Shedding of vortices from a laminar cylinder in crossflow is a more complex flow over larger time scales. Experimental data shows(43) that for Re_D of 150 the Strouhal number (St) has a value slightly less than:

$$St = \frac{fD}{U} \approx 0.2 \quad (56)$$

The vortex shedding period, λ , may then be put in terms of Strouhal number via:

$$\lambda = \frac{U}{f} = \frac{D}{St} \approx \frac{D}{0.2} = 5D \quad (57)$$

A good visual check to see if the proper Strouhal number was calculated is to see if the distance between vortices is about equal to five cylinder diameters. Furthermore, for $Re_D < 180$, viscous effects quickly damp any flow velocity in the axial direction, reducing the problem to two dimensions. This makes for a relatively quick simulation with valuable results. The conditions chosen for this simulation are shown in Table 4. A Newton dt-iteration convergence study was performed for this case. The following number of dt-iterations were examined: 1, 3, 5, 10, and 20. Each Newton dt-iteration solved 60 symmetric Gauss-Seidel inner iterations unless an inner convergence tolerance of $1 \cdot 10^{-8}$ was met.

Table 4: Vortex shedding laminar cylinder example initial conditions

Property	Value
M	0.2
Re_D	150
T_{ref}	$500^\circ R$
Δt	$9.12 \cdot 10^{-5} \text{ s}$
Solver options: Steger-Warming Jacobians 2nd Order Spatial Differencing	

The time step used resulted in about 250 time steps between consecutively shedding vortices. This number provides enough data to statistically measure St . The grid used has dimensions of 401x201 and is shown in Figure 25. The cylinder has a non-dimensional

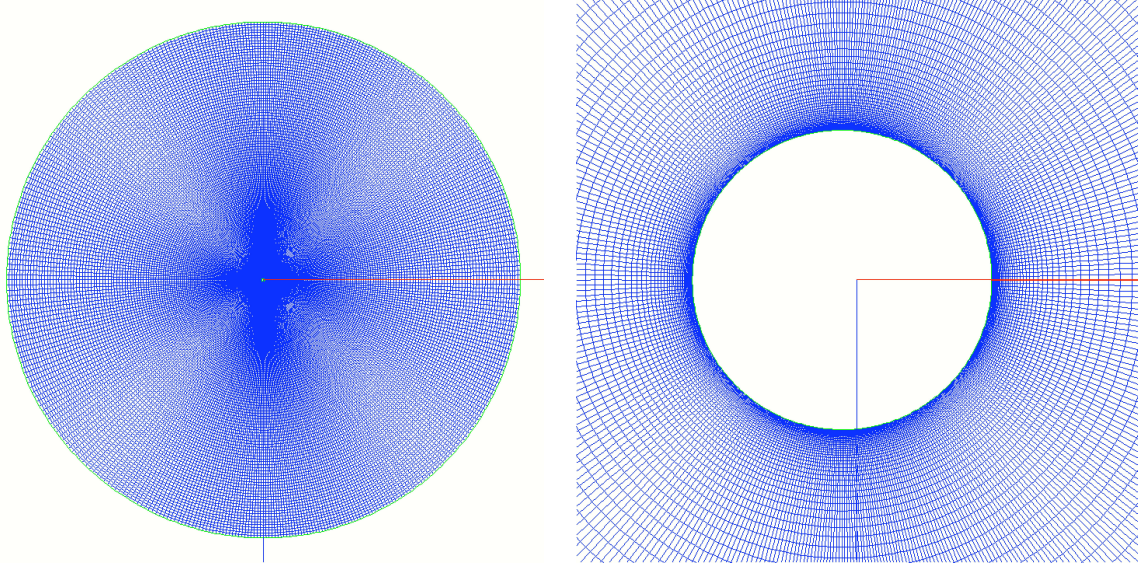


Figure 25: 2D Vortex Shedding Laminar Cylinder grid.

diameter of 1.0. The grid extends out 100 diameters with an initial spacing of 0.001 diameters. Similar to the laminar shock-tube, two different temporal discretization methods were evaluated, a 1st and 2nd order scheme. This case was run for 10,000 iterations. The last 4096 were statistically analyzed.

3.3.2 Results. The results for the 2D vortex shedding cylinder case are shown in Figures 26 to 31.

Figure 26 shows an example contour mach plot of the cylinder. The plot was made with data from using Roe RHS with 2nd order temporal discretization. All scheme combinations provided similar figures. Shedding vortices are clearly visible and a visual measurement of Strouhal number (Period ≈ 5 diameters) looks reasonable. The data was statistically analyzed to obtain more precise measurements.

Lift, drag, and time were recorded at each time step. An example plot of lift vs time is shown in Figure 27. Fast Fourier Transforms (FFT) were performed on the lift data to find the frequency of oscillation via a power spectrum density (PSD). The Strouhal number is determined from the largest peak on the PSD plot. The frequency output from the FFT was non-dimensionalized by the cylinder diameter and freestream velocity to form a Strouhal number. Figures 28 to 30 are a few of these PSD plots.

Figure 28 compares the temporal order discretization methods. Increased dissipation from numerical error stretches the shedding period. Stretching the shedding period results in a shortened frequency, which in turn predicts a small Strouhal number. The first order temporal discretization method slightly under-predicts Strouhal number compared to the second order discretization and, therefore, is showing more numerical dissipation than the second order temporal discretization method.

Figure 29 compares the different RHS methods. Using the same rationale as with the temporal comparison in the previous paragraph, it is apparent that Steger-Warming has more numerical dissipation than Roe.

Figure 30 shows a Newton dt-iteration comparison for the Roe RHS - 1st order temporal solver option combination. Three dt-iterations per time step and up all predicted the same Strouhal number slightly less than 0.2. However, the 1 dt-iteration per time step simulation case predicted a Strouhal number lower than all the other cases. Similar results were found with other solver option combinations as are shown in Appendix A.2.

The maximum lift was recorded for each shedding vortex, and the average value was found. Figure 31 shows average peak drag with respect to Newton dt-iterations. In general, one dt-iteration is far from a converged solution and three dt-iterations is well converged.

The solution is always converged for five dt-iterations or greater. Similar plots were made with other properties as shown in Appendix A.2. All results showed the same trends. Therefore, the author recommends using between three and five dt-iterations to properly converge each time iterations for unsteady turbulent flow.

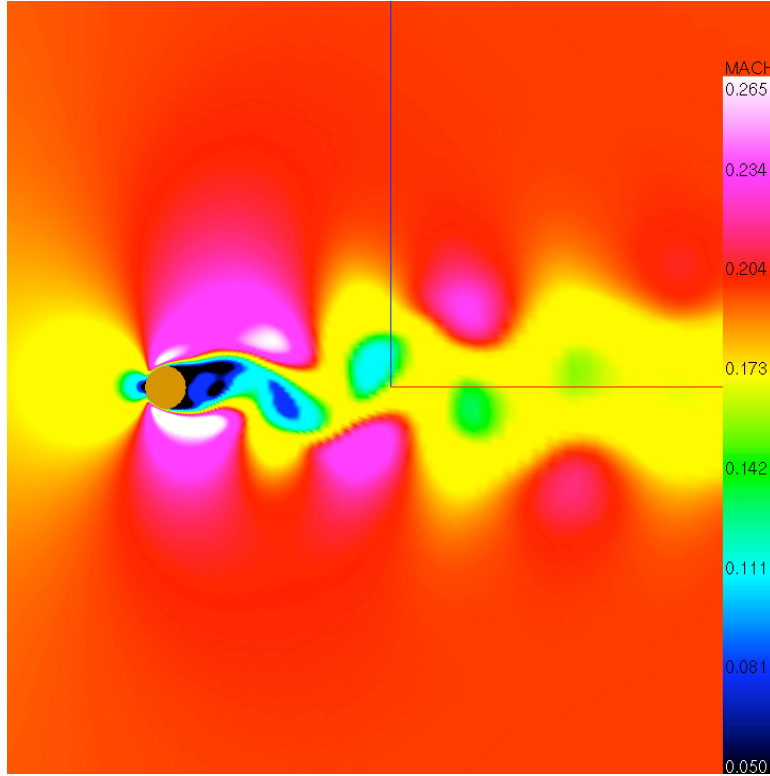


Figure 26: Mach contours of vortex shedding laminar cylinder

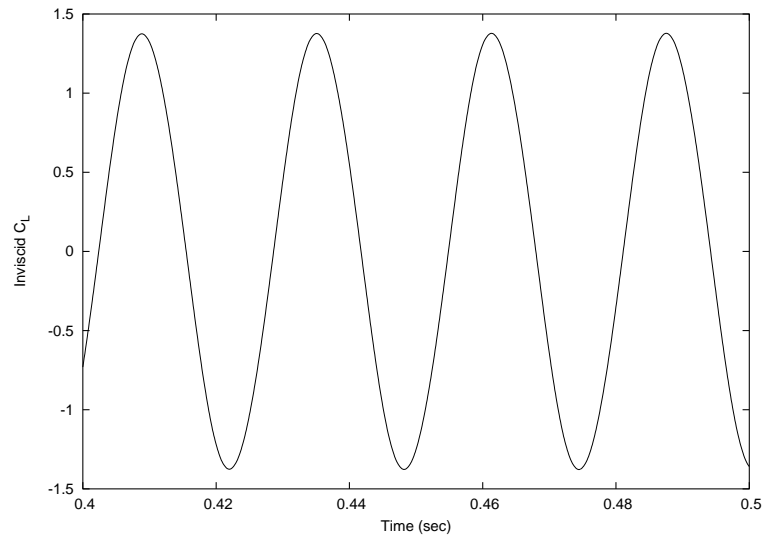


Figure 27: Lift vs Time

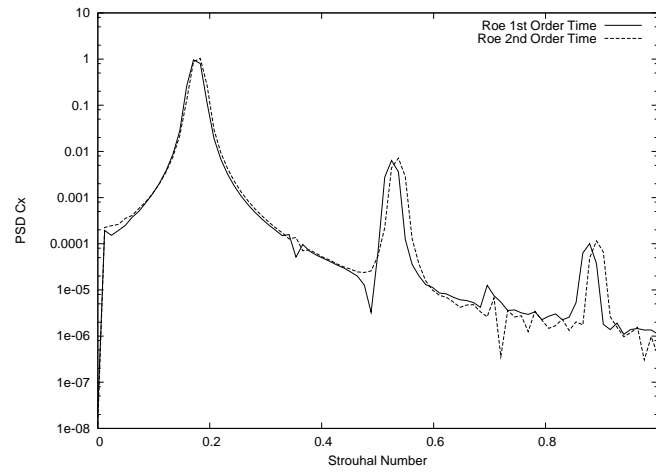


Figure 28: PSD of St from Lift - Temporal Order Comparison

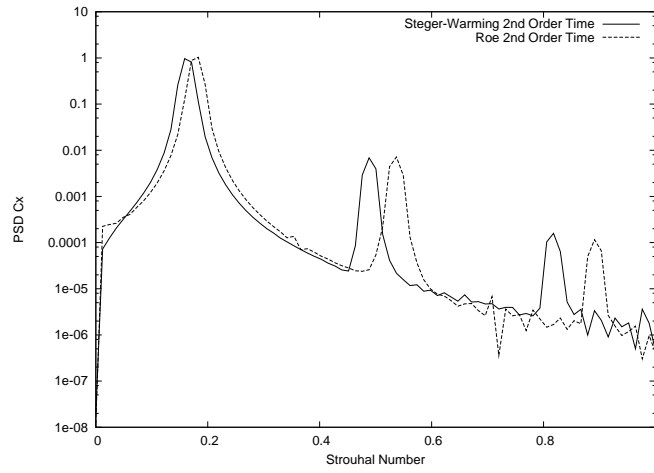


Figure 29: PSD of St from Lift - RHS Comparison

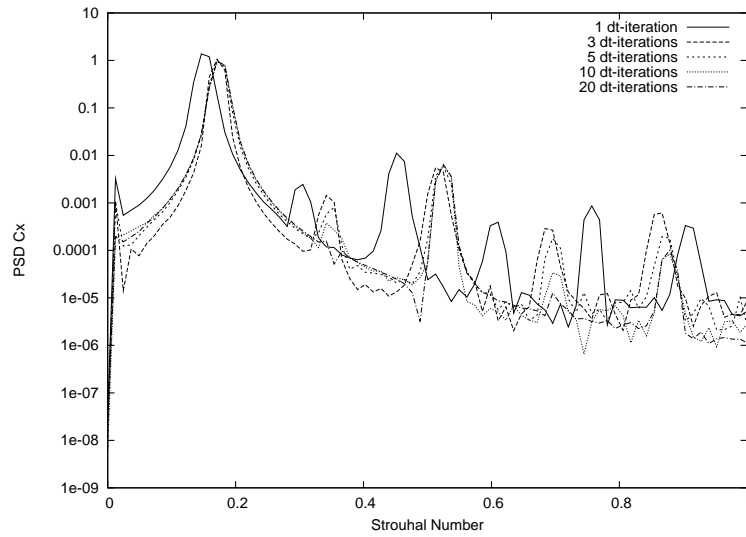


Figure 30: PSD of St from Lift - Roe - 1st Order Temporal

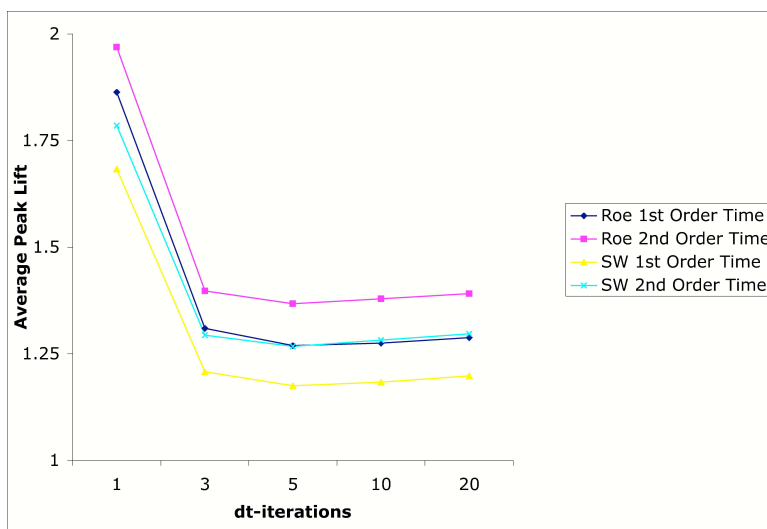


Figure 31: Average Peak Lift vs dt-iteration

3.4 *Conclusions*

To properly simulate unsteady turbulent flow, it is important to reduce artificial dissipation and accurately calculate each time step. The inviscid convecting vortex provided useful data about the contribution of each solver option to artificial dissipation, while the shock-tube and $2D$ cylinder were most beneficial in the area of time step convergence. Reviewing the non-turbulent cases, the conclusions are drawn that the following solver options should be implemented in the Beggar code to simulate unsteady turbulent flow:

1. A second order temporal discretization
2. Between three and five Newton dt-iterations

The Roe method ultimately was used to compute the RHS for the cases in Chapter 4 because it has been shown to have less numerical dissipation. However, more investigation should be done on the instabilities it showed in the inviscid vortex case.

IV. TURBULENT STUDY

With the Beggar code validated for unsteady flows, the turbulence models may now be inspected. Many of the turbulence models used today were developed for steady-state RANS flow solvers. They include significant numerical dissipation to wash out oscillations and rapidly converge to a steady state solution. This numerical dissipation will allow a steady-state problem to converge much quicker, but it may destroy the ability of the code to predict unsteady flow. Therefore, unsteady cases must be simulated in order to validate a turbulence model for unsteady flow. The unsteady turbulent validation cases selected for this effort are a 2D oscillating airfoil, a 3D turbulent shedding cylinder, and a turbulent cavity.

4.1 2D Oscillating Airfoil

4.1.1 Case Presentation. A simple turbulent case is that of an oscillating (pitching) 2D airfoil. The time dependance of the angle of attack, α , is given by

$$\alpha = \alpha_o + 4.2^\circ \sin(20\pi t) \quad (58)$$

Two α_o 's were investigated, $\alpha_o = 4.0^\circ$ and $\alpha_o = 11.0^\circ$. For the $\alpha_o = 4.0^\circ$ case, the α 's are kept small so that the flow always remains attached to the airfoil(13). With the flow always attached, Baldwin-Lomax would be expected to perform as well as Spalart-Allmaras and DES. For the $\alpha_o = 11.0^\circ$ case, the flow separates on the upper surface of the airfoil. Here, Spalart-Allmaras would be expected to outperform Baldwin-Lomax.

A NACA 0015 airfoil with a non-dimensional chord of 1.0 was discretized using two overlapping grids. The region closest to the airfoil is covered by a C-grid with dimensions 381x55. This airfoil grid extends 1 chord away from the airfoil and 6 chords behind the airfoil. The initial non-dimensional spacing off the airfoil is $\Delta x = 0.00001$. Figure 32 shows the airfoil grid and Figure 33 shows the airfoil zoomed in at the trailing edge. To oscillate the airfoil, the airfoil grid is rotated inside a larger stationary cartesian grid. This grid has dimensions 141x81 with lengths of 31x20 chord lengths. Figure 34 shows the cartesian grid with cells cut out where the airfoil resides. To achieve time accurate results, five Newton dt-iterations were run every time iteration. Each Newton dt-iteration solved 80 symmetric Gauss-Seidel inner iterations unless an inner convergence tolerance of $1 \cdot 10^{-8}$ is met.

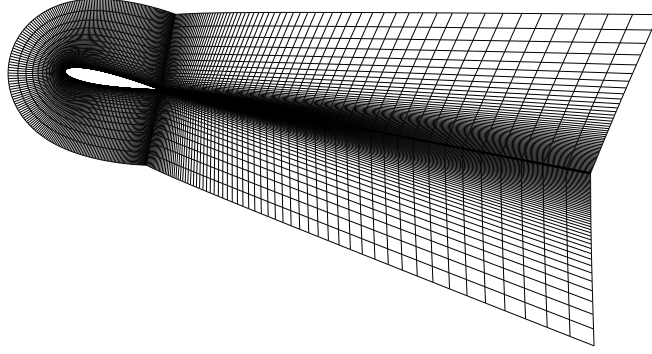


Figure 32: NACA 0015 Grid

Turbulence models to be examined include Baldwin-Lomax, Spalart-Allmaras, and a DES model. The input conditions are shown in Table 5.

Table 5: 2D oscillating airfoil example initial conditions

Property	Value
M	0.29
Re_c	$1.95 \cdot 10^6$
Δt ($\alpha_o = 4.0^\circ$)	$2.24 \cdot 10^{-4}$ s
Δt ($\alpha_o = 11.0^\circ$)	$3.125 \cdot 10^{-5}$ s
Solver options: Steger-Warming Jacobians 2nd Order Spatial Differencing Roe Right Hand Side 5 dt-iterations	

To ensure time convergence is not an issue, two time step sizes were investigated with the $\alpha_o = 4.0^\circ$ case. The time step of $\Delta t = 2.24 \cdot 10^{-4}$ was halved, and twice as many iterations should return the same solution.

The experimental data was gathered from reference (27). Pressure transducers were placed at four stations along the span of a 60 inch semispan NACA 0015 wing with a 12.0

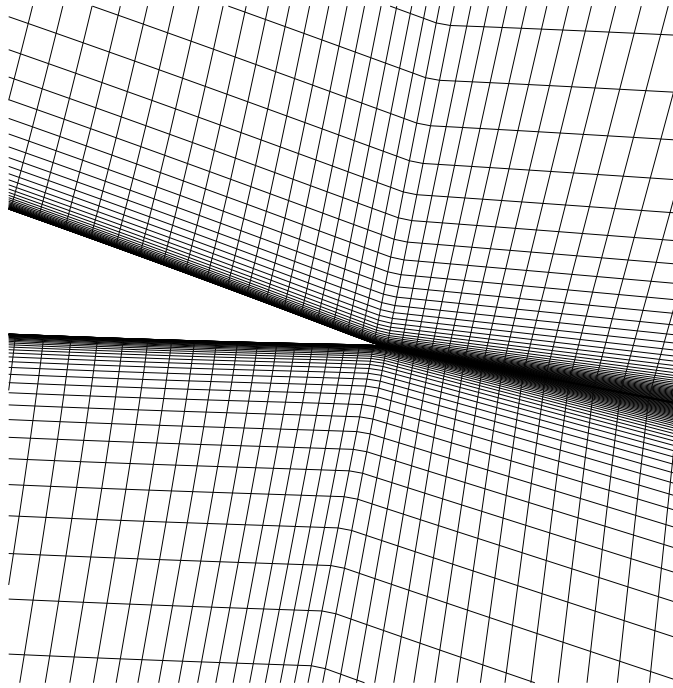


Figure 33: NACA 0015 Grid - Zoomed in on Trailing Edge

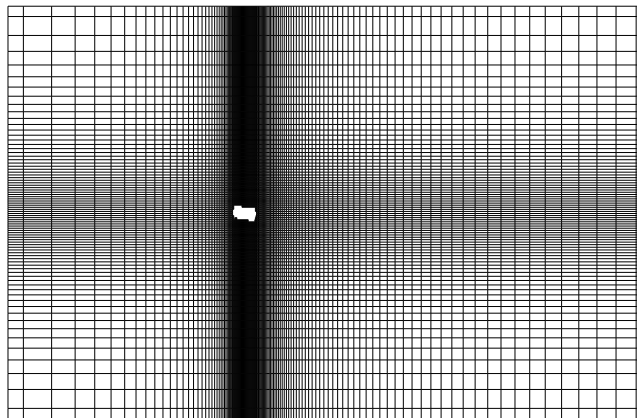


Figure 34: Cartesian Grid

inch chord with zero twist. The main station located at mid-span included 20 pressure transducers along the chord. The three off-center stations were used to check the two-dimensionality for each data point. Measurements were taken 240 times per oscillation. The pressure transducer output was then sent through a 500 Hz low pass filter. Because the experimental data was only taken at 20 points along the chord and then sent through a filter, the net effect of the experimental setup was that the unsteady data are highly filtered(23).

4.1.2 Results. Results for the 2D oscillating airfoil are shown in Figures 35 through 46. Figures 35 through 40 apply to the $\alpha_o = 4.0^\circ$ simulations while Figures 41 through 46 apply to the $\alpha_o = 11.0^\circ$ simulations. The $\alpha_o = 4.0^\circ$ case is an attached flow case(13) whereas the $\alpha_o = 11.0^\circ$ case has separation near the trailing edge as the airfoil pitches up (upstroke) and no separation as the airfoil pitches down (downstroke).

Figures 35 through 37 show lift, drag, and pitching moment coefficients as a function of angle of attack. A circuit is formed on each due to the induced angle of attack from the oscillation. All models accurately calculated the lift coefficient as seen in Figure 35. Figure 36 shows all three of the models under-predicting C_D at $\alpha = -0.2^\circ$. This phenomena has been seen in other codes for the Baldwin-Lomax and Spalart-Allmaras models(13, 35, 22). All of the models match each other well for C_L and C_D . Baldwin-Lomax diverges from Spalart-Allmaras and DES in the downstroke portion of the C_M curve as shown in Figure 37. To investigate this, plots of u -velocity were made near the trailing edge of the airfoil at $\alpha = 5.22^\circ$ on the downstroke. Figure 38 shows the Baldwin-Lomax prediction and Figure 39 shows the Spalart-Allmaras prediction. Baldwin-Lomax has a large region of negative velocity, indicating that it is predicting separation on the trailing edge. The flow remains attached in the Spalart-Allmaras prediction, as there is no negative velocity. As noted by Wilcox(45), algebraic models usually predict too much separation. It appears this may be the case.

Simulations with a halved time step were also run to see if the solution was time converged. Figure 40 shows the C_M predicted with the Baldwin-Lomax model for the halved time step compared with the whole time step. There is some variation at high angles of attack on the downstroke where Baldwin-Lomax predicted separation. Otherwise, the plots lie on top of each other. Furthermore, Spalart-Allmaras and DES predictions for lift, drag, or moment coefficient did not change when the time step was halved. It is therefore assumed that the time step has been converged.

Figures 41 through 43 show lift, drag, and pitching moment coefficients as a function of angle of attack for the $\alpha_o = 11.0^\circ$ simulations. At this angle of attack and Reynolds number, separation is expected on the upstroke and disappears on the downstroke. This is

known as a light dynamic stall case. This is a good case to run to test turbulence models, as light dynamic stall is sensitive to the onset of separation.

A common trend among the three models is that they all performed poorly for the $\alpha_o = 11.0^\circ$ case. None of the models resemble the lift coefficient curve in Figure 41. All the models predicted a rounded end at $\alpha = 6.8^\circ$ and a point at $\alpha = 15.2^\circ$, where data shows the opposite. There are severe oscillations in the Baldwin-Lomax curve, indicating that the airfoil is shedding vortices.

(35), (13:Ko), and (23) obtained different results for this case with the Spalart-Allmaras model. They found that the Spalart-Allmaras model matched well with experimental data for lift and drag, and had the same shape of curve for C_m . Ko is the only one who also compared Baldwin-Lomax. Ko's version of Baldwin-Lomax predicted the same plot on the upstroke of Figure 41, but did not predict shedding on the downstroke.

Figures 44, 45, and 46 show vorticity predictions at the trailing edge of the airfoil for Baldwin-Lomax, Spalart-Allmaras, and DES models, respectively. As seen in these figures, large vortical structures are shedding from the airfoil in the Baldwin-Lomax simulation, whereas no vortices are being shed from either the Spalart-Allmaras or DES simulations. Examining the velocity vectors showed that Baldwin-Lomax predicted separation a tenth of a chord length sooner than Spalart-Allmaras and DES. This distance, combined with the fact that the airfoil has more curvature closer to the leading edge and therefore a more adverse pressure gradient, could be the reason Baldwin-Lomax is predicting vortex shedding while Spalart-Allmaras and DES are not. Recalling that Baldwin-Lomax also predicted separation for the $\alpha_o = 4.0^\circ$ case, a good assumption is that Baldwin-Lomax is predicting separation too early. Reasons why Beggar's Spalart-Allmaras data does not match well with experimental data or data gathered from other versions of the Spalart-Allmaras model cannot be determined, but the question is raised as to whether the Spalart-Allmaras model was coded into Beggar properly.

The clock times were recorded for the $\alpha_o = 4.0^\circ$ cases. The total time was divided by the total number of iterations to come up with the times per iteration as shown in Table 6. Because Spalart-Allmaras and DES have to solve an extra differential equation, all things being equal it is expected that those simulations would take longer than Baldwin-Lomax.

Table 6: Average computation time for various turbulence models for the oscillating airfoil case

Model	Time per Iteration Normalized by Baldwin-Lomax
Baldwin-Lomax	1.0
Spalart-Allmaras	1.27
DES	1.16

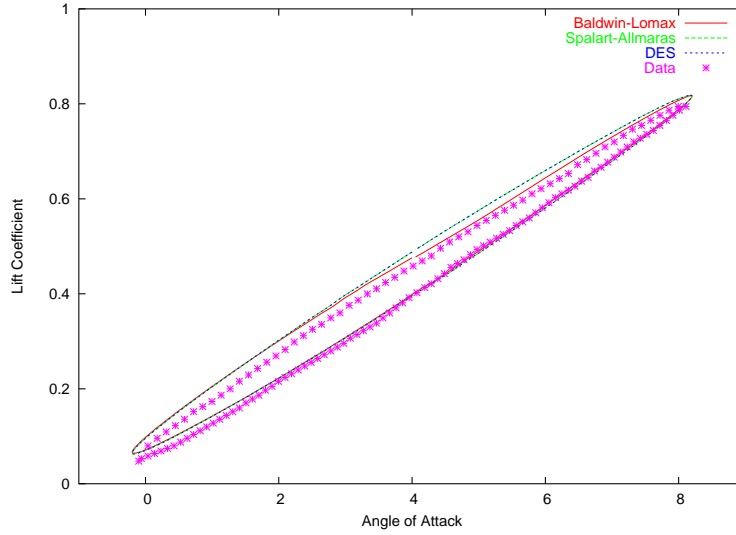


Figure 35: $\alpha_o = 4.0^\circ$ - Lift Coefficient vs α

However, since Baldwin-Lomax predicted shedding vortices and the Spalart-Allmaras model did not, the Baldwin-Lomax model had more gradients to solve for and the number of inner iterations needed to converge each Newton dt-iteration was much higher.

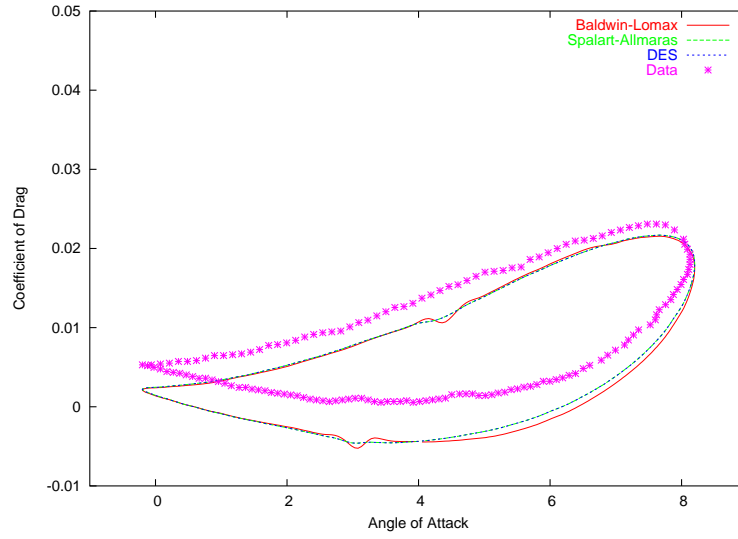


Figure 36: $\alpha_o = 4.0^\circ$ - Drag Coefficient vs α

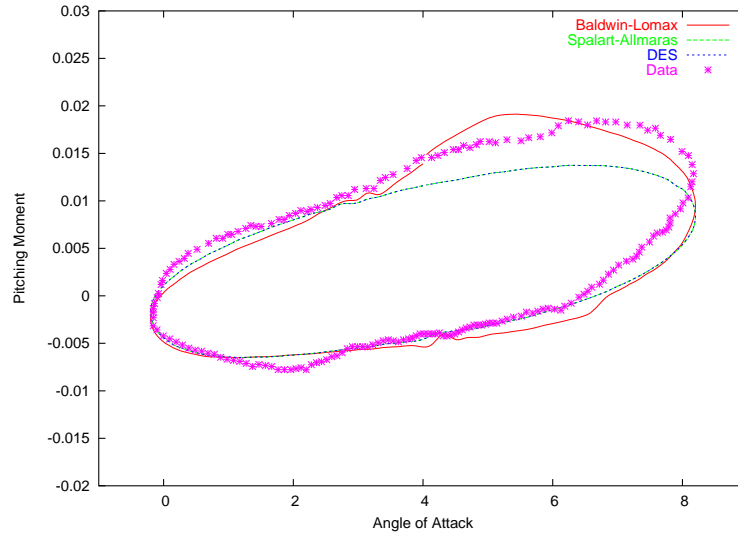


Figure 37: $\alpha_o = 4.0^\circ$ - Pitching Moment Coefficient vs α

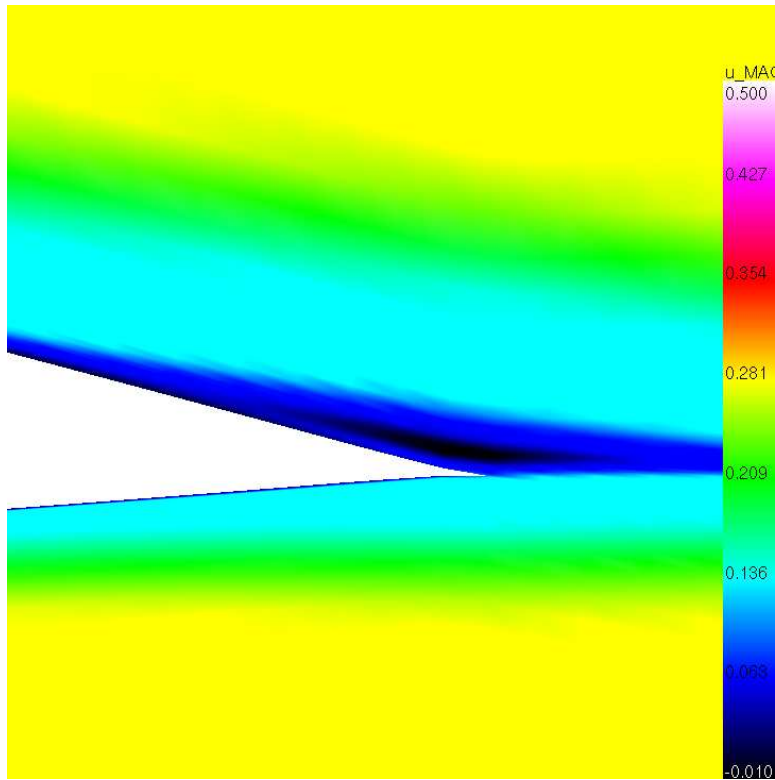


Figure 38: u Velocity - $\alpha = 5.22^\circ$ - Downstroke- Baldwin-Lomax

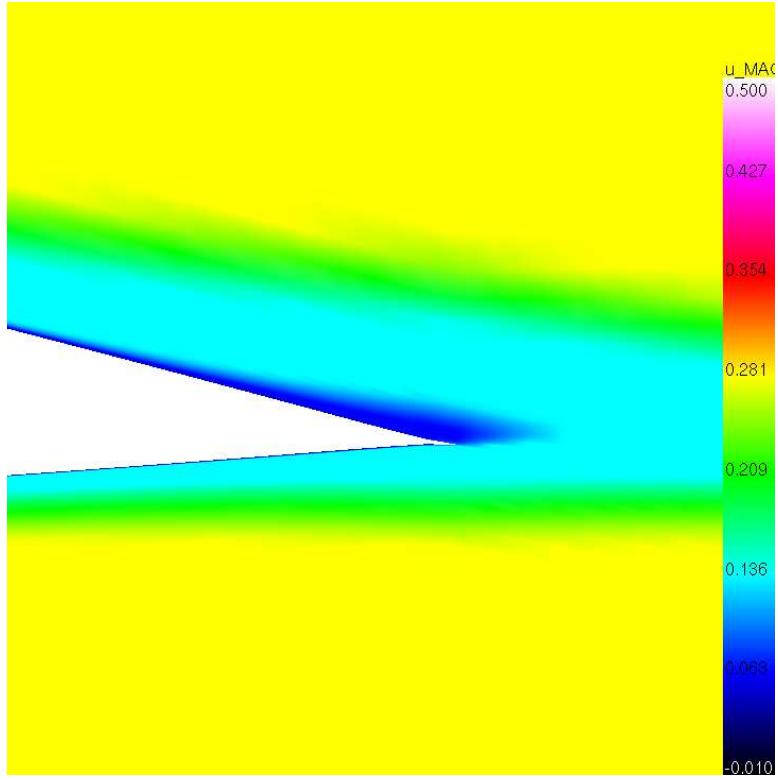


Figure 39: u Velocity - $\alpha = 5.22^\circ$ - Downstroke- Spalart-Allmaras

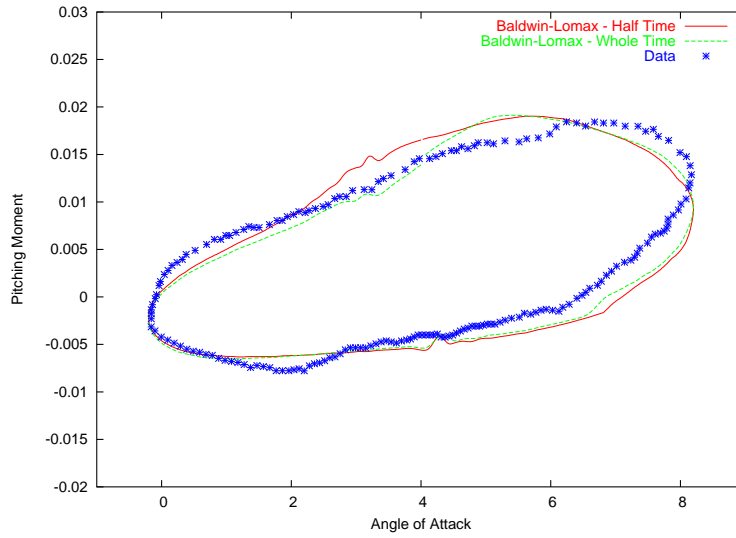


Figure 40: $\alpha_o = 4.0^\circ$ - Pitching Moment Coefficient vs α - Half Time Comparison

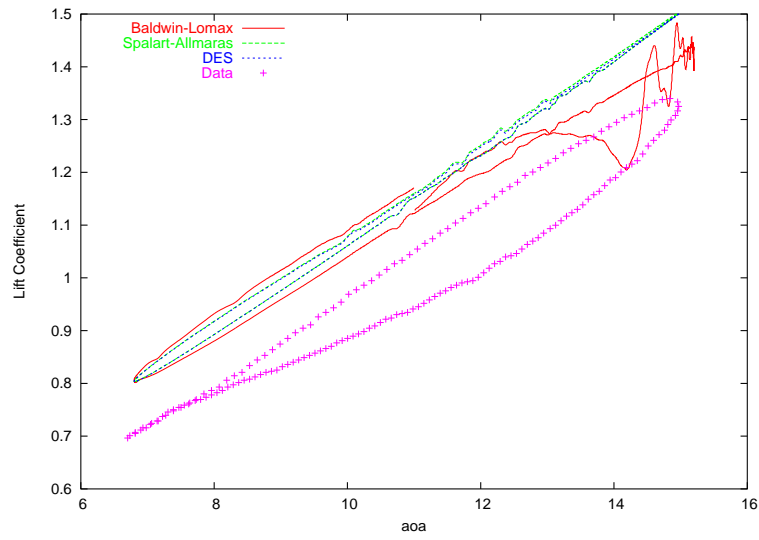


Figure 41: $\alpha_o = 11.0^\circ$ - Lift Coefficient vs α

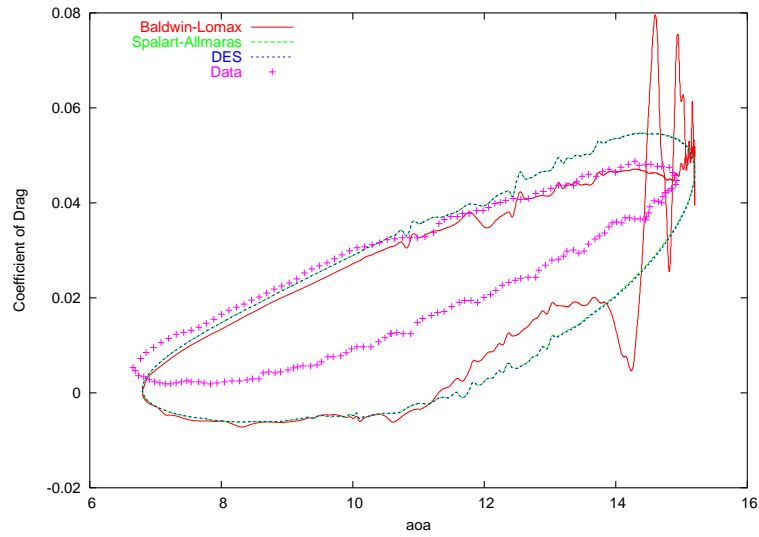


Figure 42: $\alpha_o = 11.0^\circ$ - Drag Coefficient vs α

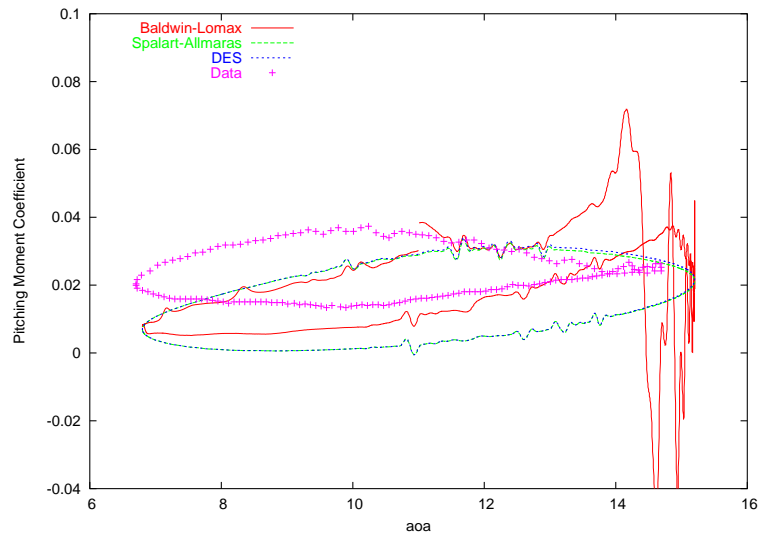


Figure 43: $\alpha_o = 11.0^\circ$ - Pitching Moment Coefficient vs α

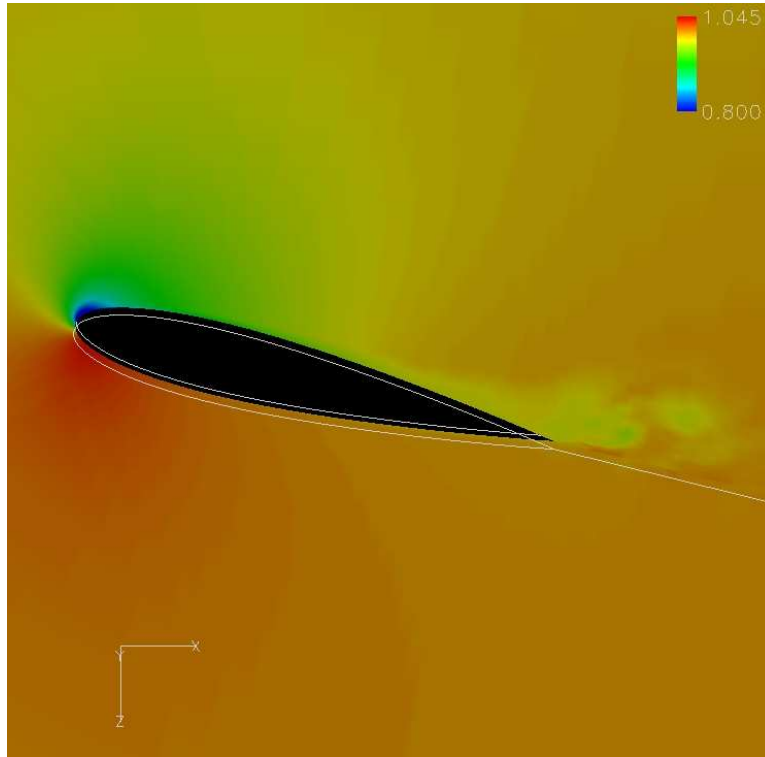


Figure 44: Instantaneous Vorticity - $\alpha_o = 11.0^\circ$ - $\alpha = 13.97^\circ$ Downstroke - Baldwin-Lomax

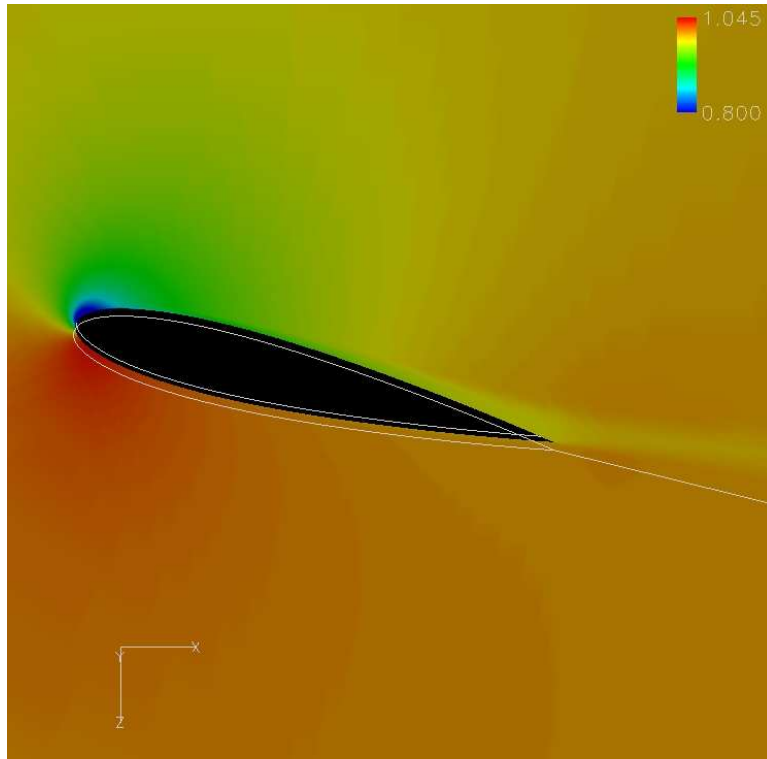


Figure 45: Instantaneous Vorticity - $\alpha_o = 11.0^\circ$ - $\alpha = 13.97^\circ$ Downstroke - Spalart-Allmaras

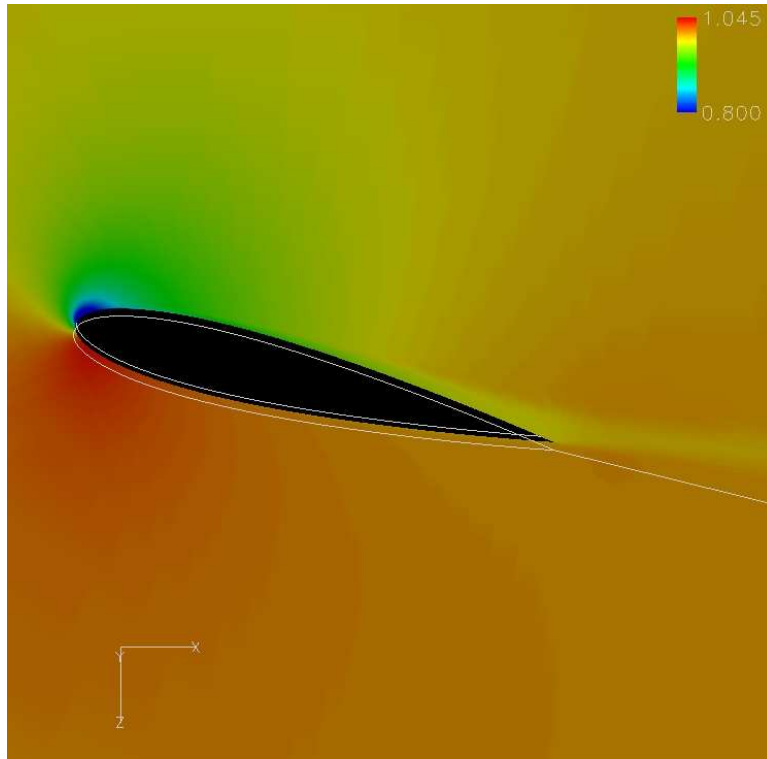


Figure 46: Instantaneous Vorticity - $\alpha_o = 11.0^\circ$ - $\alpha = 13.97^\circ$ Downstroke - DES

4.2 3D Vortex Shedding Cylinder

4.2.1 Case Presentation. A vortex shedding turbulent cylinder is significantly more difficult than the 2D case examined in Chapter III. With a $Re > 180$, the flow can no longer be approximated as 2D. A vortex may be shedding from the top of the cylinder at one point along the span on the cylinder while another vortex is shedding from the bottom of the cylinder at a different point. Due to computational and time constraints and some technical difficulties, only a coarse mesh study was performed. With the coarse mesh, DES will have difficulty performing well. With the larger cells in the wake, only the largest of the eddies will be captured by the grid and DES will rely on the sub-grid model to account for the rest of the eddies.

The dimensions of the grid are 101x73x51. The initial spacing off the wall is 1.0×10^{-5} which gives a $y^+ \approx 1.0$. The cylinder has a non-dimensional diameter of 1.0, a length of 10 chords, and the grid extends 50 chords from the cylinder. Initial conditions are shown in Table 7. To achieve time accurate results, five Newton dt-iterations were run every time step. Each Newton dt-iteration solved 80 symmetric Gauss-Seidel inner iterations unless an inner convergence tolerance of $1 \cdot 10^{-8}$ was met.

Table 7: Vortex shedding turbulent cylinder example initial conditions

Property	Value
M	0.2
Re_D	$8 \cdot 10^6$
Δt	$9.0 \cdot 10^{-5}$ s
Solver options: Steger-Warming Jacobians 2nd Order Spatial Differencing Roe Right Hand Side 5 dt-iterations	

4.2.2 Results. Results for the 3D vortex shedding cylinder are shown in Figures 48 through 57. Pressure coefficient and time was recorded for every time iteration at a point on top of the cylinder. This data was passed through a Fast Fourier Transform to find the PSD's of the shedding frequency. The shedding frequency was non-dimensionalized which results in Strouhal number.

Figure 47 is a sample pressure coefficient vs time plot from data gathered at the top of the cylinder. Figure 48 shows the PSD with respect to St computed from data gathered at the top of the cylinder. Experiment(10) shows for $Re_D = 8 \cdot 10^6$,

$$St \approx 0.306 - 0.308$$

Figure 48 shows both the Spalart-Allmaras and DES models underpredicted the Strouhal number by about $\frac{2}{3}$. Baldwin-Lomax predicts a Strouhal number about $\frac{1}{3}$ the value of the experimental data. The smaller turbulent frequencies in the Baldwin-Lomax simulation are overshadowing the vortex shedding frequency.

Figures 49 to 51 show instantaneous plots of total pressure from a cross-sectional view for the Baldwin-Lomax, Spalart-Allmaras, and DES models, respectively. In each diagram shedding vortices are present. Spalart-Allmaras and DES predict periodic shedding vortices, whereas the Baldwin-Lomax model predicts randomly shedding vortices.

Figures 52 to 54 show instantaneous plots of vorticity on the wake surface behind the cylinder and the wall perpendicular to the cylinder. Three dimensional structures are evident in the Baldwin-Lomax simulation, as seen in Figure 52. However, it appears that Spalart-Allmaras and DES are predicting 2D vortex shedding. To investigate this, cross sectional plots of velocity parallel to the cylinder were made, as shown Figures 55 to 57. Significant velocity parallel to the cylinder is present in the Baldwin-Lomax simulation, Figure 55. The Spalart-Allmaras and DES simulations predict almost no velocity parallel to the cylinder, as seen in Figures 56 and 57 respectively.

Table 8 shows drag coefficient and Strouhal number data compared to experimental data and other CFD results. The average C_D matches well for Baldwin-Lomax, but the

Table 8: Force coefficient and Strouhal number data

Model	Average C_d	St
Baldwin-Lomax	0.557	0.11
Spalart-Allmaras	0.193	.195
DES	0.189	0.195
Spalart-Allmaras (25)	0.226	0.232
DES (25)	0.298	0.232
Data (10)	0.505-0.540	0.306-0.308

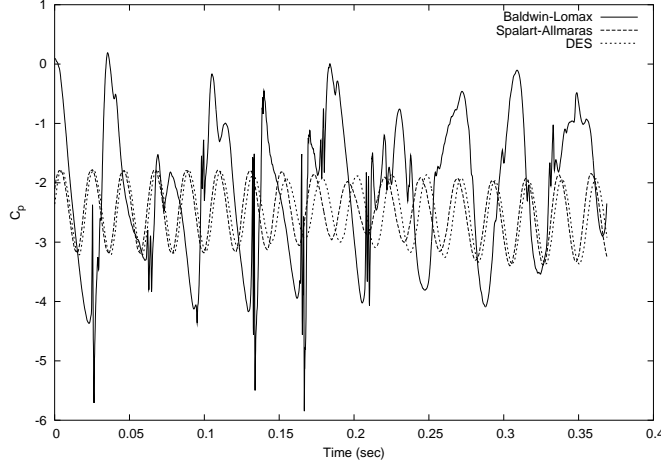


Figure 47: C_p vs Time

Strouhal number was underpredicted. The Spalart-Allmaras and DES models do not match the average C_D or St . Using the same grids and turbulence model, the Spalart-Allmaras simulation with Beggar predicted a C_D 15% lower than predicted with the NXAIR(25) code. These results strengthen the belief that the Spalart-Allmaras model was not properly written in the Beggar code.

All cases were run on a 1.8 GHz Opteron workstation with eight gigabytes of memory. The wall clock times for each 3D cylinder run were recorded. The average time per iteration for each turbulence model is shown in Table 9, which shows DES and Spalart-Allmaras taking about the same time. Baldwin-Lomax took about 1.5 times longer to solve each time step. As described previously, Spalart-Allmaras overdamped the unsteady effects which would make converging each time step simpler. If the same amount of unsteady effects were present in all cases, one would expect Spalart-Allmaras to take longer to solve than Baldwin-Lomax.

Table 9: Average computation times for various turbulence models for the 3D cylinder case

Model	Time per Iteration Normalized by Baldwin-Lomax
Baldwin-Lomax	1.0
Spalart-Allmaras	0.62
DES	0.62

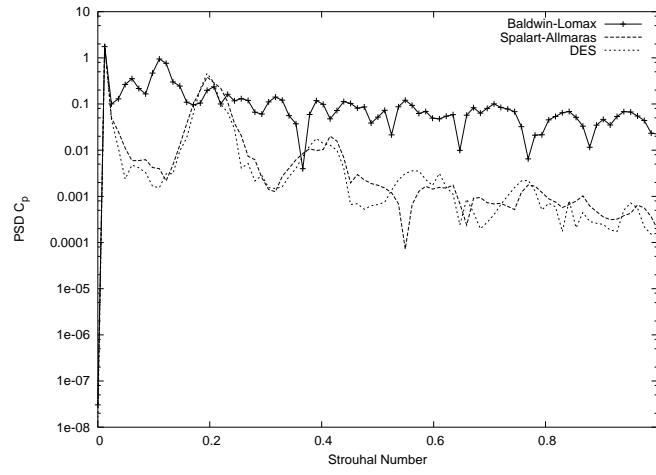


Figure 48: PSD of St

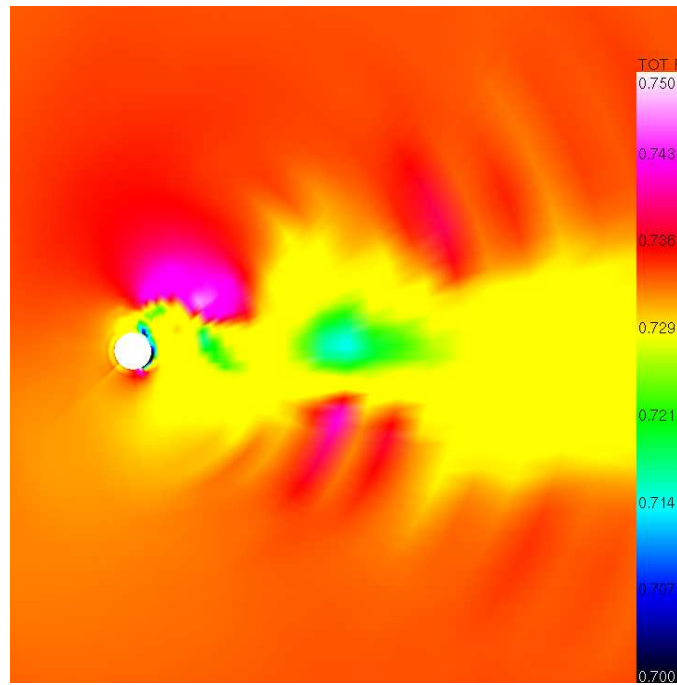


Figure 49: Instantaneous Total Pressure Plot - Baldwin-Lomax

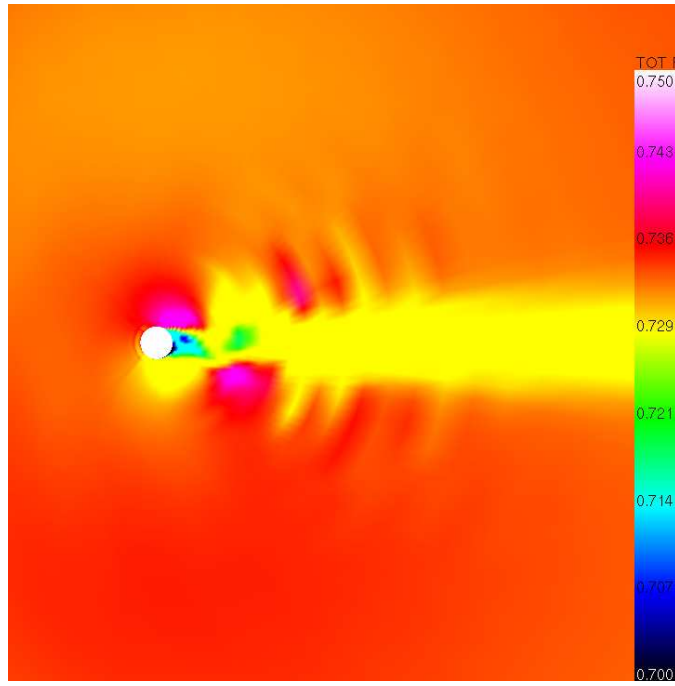


Figure 50: Instantaneous Total Pressure Plot - Spalart-Allmaras

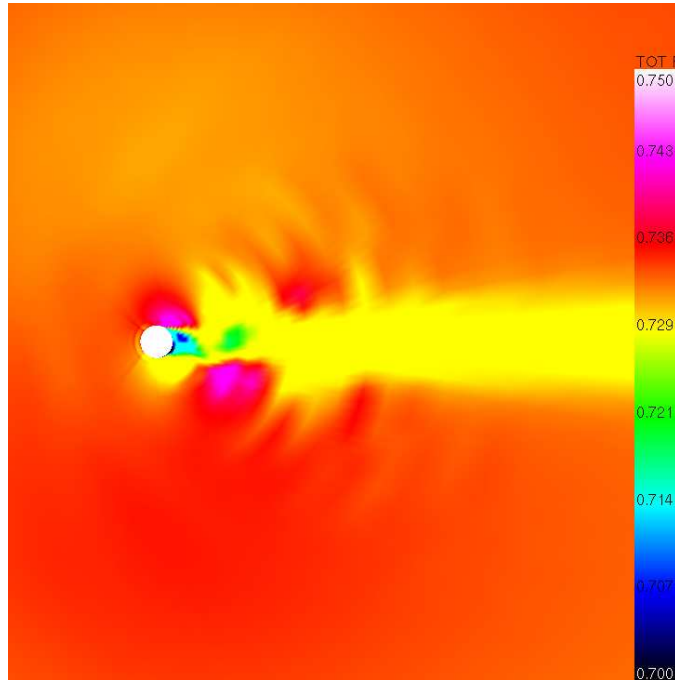


Figure 51: Instantaneous Total Pressure Plot - DES

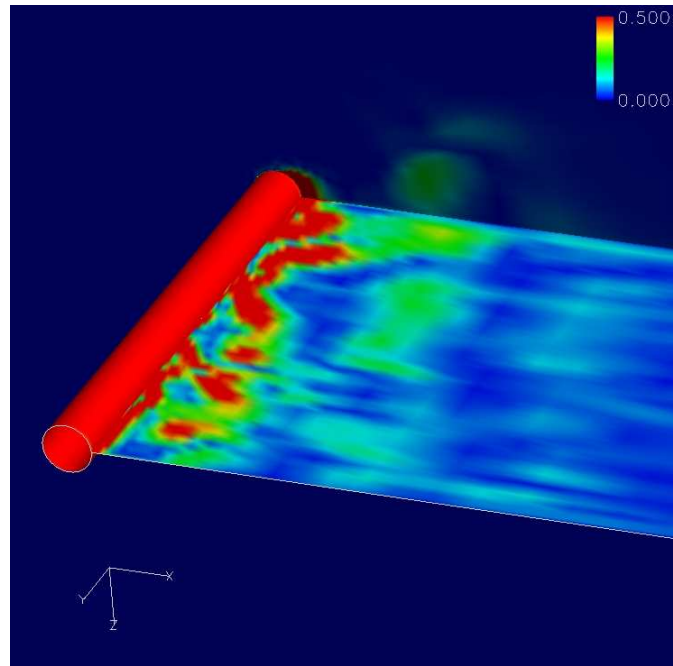


Figure 52: Instantaneous Vorticity Plot - Baldwin-Lomax

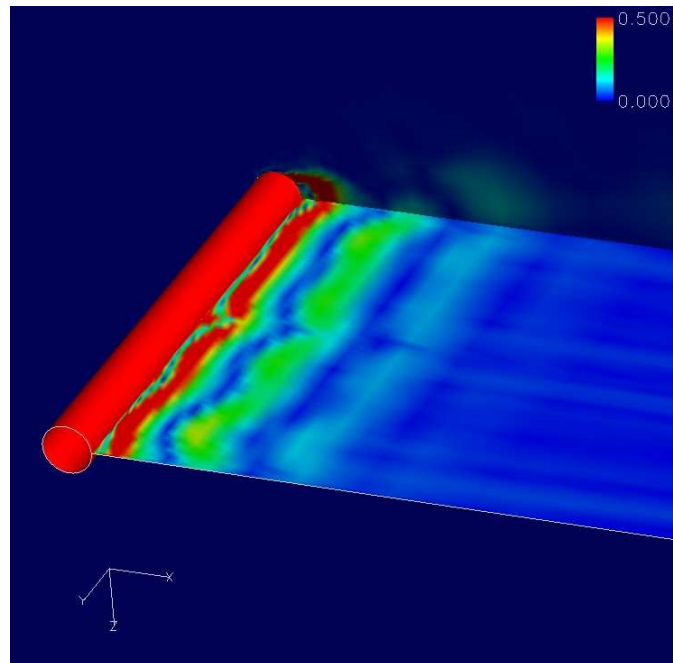


Figure 53: Instantaneous Vorticity Plot - Spalart-Allmaras

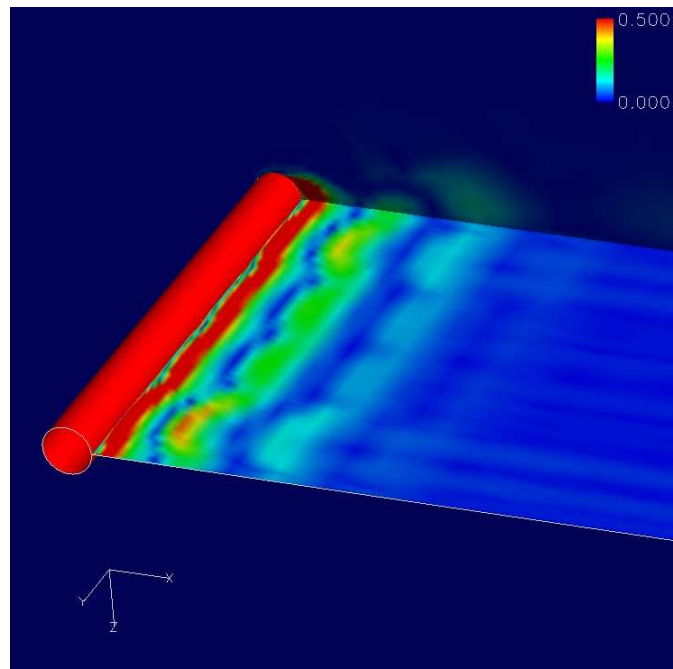


Figure 54: Instantaneous Vorticity Plot - DES

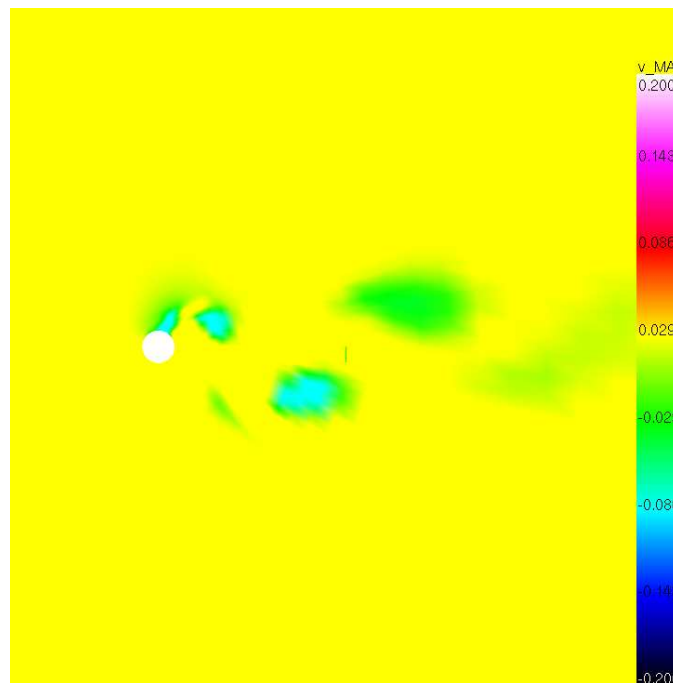


Figure 55: Velocity Parallel to the Cylinder - Baldwin-Lomax

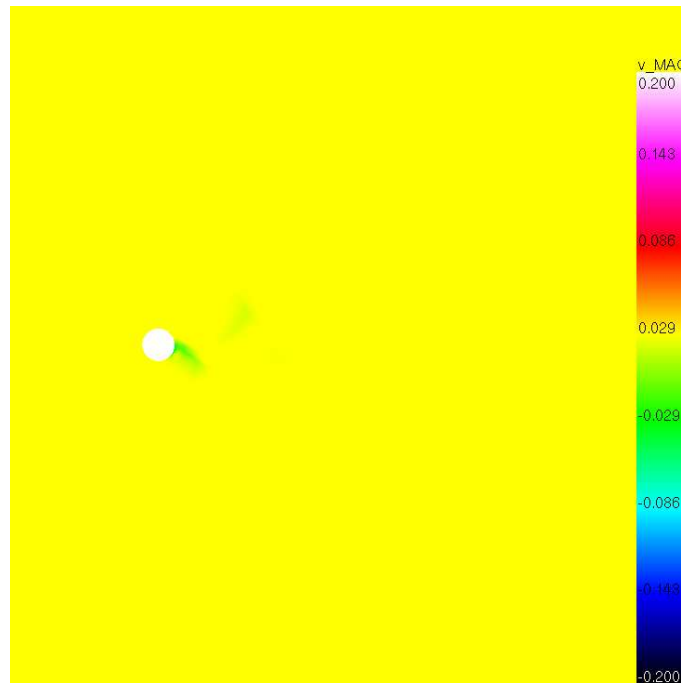


Figure 56: Velocity Parallel to the Cylinder - Spalart-Allmaras

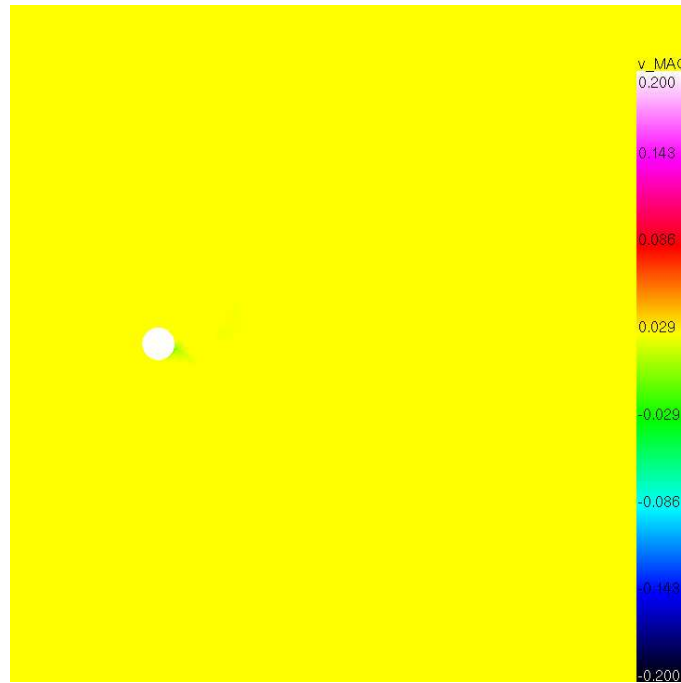


Figure 57: Velocity Parallel to the Cylinder - DES

4.3 Turbulent Cavity

4.3.1 Case Presentation. An unsteady simulation of the Weapons Internal Carriage and Separation (WICS) weapons bay was also investigated. The bay has the physical dimensions of 18x4x4 inches. The bay was placed inside grids that extend 15 inches upstream of the bay and 25 inches downstream of the bay. This matches the experimental setup(5). A grid converge study was performed for this case. Information about each grid is shown in Table 10 and the grids are shown in Figure 58.

Table 10: Turbulent cavity grid specifications

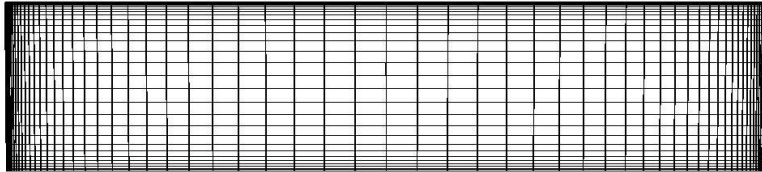
Grid	Total Points	Bay Grid Dimensions	Bay Grid Δx_{\max}	Bay Grid Δy_{\max}	Bay Grid Δz_{\max}
Fine	1.9×10^6	133x137x61	0.3 in	0.1 in	0.1 in
Medium	1.1×10^6	76x47x41	0.6 in	0.2 in	0.2 in
Coarse	7.9×10^5	61x31x31	0.75 in	0.3 in	0.3 in

Initial conditions are shown in Table 11. To achieve time accurate results, three Newton dt-iterations were run every time step. Each Newton dt-iteration solved 60 symmetric Gauss-Seidel inner iterations unless an inner convergence tolerance of $1 \cdot 10^{-8}$ was met.

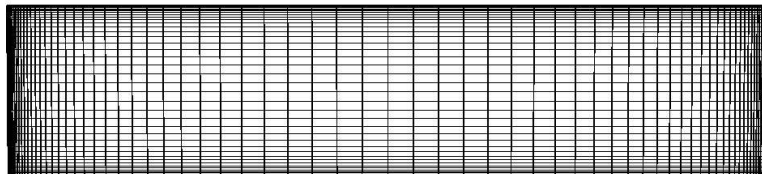
Table 11: Turbulent cavity example initial conditions

Property	Value
M	0.95
Re	$2.1 \cdot 10^5 \frac{1}{ft}$
Δt	$8.0 \cdot 10^{-6}$ s
Solver options: Steger-Warming Jacobians 2nd Order Spatial Differencing Roe Right Hand Side 3 dt-iterations	

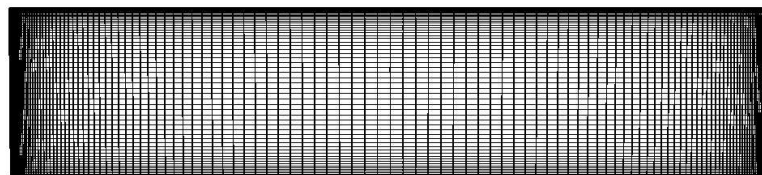
Wind tunnel data has been gathered(5) from the AEDC four-foot transonic wind tunnel using two transducers, labeled K16 and K18. Transducer K-16 was located on the centerline of the bay ceiling 0.275 inches from the back wall while K-18 was located on the centerline of the back wall 0.725 inches from the bay opening. CFD data was gathered at the same locations and compared with the experimental data.



Coarse



Medium



Fine

Figure 58: Bay Grids

4.3.2 Results. Results for the turbulent cavity case are shown in Figures 59 through 65. Figures 59 through 62 compare data gathered from using the different models to the experimental data. In these plots, the Spalart-Allmaras model was far from matching the experimental data. The decibel reading from the Spalart-Allmaras model in Figure 59 was about 40 dB less than the experimental data. Only a few frequencies have strong decibels readings with the Spalart-Allmaras model. This indicates that only the largest fluctuations are strong enough to propagate all the way to the bay ceiling and all the other fluctuations are damped out by the model. Baldwin-Lomax and DES were both in good agreement with the experimental data. (37:Suhs) also found Baldwin-Lomax to be in good agreement with the experimental data. DES does a better job at matching the first peak. This simulation was also run by (23:Nichols), whose data shows good agreement with the Spalart-Allmaras model until a frequency of 1000 Hz. After 1000 Hz, the Spalart-Allmaras model underpredicted the sound level by about 20 decibels. As described in Section 2.7, the only difference between the Spalart-Allmaras and DES models is that when the distance to the nearest wall gets larger than 0.65 times the largest cell dimension, then that value is used in place of the distance to the wall to solve the additional PDE. With such a large difference in results between the Spalart-Allmaras and DES models, it is likely that the distance to the wall is not being calculated properly.

Figures 60 through 62 show the average pressure contour along the centerline of the bay ceiling for the coarse, medium, and fine grids, respectively. DES agrees well with the experimental data when solved on the medium grid, but predicts almost no change in pressure coefficient along the bay ceiling with the coarse grid. This shows that the DES model is more sensitive to mesh density than a regular RANS model. The DES model could not be run with the fine grid because of technical difficulties. Baldwin-Lomax performs increasingly well as the mesh density is increased. For the fine grid, Baldwin-Lomax data matches the experimental data well. For each of the coarse, medium, and fine grid simulations, Spalart-Allmaras predicts zero pressure coefficient along the centerline of the bay ceiling until the last two inches of the bay. Nichols(23) shows the Spalart-Allmaras model matching the pressure coefficient data nicely, making the case stronger that the Spalart-Allmaras model in Beggar may have been written incorrectly and is overdamping unsteady effects.

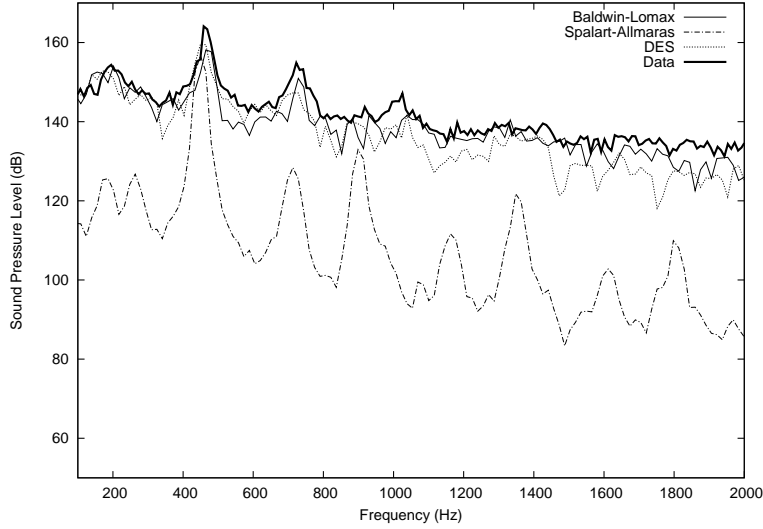


Figure 59: Sound Pressure Level Spectrum at the K16 Location - Medium Grid

Figures 63 through 65 show instantaneous vorticity plots on the centerplane of the bay grid. These plots give a better visual of the unsteady effects, or lack thereof in the Spalart-Allmaras case. Data from the K18 point and all other grids provided similar results and can be seen in Appendix B.1.

All runs for the medium case were performed on 3 nodes of a 2.2 GHz Opteron cluster with 2 processors per node and four gigabytes of memory per node. The wall clock times for each run were recorded. The average time per iteration for each turbulence model is shown in Table 12. The differences in time are not significant for this simulation. The additional time needed to solve the extra PDE in the Spalart-Allmaras model balanced the additional time needed to converge the Navier-Stokes equations with the Baldwin-Lomax model due to the extra unsteady effects present in the flow.

Table 12: Average computation times for various turbulence models for the tubulent cavity case

Model	Time per Iteration Normalized by Baldwin-Lomax
Baldwin-Lomax	1.0
Spalart-Allmaras	1.08
DES	0.99

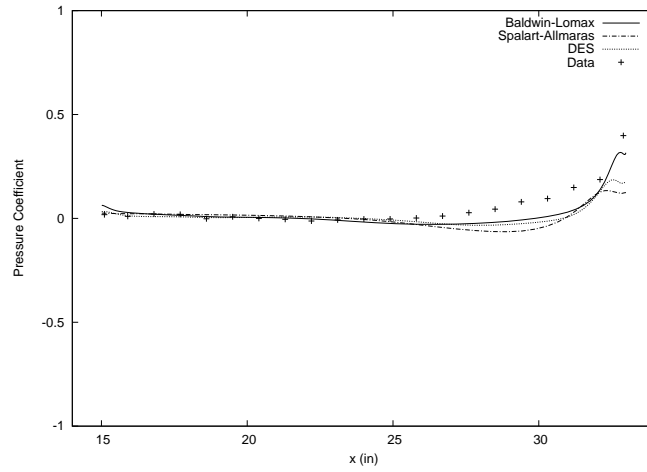


Figure 60: Average Pressure Coefficient on the Cavity Ceiling - Coarse Grid

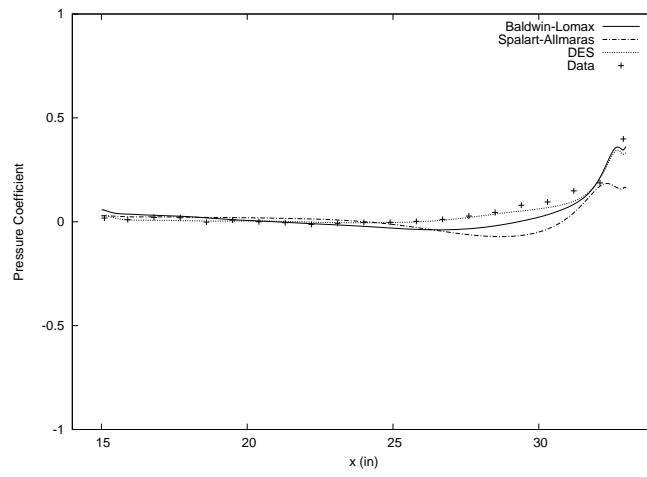


Figure 61: Average Pressure Coefficient on the Cavity Ceiling - Medium Grid

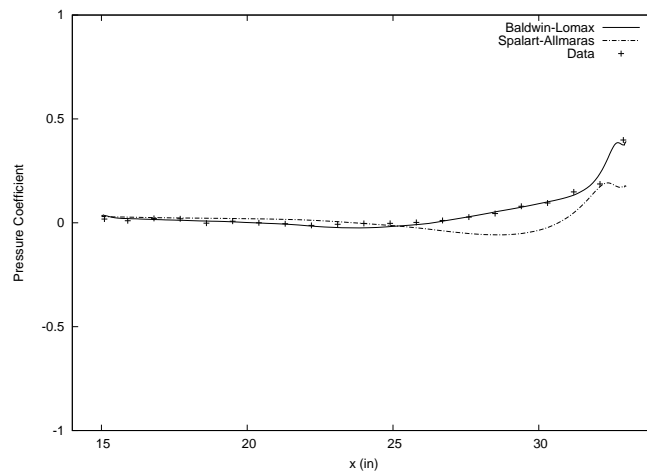


Figure 62: Average Pressure Coefficient on the Cavity Ceiling - Fine Grid

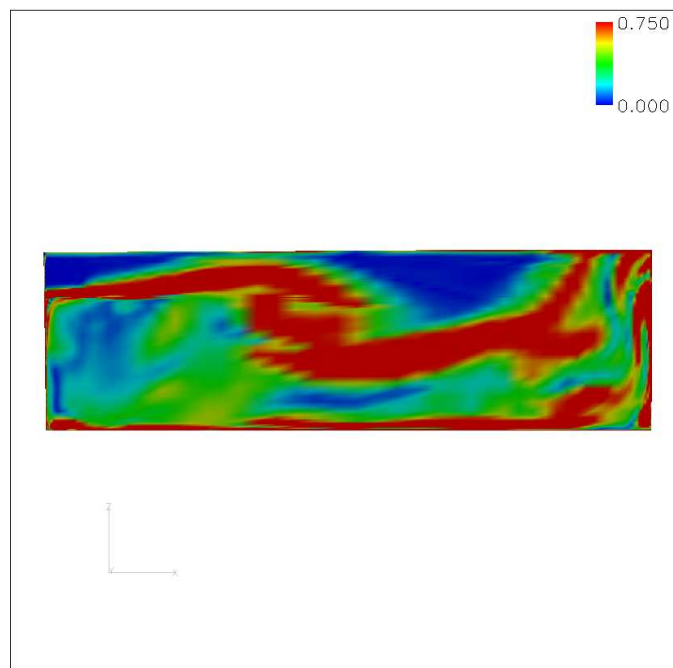


Figure 63: Vorticity - Baldwin-Lomax - Medium Cavity Grid

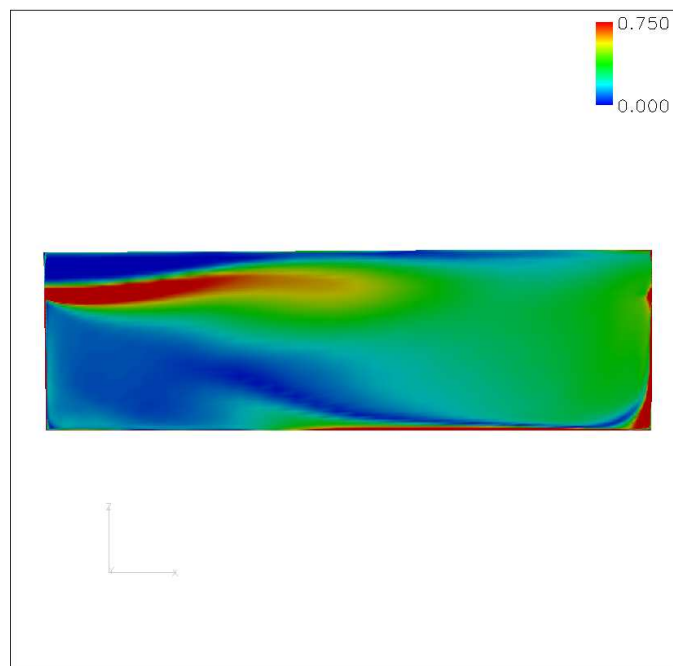


Figure 64: Vorticity - Spalart-Allmaras - Medium Cavity Grid

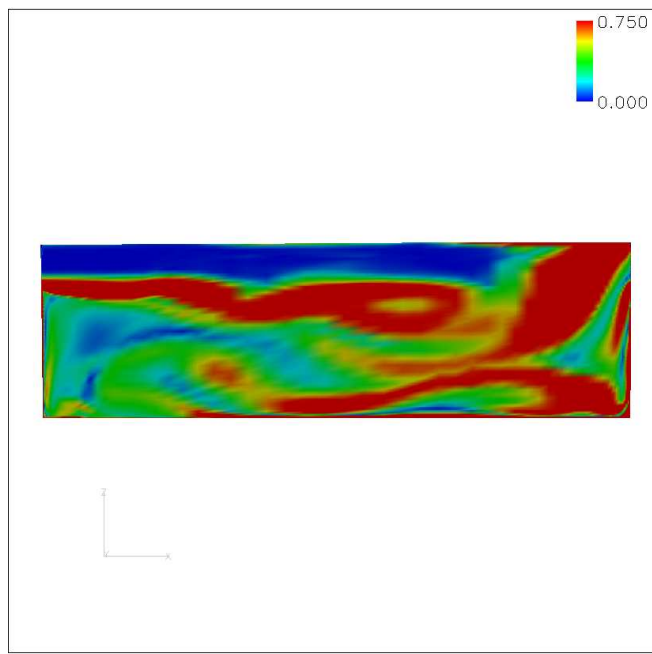


Figure 65: Vorticity - DES - Medium Cavity Grid

4.4 *Conclusions*

Considering all three cases in the turbulent study, it is determined that the version of the Spalart-Allmaras model in the Beggar code used in this study should not be used to simulate unsteady turbulent flow. In every case, the Spalart-Allmaras model damped out all the unsteady effects in the flow. Since the DES model in the Beggar code used Spalart-Allmaras as its subgrid model, there is concern that DES may damp out the steady effects as well. This appears to have been the case for the oscillating airfoil at $\alpha_o = 11.0^\circ$. The grid may not have been resolved fine enough in that case though, as unsteady effects were not damped out by the DES model in the turbulent cavity simulation with the medium grid. Strong evidence was presented that the Spalart-Allmaras model in Beggar may have been written incorrectly.

No conclusions can be made about which turbulence model uses the least cpu-time. The largest effect that the turbulence model had on average cpu-time was determining if there should be vortices or not. The largest piece of cpu-time is dedicated to converging the inner iterations, and unsteady phenomena such as vortices increase the difficulty of converging these inner iterations.

V. GENERIC STORE SIMULATION

5.1 Case Presentation

Chapters III and IV provide much insight into the Beggar code and how the turbulence models compare with experimental and theoretical data, but the cases themselves are not representative of the simulations performed day to day by the CAT. To see how the models react to a more applicable simulation, a MK-84 store jettison was simulated.

The MK-84 is initially in an X-configuration at $\alpha_o = -10.0^\circ$, as shown in Figure 66. The MK-84 block is broken into eight equal circumferentially divided grids of dimension 138x26x52. The store is 160 inches long with a maximum width of 24.5 inches. The initial spacing off the store surface is 3×10^{-5} inches. The store block resides inside an overlap grid of dimensions 70x51x45 (750x600x600 inches) which is fixed to the store. The store block and overlap block are both released in the center of a stationary cartesian grid of dimensions 44x43x43 (2200x2000x2000 inches).

Initial conditions are shown in Table 13. To achieve time accurate results, three Newton dt-iterations were run every time step. Each Newton dt-iteration will solve 80 symmetric Gauss-Seidel inner iterations unless an inner convergence tolerance of $1 \cdot 10^{-8}$ is met.

Table 13: Store jettison initial conditions

Property	Value
M	0.95
Re	$4.9 \cdot 10^5 \frac{1}{ft}$
c_∞	$1097.6 \frac{ft}{s}$
Solver options: Steger-Warming Jacobians 2nd Order Spatial Differencing Roe Right Hand Side 3 dt-iterations	

The store jettison was simulated with the Baldwin-Lomax, Spalart-Allmaras, and DES models. Recording the change in orientation angle of the store, the effect the turbulence model has on the store can be recorded. Turbulent effects will be greatest when the store has little inertia. For this reason, the simulation was initialized with no inertia in the y-direction. A small initial time step of $\Delta t = 7.6 \times 10^{-7}$ seconds was used to allow the turbulence model

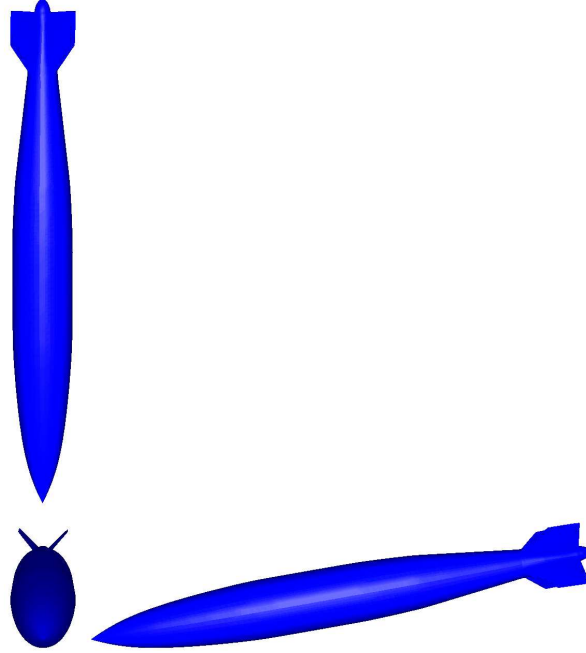


Figure 66: Initial Store Orientation

to properly influence the store trajectory before the inertia starts to dominate. The time step used with respect to iteration is shown in Table 14. After 14,000 iterations, the Spalart-Allmaras and DES models predicted negative densities so the simulation was stopped there. It should be noted that Baldwin-Lomax would have continued.

Table 14: Store jettison time step per iteration

Iteration Range	Time Step (sec)
1-10000	7.6×10^{-7}
10001-11000	7.6×10^{-6}
11001-13000	7.6×10^{-5}
13001-14000	1.14×10^{-4}

5.2 Results

Figures 67 to 69 show the time history of roll, pitch, and yaw respectively. All of the models are in good agreement for pitch and yaw. Divergence is present in the roll time history plot. Baldwin-Lomax predicts negative roll angles while Spalart-Allmaras and DES predict positive values. The separation between Spalart-Allmaras and DES roll predictions

also appears to be diverging. This is probably due to the turbulence models effect on the fins.

Figures 70, 71, and 72 show total pressure on and around the store body. All three figures show the same distribution across the store body. Figure 73 shows pressure coefficients along the store for the three models. All three models predict the same pressure coefficient distribution except for minor differences near the fins, showing that the turbulence model will not have much effect on the motion of the store.

Figure 74 shows the pressure coefficient along the mid-span of one of the upper fins. The C_p on the upper surface of the fin is the same for all three models. DES predicts about a 20% increase in C_p on the lower surface near the quarter chord. This difference will not create a moment large enough to have a substantial influence on a 2000 pound bomb, but the fact that the difference exists should be noted.

All runs for the store jettison simulation were performed on 5 nodes of an Opteron cluster with 2 processors per node and four gigabytes of memory per node. The wall clock times for each run were recorded. The average time per iteration for each turbulence model is shown in Table 15, which shows the DES model taking about $\frac{3}{4}$ the time of Spalart-Allmaras model. This time difference can be attributed to the turbulent PDE converging fast and using less Gauss-Seidel inner iterations in the DES case. Baldwin-Lomax took about 1.6 times longer to solve each time step than DES.

Table 15: Wall clock times for various turbulence models for the store jettison case

Model	Time per Iteration Normalized by Baldwin-Lomax
Baldwin-Lomax	1.0
Spalart-Allmaras	0.81
DES	0.61

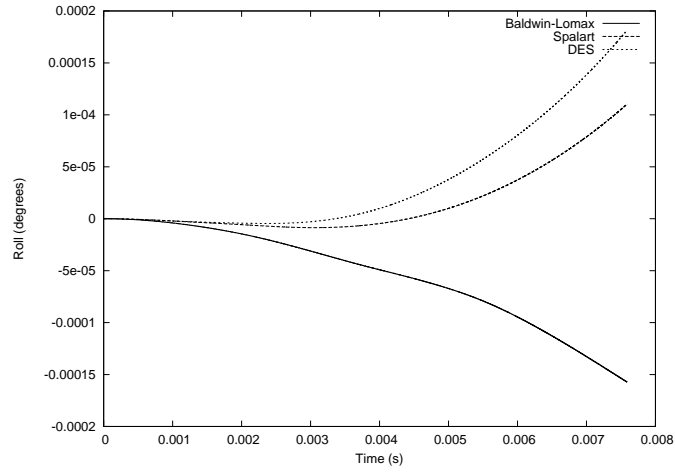


Figure 67: Roll Time History

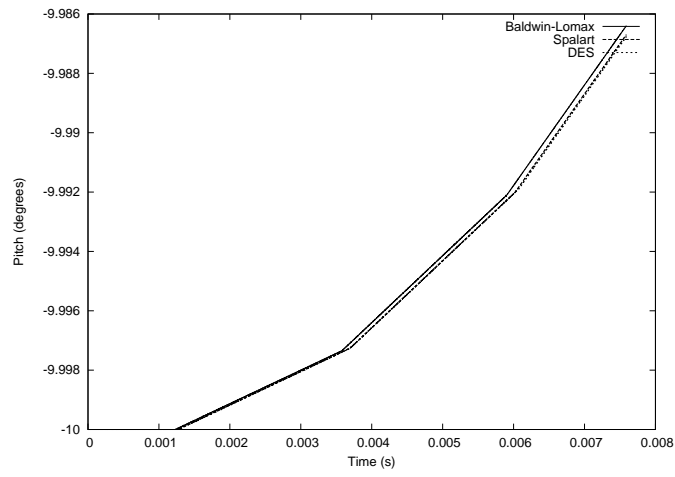


Figure 68: Pitch Time History

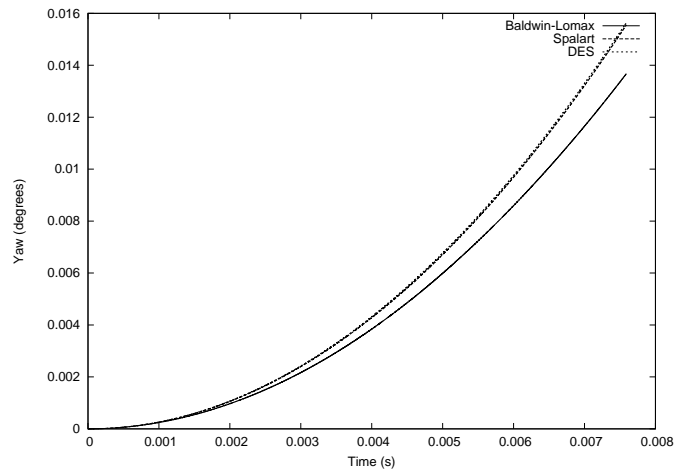


Figure 69: Yaw Time History

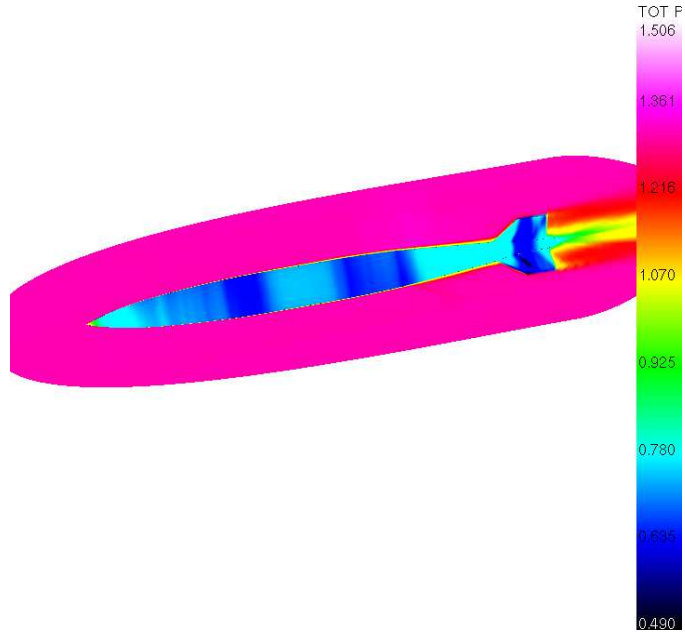


Figure 70: Pressure at $t = 7.62 \times 10^{-3}$ sec - Baldwin-Lomax

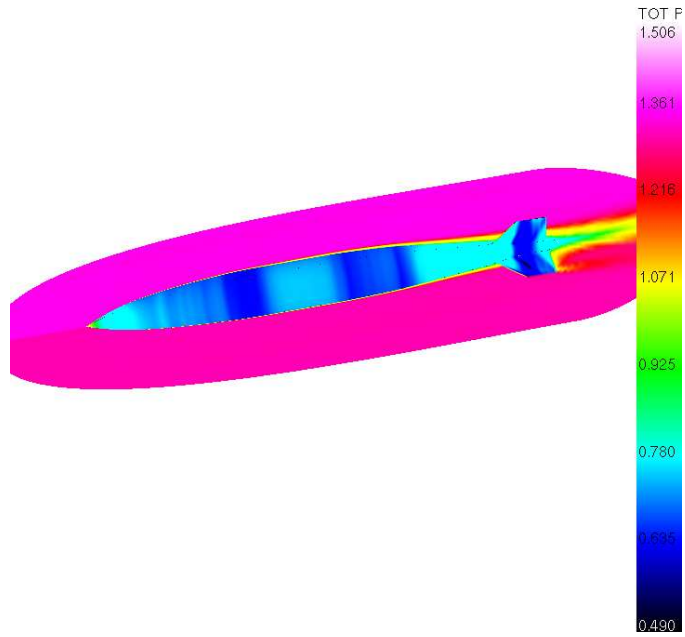


Figure 71: Pressure at $t = 7.62 \times 10^{-3}$ sec - Spalart-Allmaras

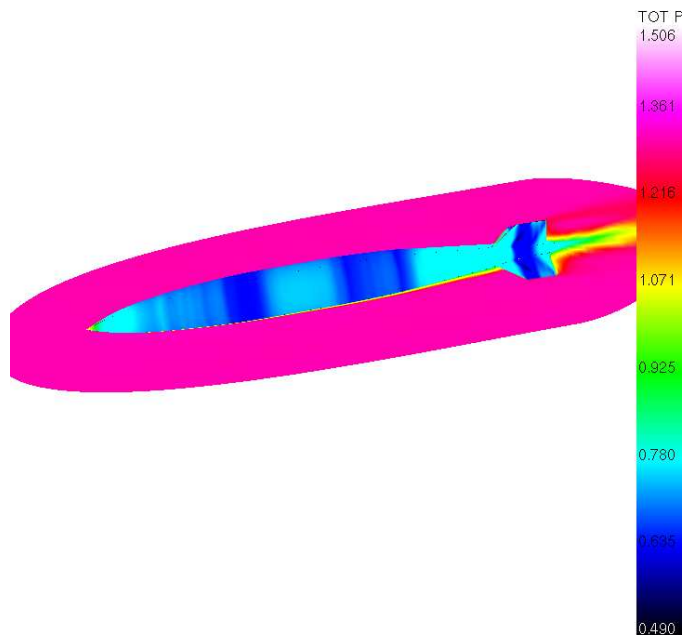


Figure 72: Pressure at $t = 7.62 \times 10^{-3}$ sec - DES

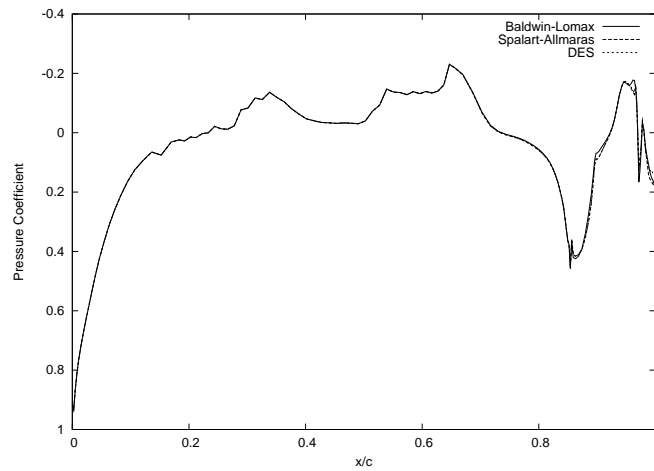


Figure 73: Pressure Coefficient Along Store Body

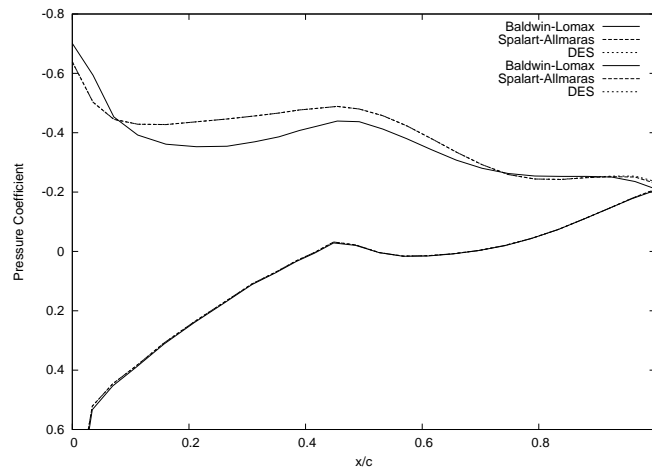


Figure 74: Pressure Coefficient Along Midspan of Store Fin

VI. SUMMARY AND RECOMMENDATIONS

6.1 *Summary*

Reviewing Chapter III, conclusions were drawn about which solver options should be used while attempting to model unsteady turbulent flow. To properly simulate unsteady turbulent flow, it is important to reduce artificial dissipation and accurately calculate each time step. The inviscid convecting vortex provided much useful data about how each solver option contributed to artificial dissipation, while the shock-tube and 2D cylinder were most beneficial in the area of time step convergence. Reviewing the non-turbulent cases, the conclusions are drawn that the following solver options should be implemented in the Beggar code to simulate unsteady turbulent flow:

1. A second order temporal discretization
2. Between three and five Newton dt-iterations

Considering all three cases in the turbulent study in Chapter IV, it is determined that the Spalart-Allmaras model as currently implemented should not be used to simulate unsteady turbulent flow. In every case, the Spalart-Allmaras model damped out most of the unsteady effects in the flow. Since the DES model in the Beggar code used Spalart-Allmaras as its subgrid model, there is concern that DES may damp out the unsteady effects as well. This appears to have been the case for the oscillating airfoil at $\alpha_o = 11.0^\circ$. However, the grid may not have been resolved fine enough, as unsteady effects were not damped out by the DES model in the turbulent cavity simulation with the medium grid. Unfortunately, time and computational constraints prevented further study of the DES model on grids fine enough where DES performs best. Therefore a conclusion on whether the DES model should be used to model unsteady turbulent flow cannot be made.

A strong case has been made that the Spalart-Allmaras model may not have been written correctly into Beggar. (17:Murman) notes that the Spalart-Allmaras model produces excessively large values of turbulent eddy-viscosity in the region of off-surface vortices. This property of the model may be washing away the unsteady effects, but the fact that the Beggar version of Spalart-Allmaras seems to be damping unsteady effects more than other codes leads to the conclusion that the Beggar version of Spalart-Allmaras needs to be evaluated. Recalling that the only difference between the Spalart-Allmaras and DES

models is the distance to the wall variable and because DES provided much better results with the turbulent cavity case, the distance to the wall is a likely suspect as to what is being improperly calculated.

Finally considering the store jettison simulation in Chapter V, the conclusion is drawn that the choice of turbulence model does not play a large part in the trajectory of a massive object traveling at high velocities. The fact that the Baldwin-Lomax model took 1.6 times longer to solve the problem may be a good reason to cease using it, especially in steady problems where Spalart-Allmaras will have the added bonus of damping unsteady effects in the flow.

6.2 Recommendations

This study compared different turbulence models using the same grids. While this provided information about how a turbulence model generally performs, grid optimization would provide additional information on solution clock times and accuracy. Each model would be optimized with differently dimensioned grids. Therefore, a good study to run would be to optimize the grids for the models being compared and then compare clock times and solutions to determine which model best suits the user's needs.

The instabilities that second order Roe combined with the three point backward time temporal discretization showed in the inviscid vortex case should be investigated.

Appendix A. Results from Non-Turbulent Cases

A.1 Inviscid Convecting Vortex

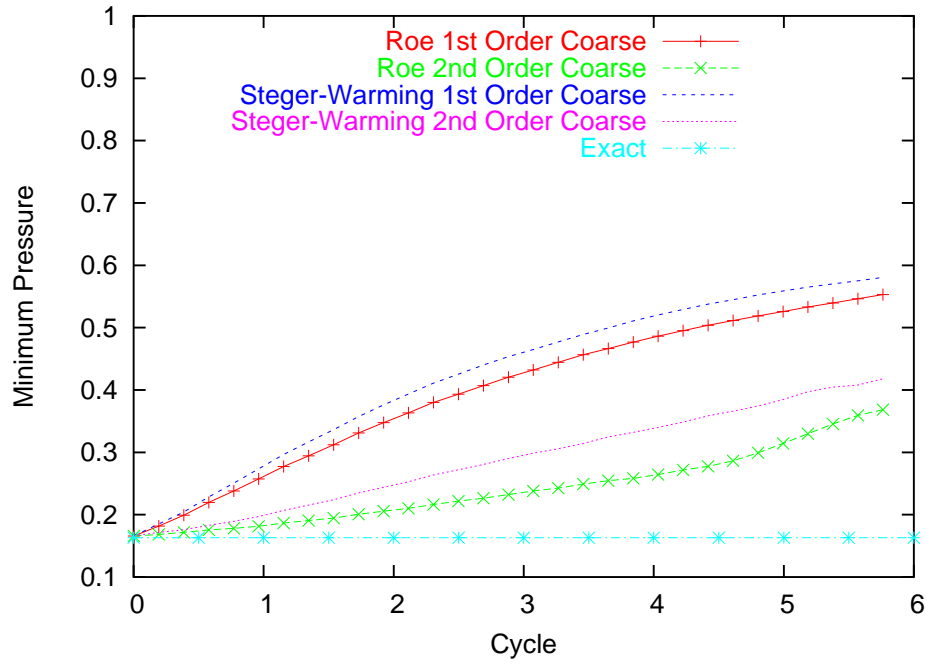


Figure 75: Cycle vs Minimum Pressure - Coarse Grid

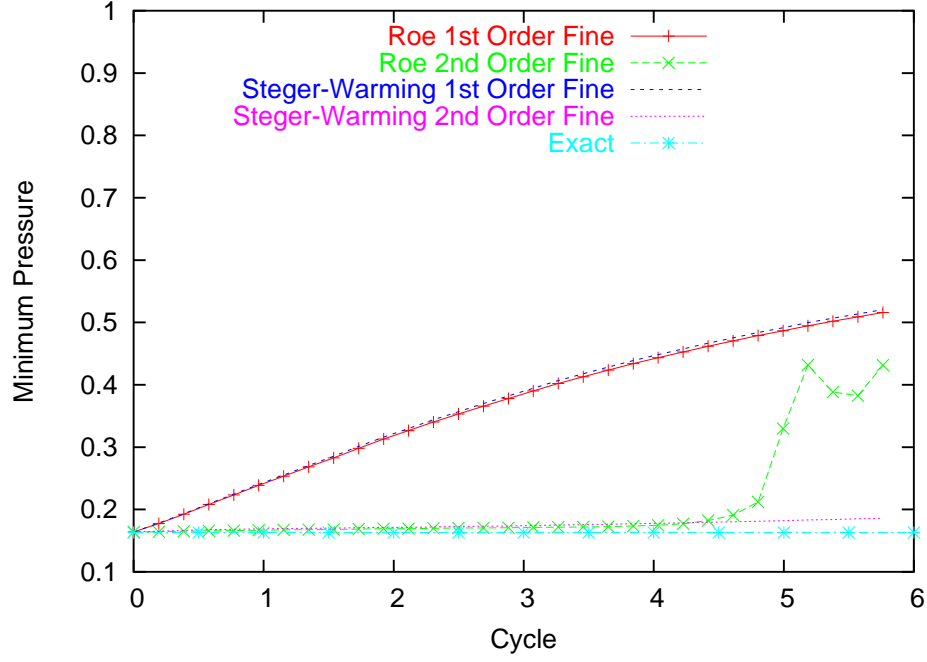


Figure 76: Cycle vs Minimum Pressure - Fine Grid

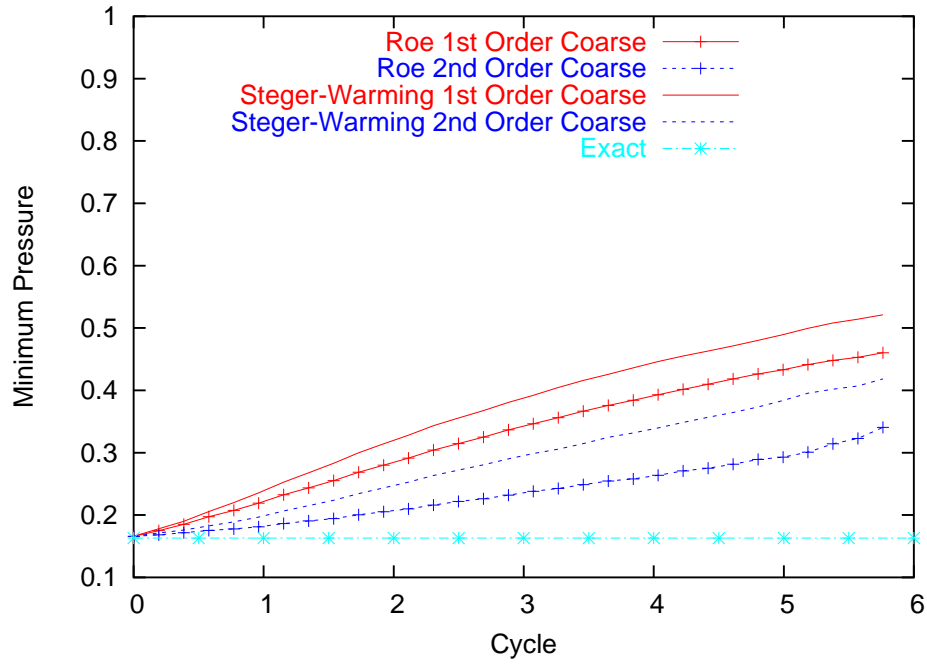


Figure 77: Cycle vs Minimum Pressure - Coarse Grid - Halved Time Step

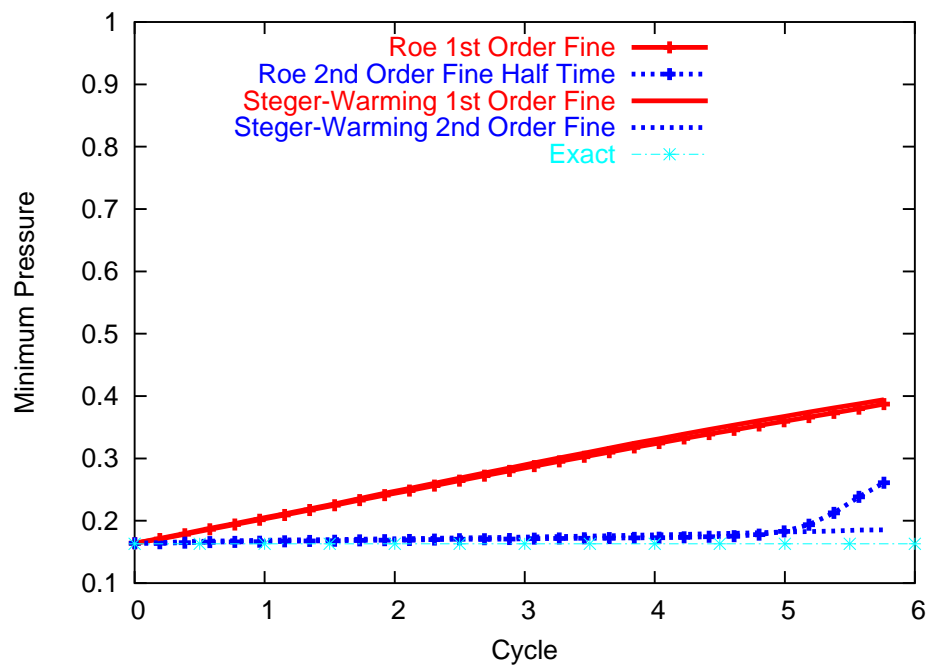


Figure 78: Cycle vs Minimum Pressure - Fine Grid - Halved Time Step

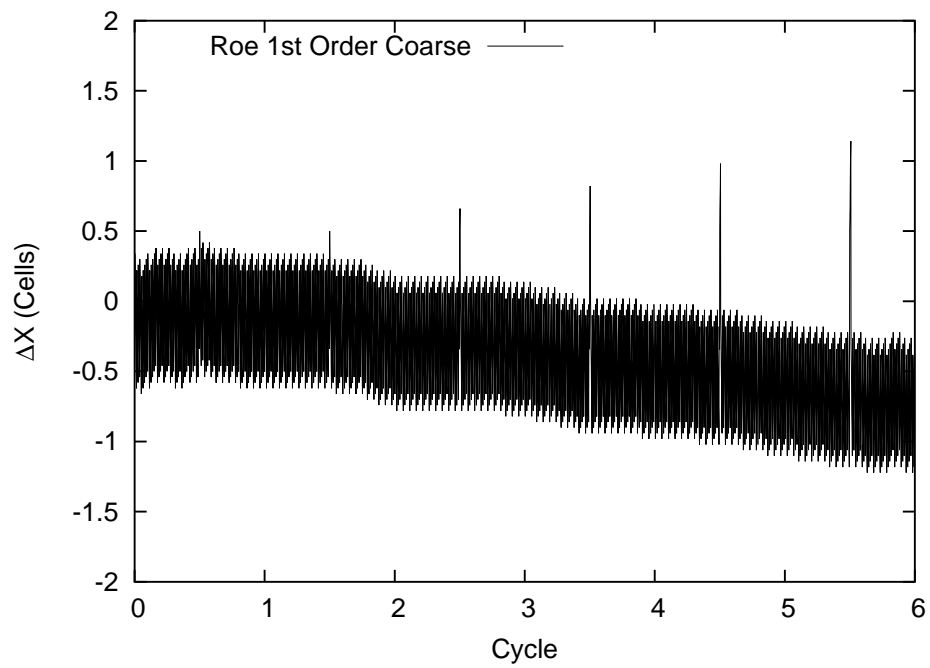


Figure 79: Cycle vs Δx - Roe - Coarse Grid - 1st Order Temporal

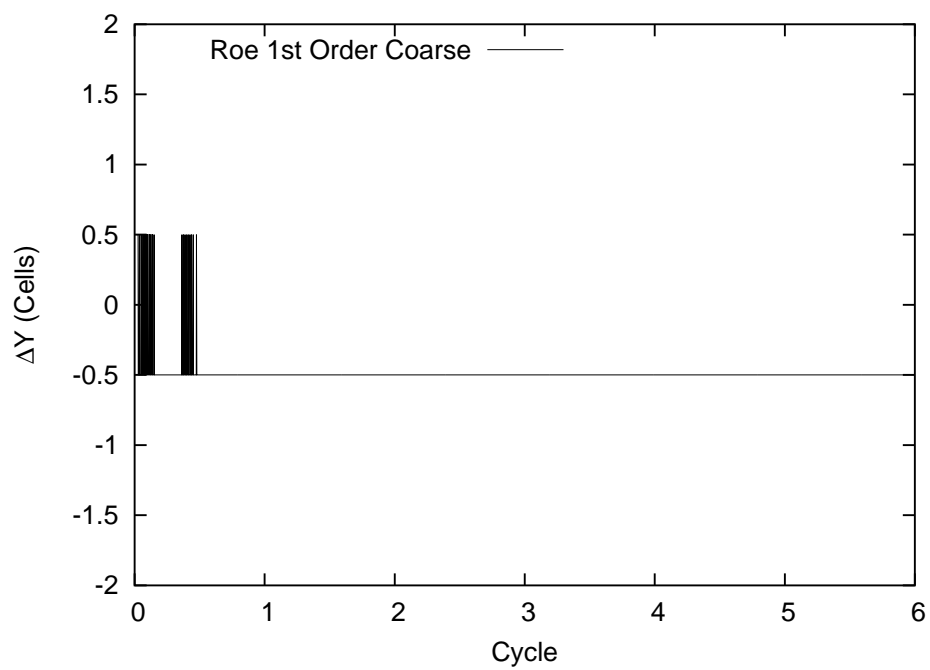


Figure 80: Cycle vs Δy - Roe - Coarse Grid - 1st Order Temporal

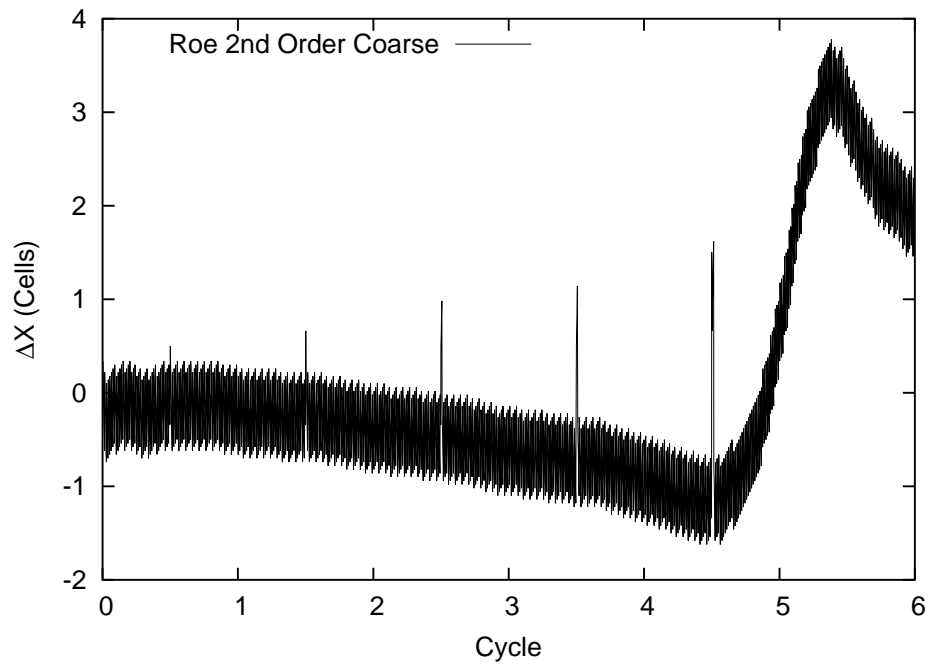


Figure 81: Cycle vs Δx - Roe - Coarse Grid - 2nd Order Temporal

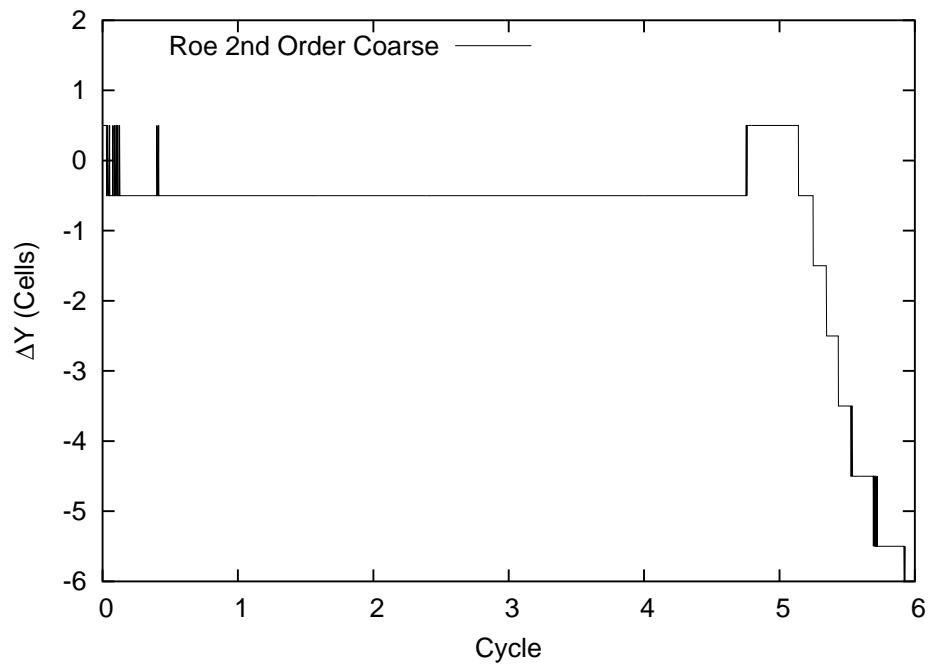


Figure 82: Cycle vs Δy - Roe - Coarse Grid - 2nd Order Temporal

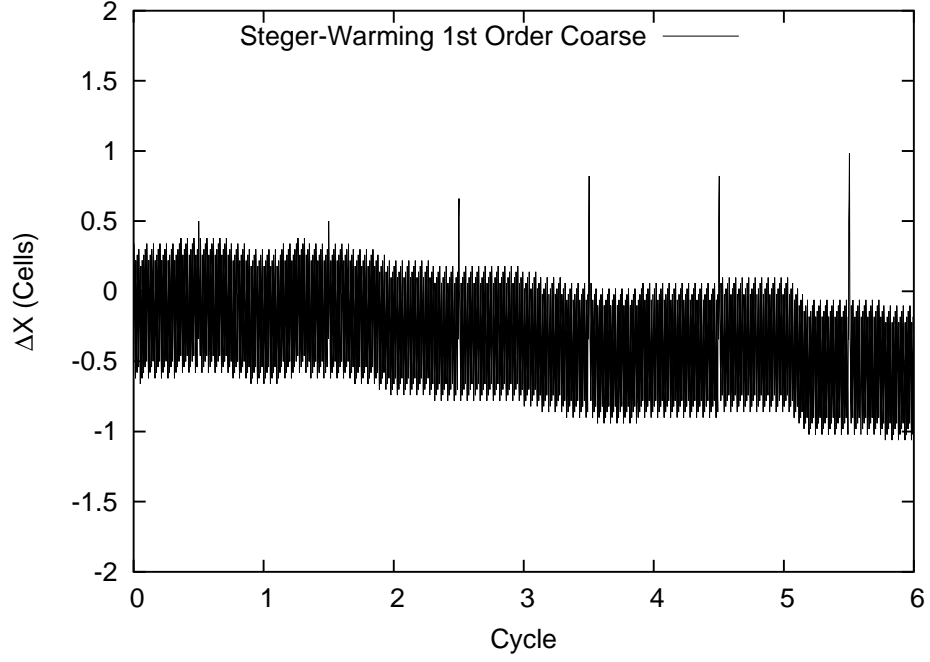


Figure 83: Cycle vs Δx - Steger-Warming - Coarse Grid - 1st Order Temporal

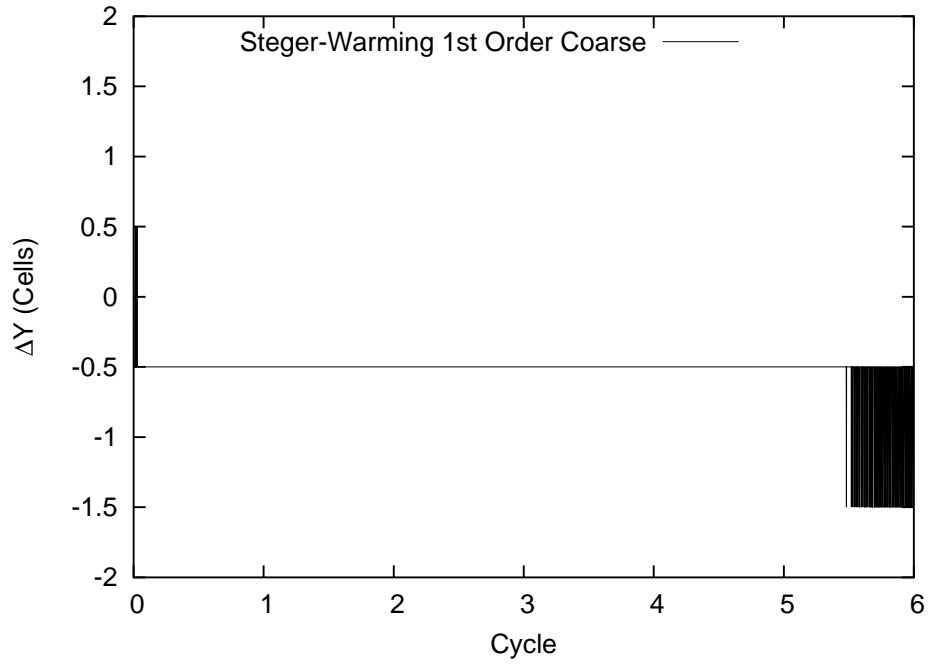


Figure 84: Cycle vs Δy - Steger-Warming - Coarse Grid - 1st Order Temporal

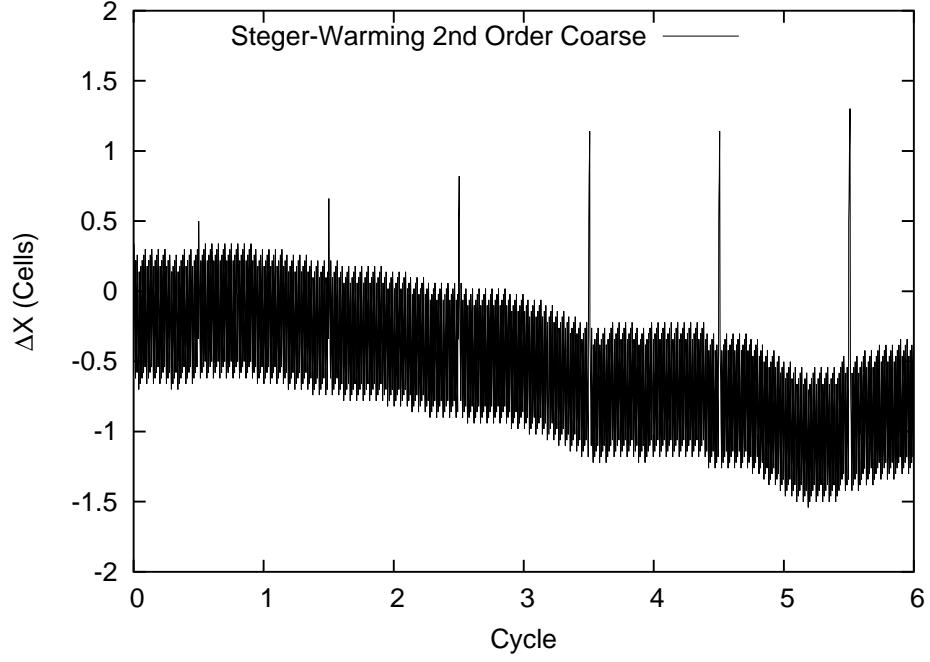


Figure 85: Cycle vs Δx - Steger-Warming - Coarse Grid - 2nd Order Temporal

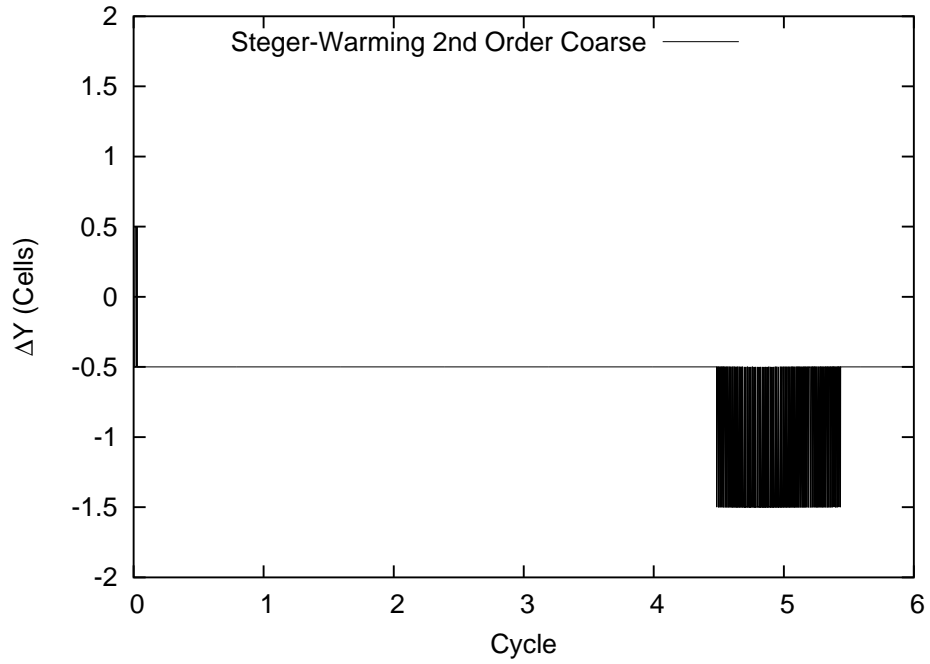


Figure 86: Cycle vs Δy - Steger-Warming - Coarse Grid - 2nd Order Temporal

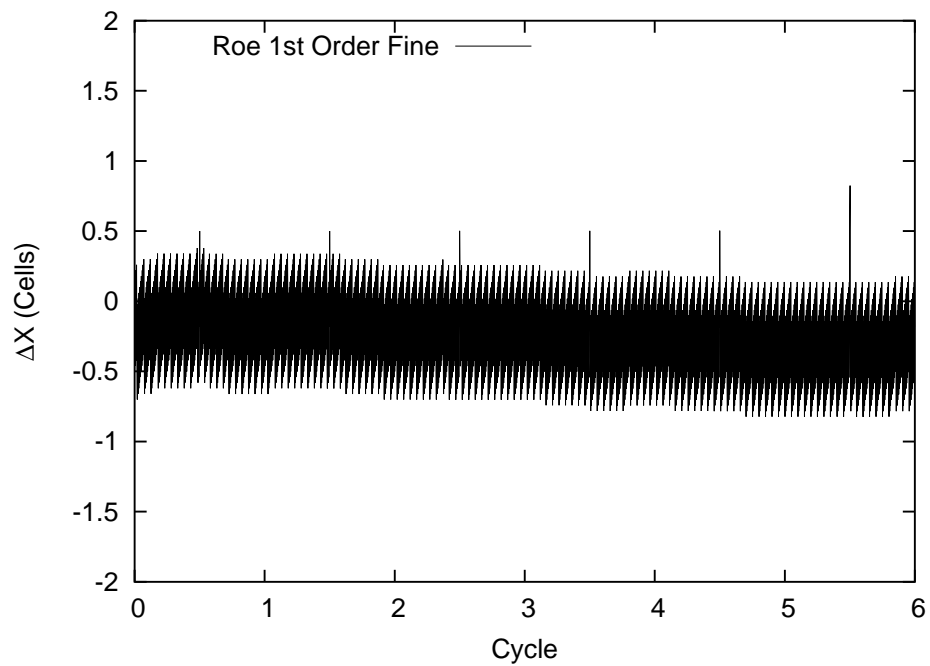


Figure 87: Cycle vs Δx - Roe - Fine Grid - 1st Order Temporal

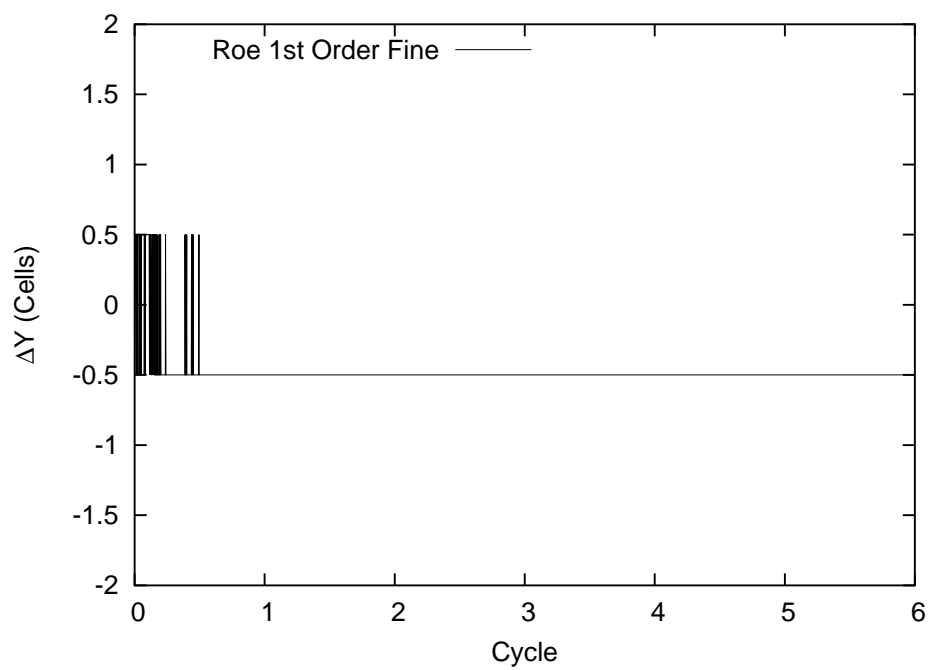


Figure 88: Cycle vs Δy - Roe - Fine Grid - 1st Order Temporal

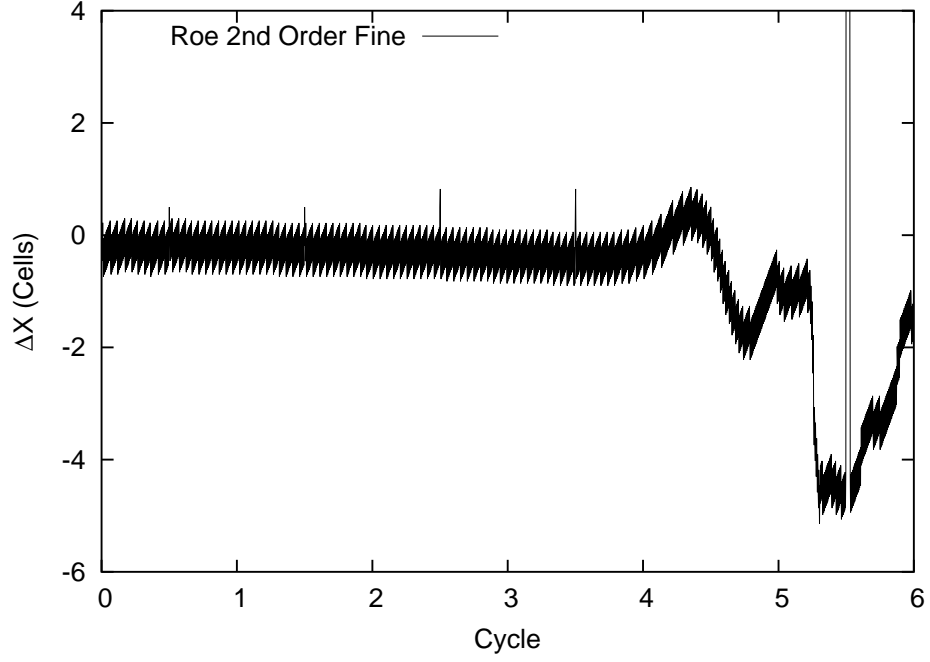


Figure 89: Cycle vs Δx - Roe - Fine Grid - 2nd Order Temporal

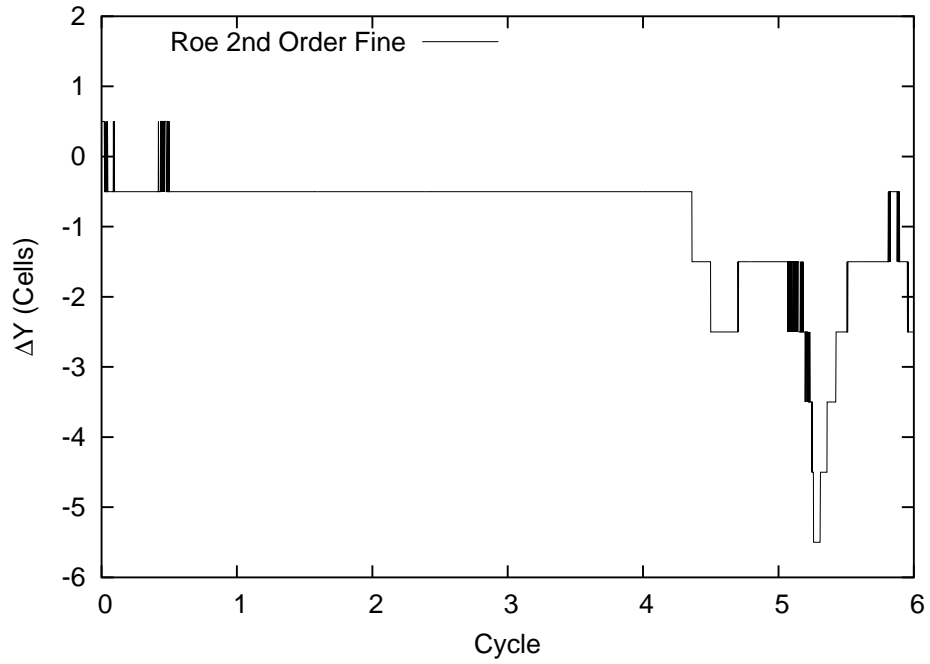


Figure 90: Cycle vs Δy - Roe - Fine Grid - 2nd Order Temporal

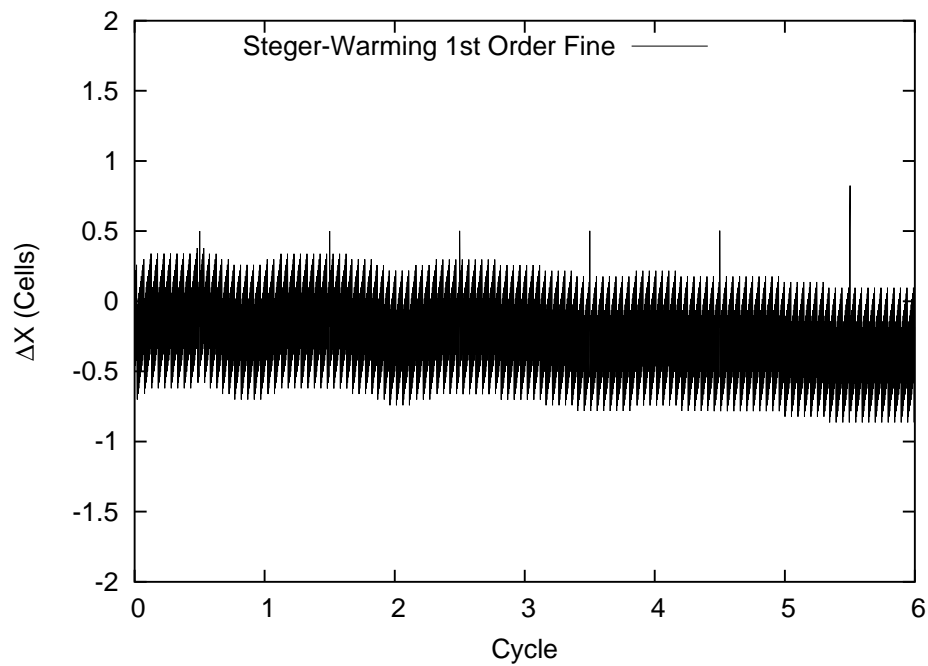


Figure 91: Cycle vs Δx - Steger-Warming - Fine Grid - 1st Order Temporal

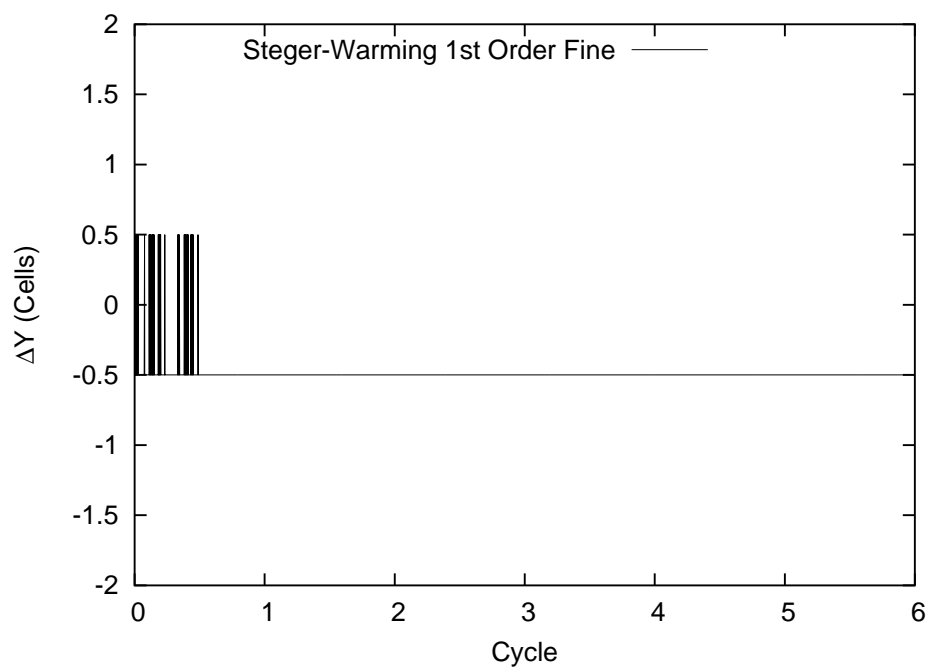


Figure 92: Cycle vs Δy - Steger-Warming - Fine - 1st Order Temporal

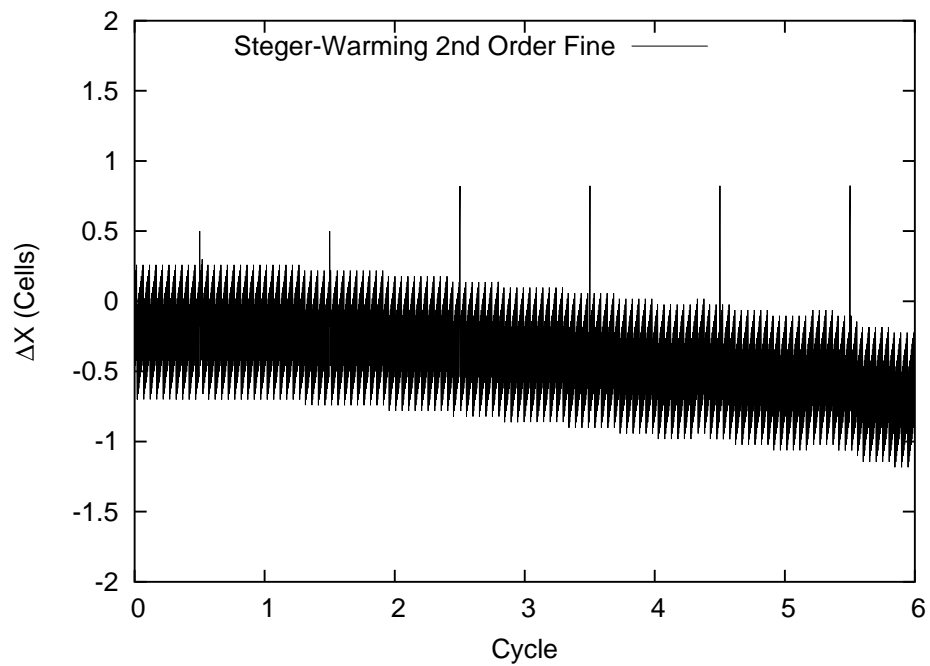


Figure 93: Cycle vs Δx - Steger-Warming - Fine - 2nd Order Temporal

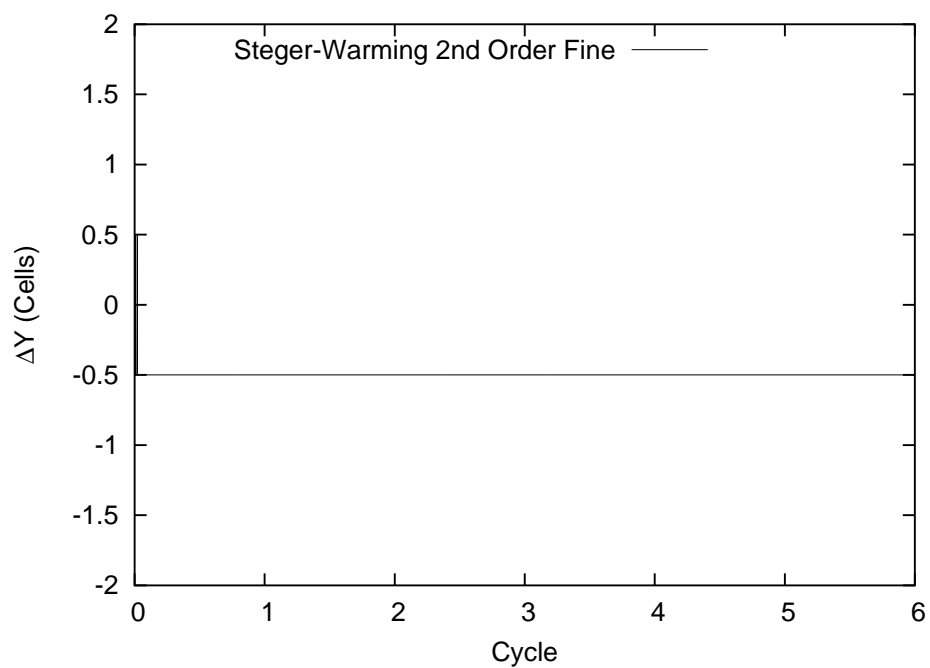


Figure 94: Cycle vs Δy - Steger-Warming - Fine Grid - 2nd Order Temporal

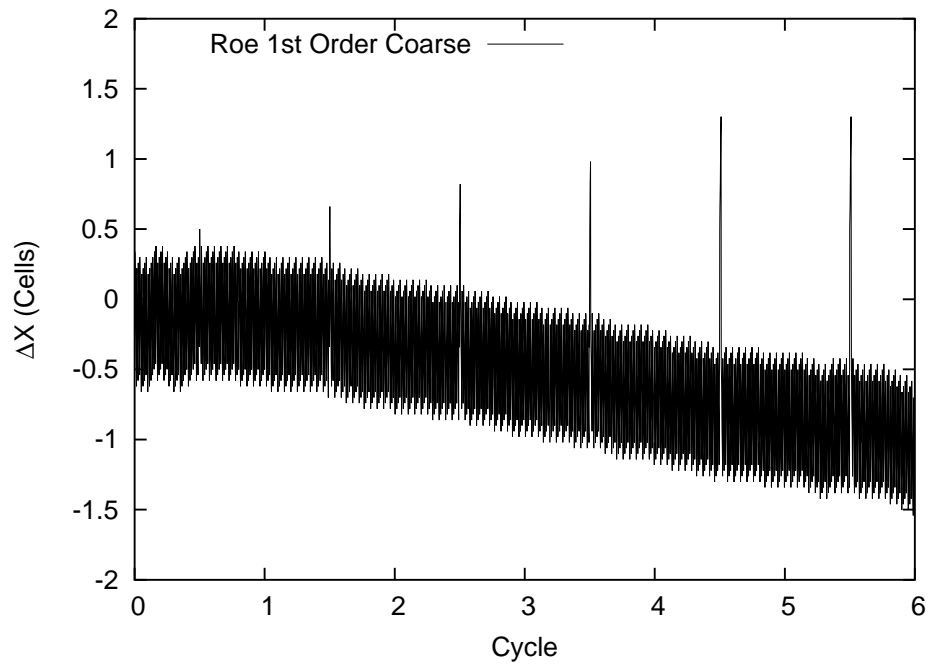


Figure 95: Cycle vs Δx - Roe - Coarse Grid - 1st Order Temporal - Halved Time Step

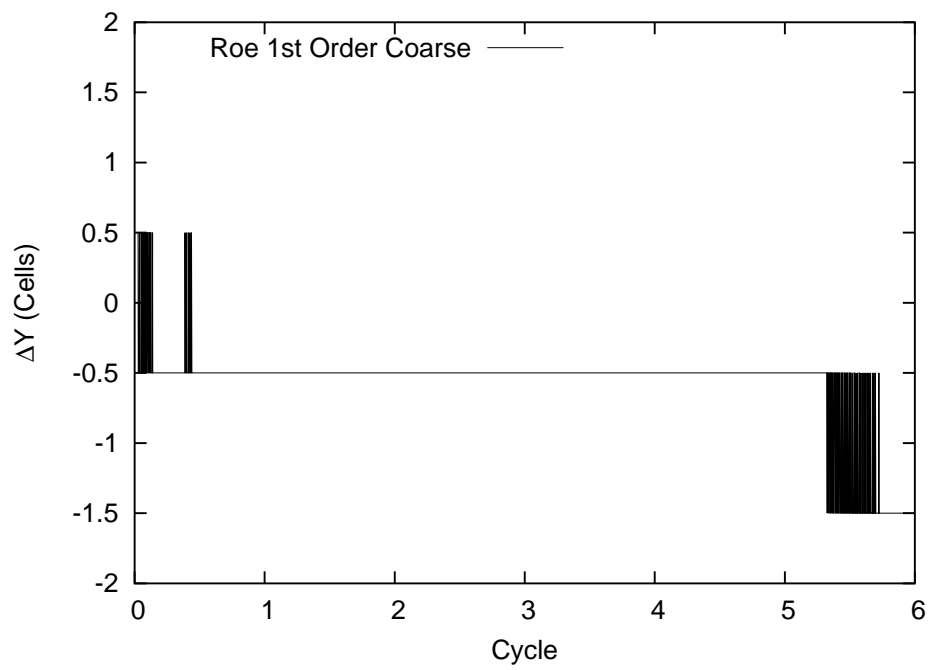


Figure 96: Cycle vs Δy - Roe - Coarse Grid - 1st Order Temporal - Halved Time Step

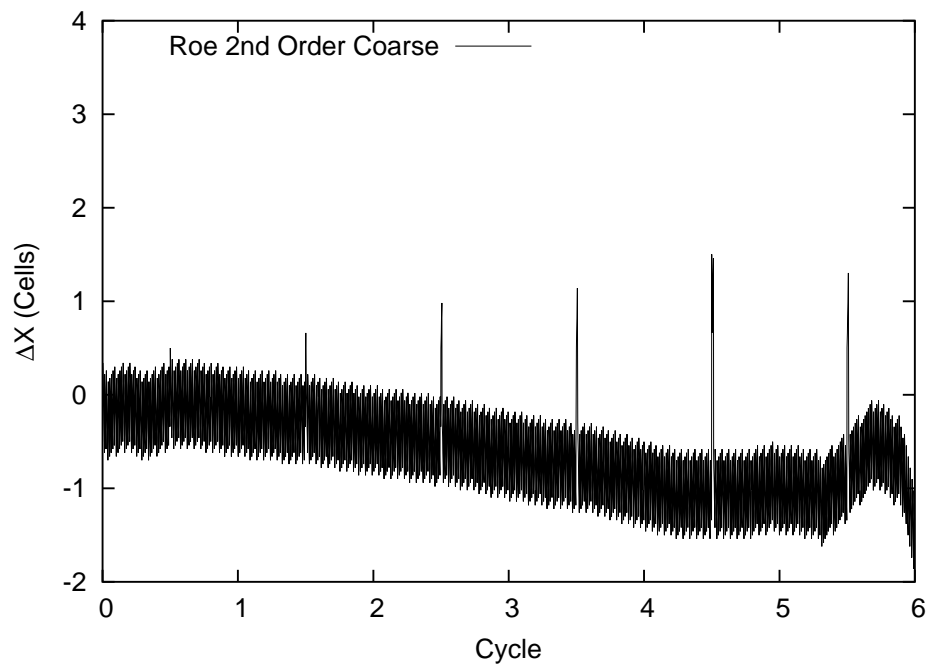


Figure 97: Cycle vs Δx - Roe - Coarse Grid - 2nd Order Temporal - Halved Time Step

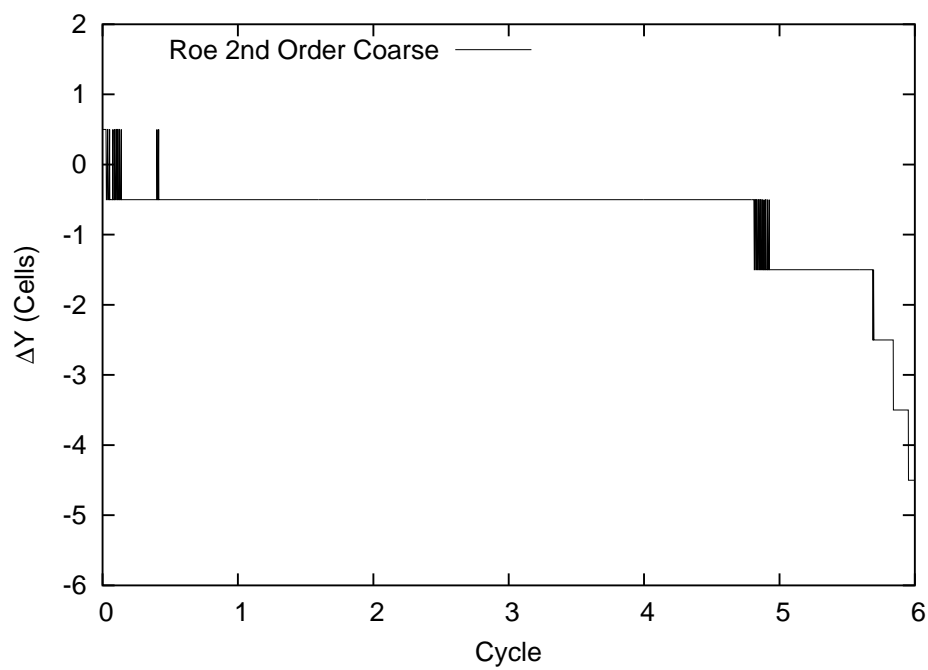


Figure 98: Cycle vs Δy - Roe - Coarse Grid - 2nd Order Temporal - Halved Time Step

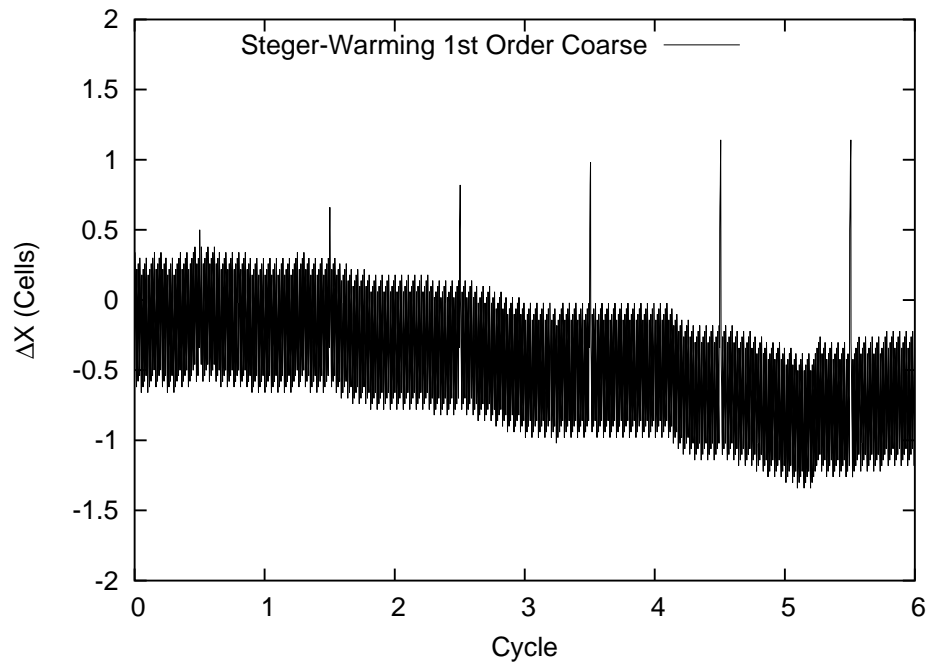


Figure 99: Cycle vs Δx - Steger-Warming - Coarse Grid 1st Order Temporal - Halved Time Step

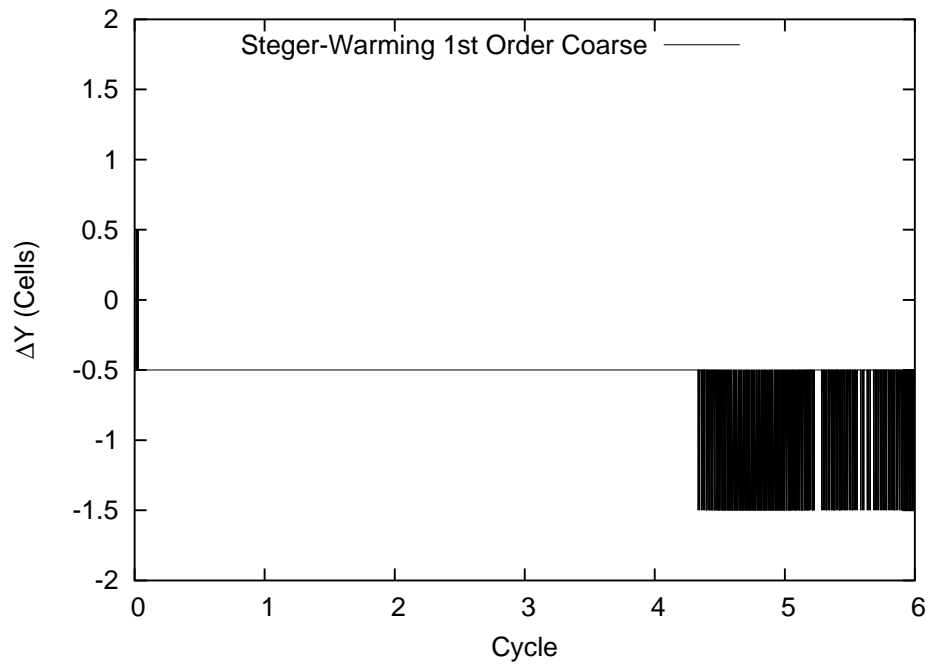


Figure 100: Cycle vs Δy - Steger-Warming - Coarse Grid - 1st Order Temporal - Halved Time Step

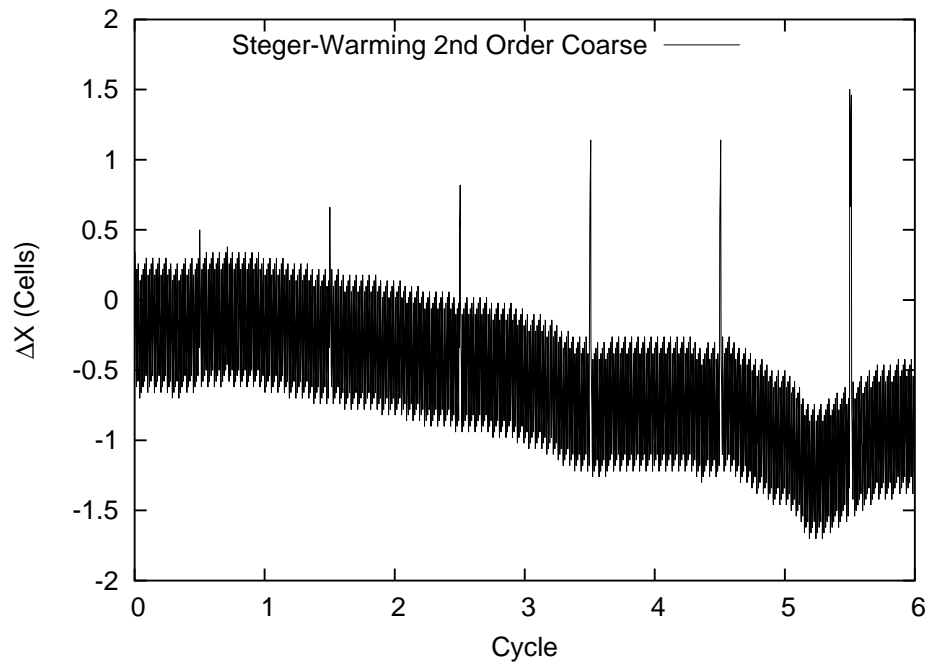


Figure 101: Cycle vs Δx - Steger-Warming - Coarse Grid - 2nd Order Temporal - Halved Time Step

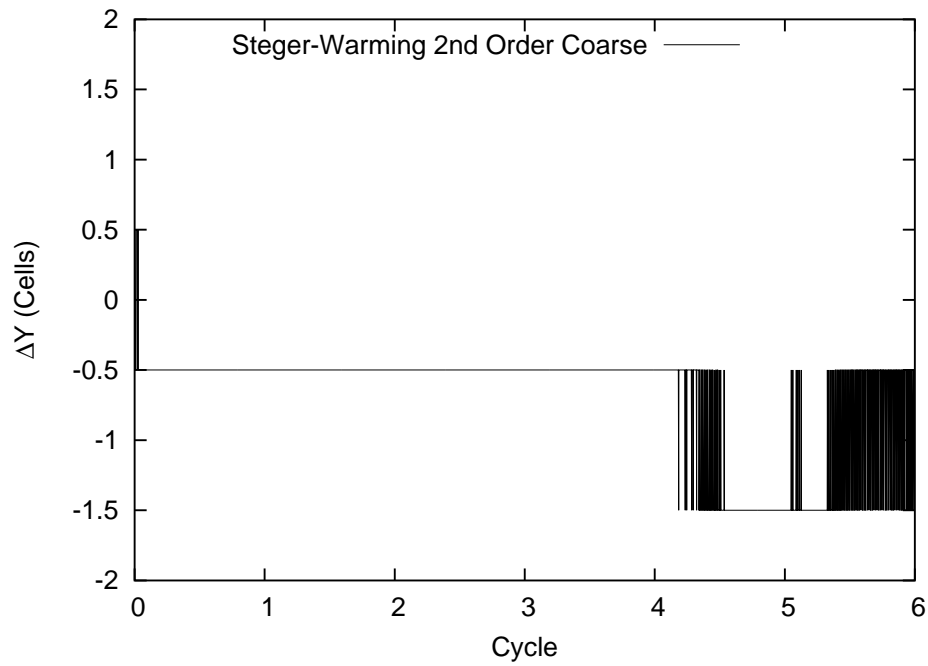


Figure 102: Cycle vs Δy - Steger-Warming - Coarse Grid - 2nd Order Temporal - Halved Time Step

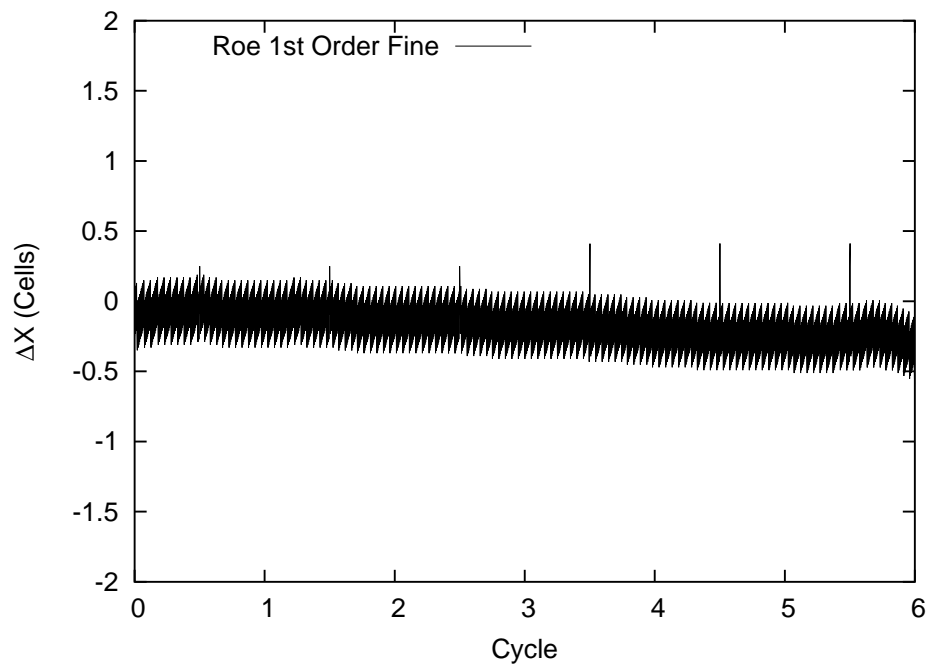


Figure 103: Cycle vs Δx - Roe - Fine Grid - 1st Order Temporal - Halved Time Step

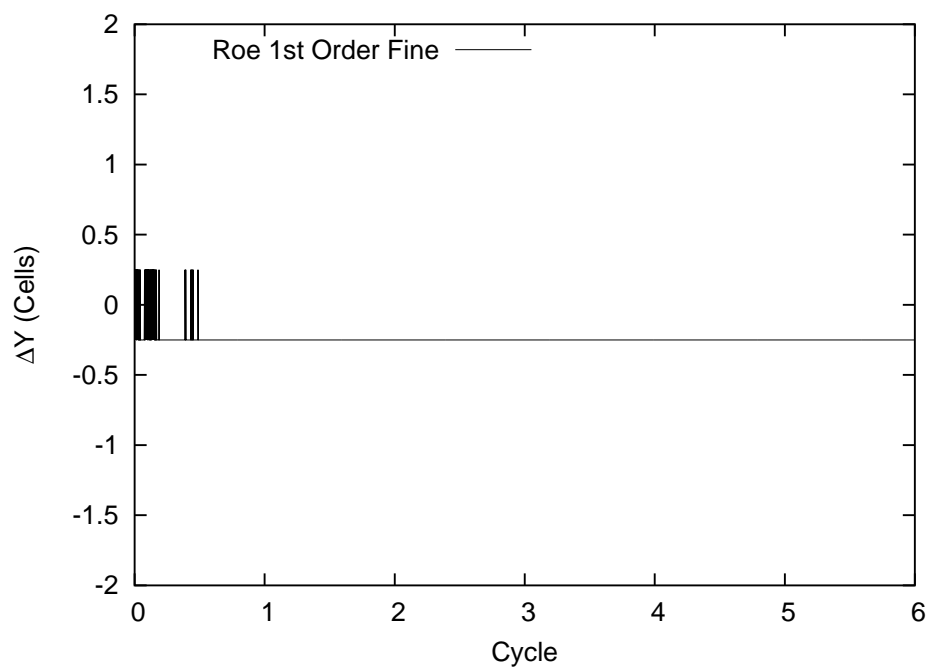


Figure 104: Cycle vs Δy - Roe - Fine Grid - 1st Order Temporal - Halved Time Step

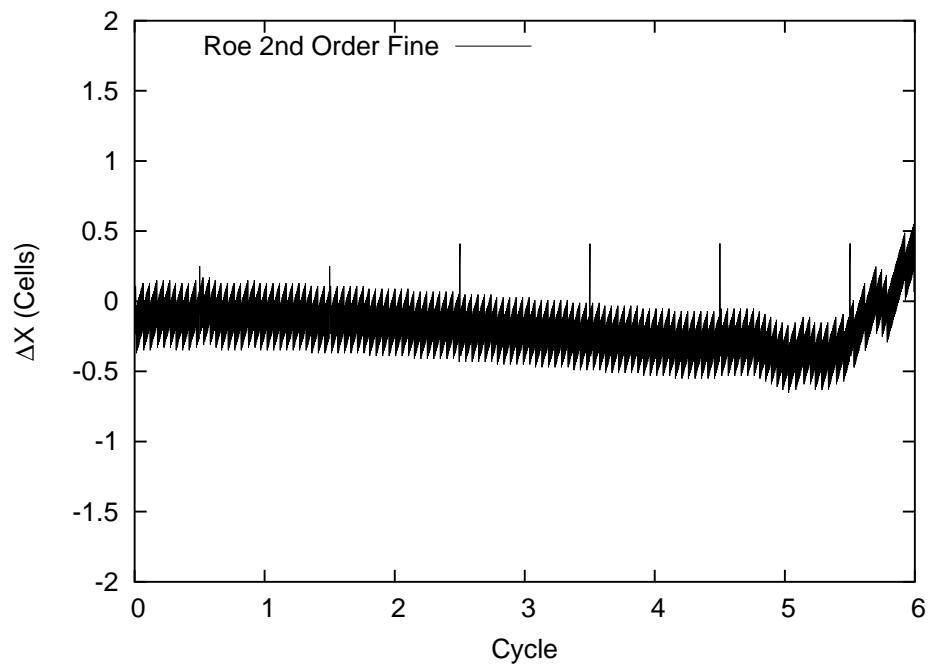


Figure 105: Cycle vs Δx - Roe - Fine Grid - 2nd Order Temporal - Halved Time Step

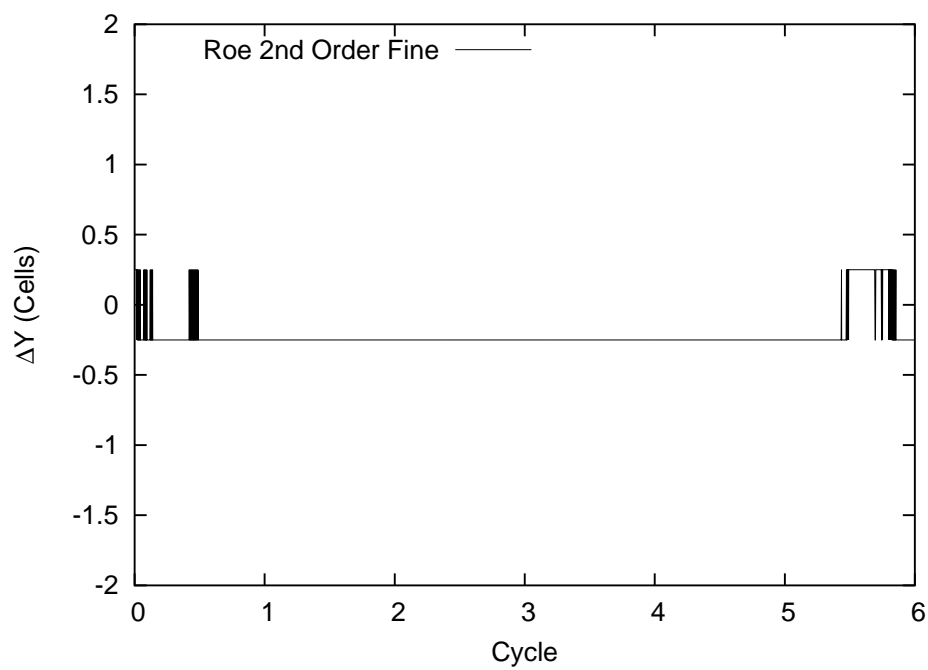


Figure 106: Cycle vs Δy - Roe - Fine Grid - 2nd Order Temporal - Halved Time Step

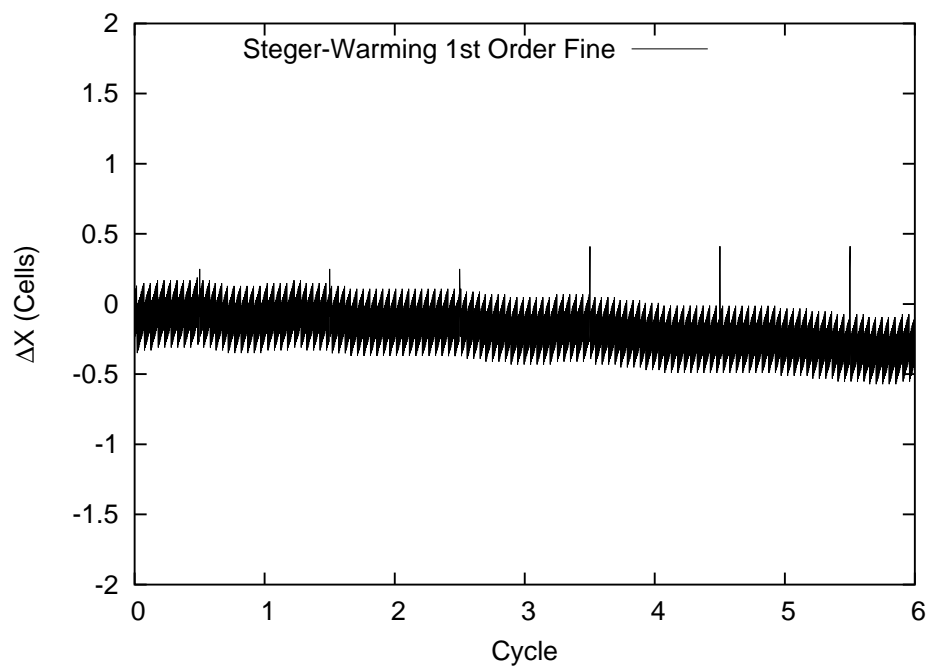


Figure 107: Cycle vs Δx - Steger-Warming - Fine Grid - 1st Order Temporal - Halved Time Step

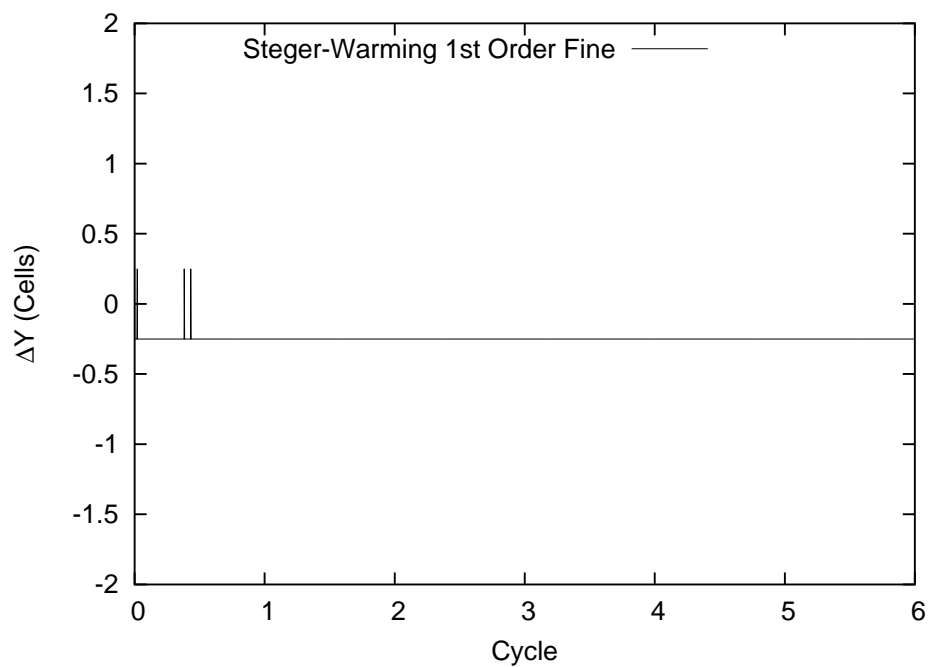


Figure 108: Cycle vs Δy - Steger-Warming - Fine - 1st Order Temporal - Halved Time Step

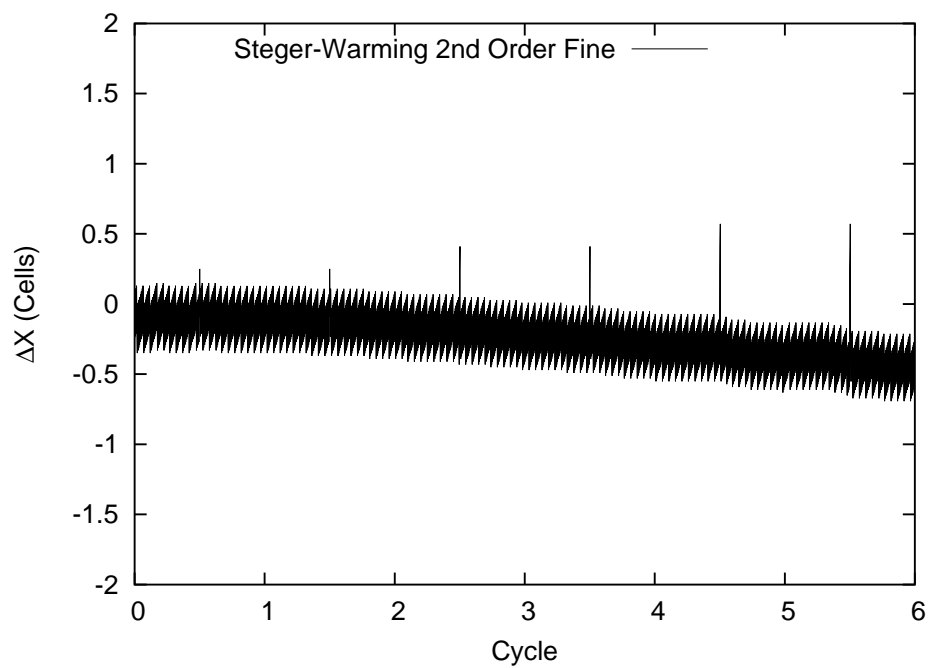


Figure 109: Cycle vs Δx - Steger-Warming - Fine - 2nd Order Temporal - Halved Time Step

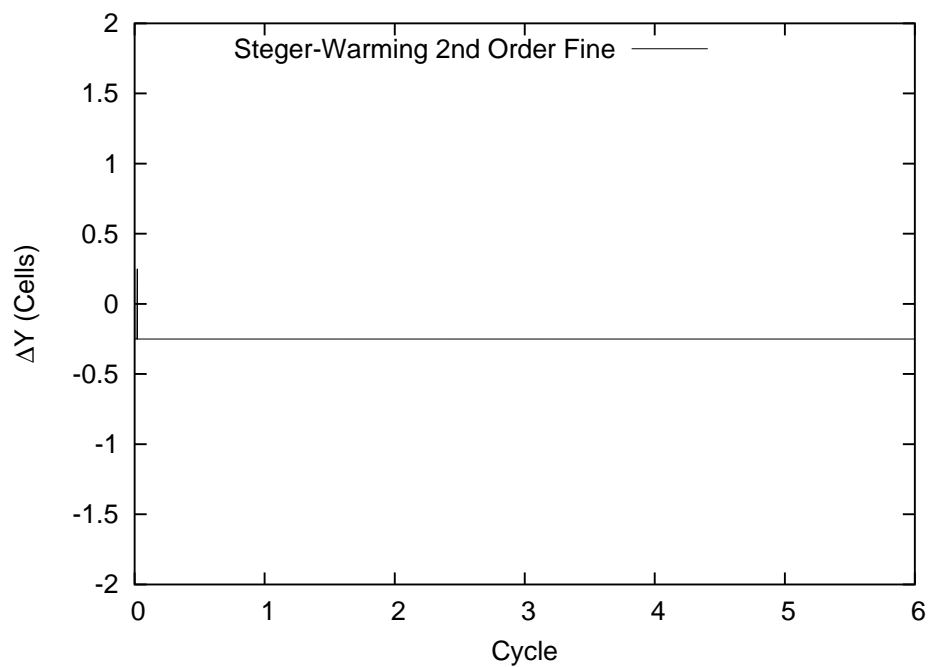


Figure 110: Cycle vs Δy - Steger-Warming - Fine Grid - 2nd Order Temporal - Halved Time Step

A.2 2D Vortex Shedding Cylinder

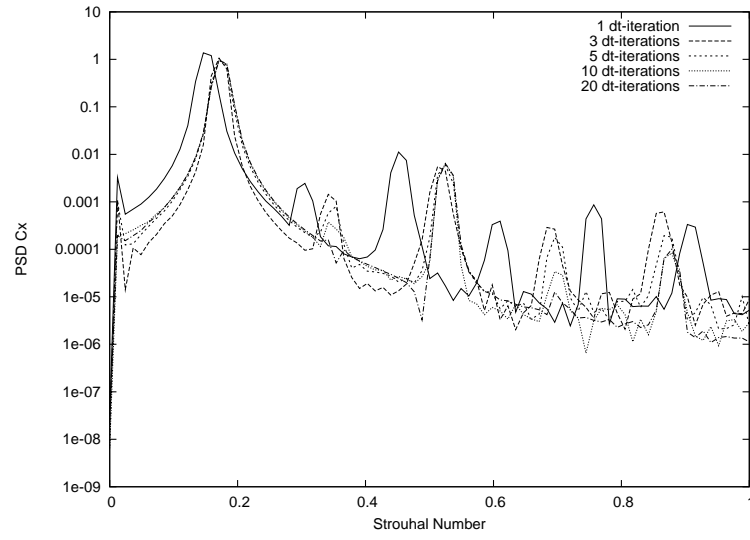


Figure 111: PSD of St for Lift - Roe - 1st Order Temporal

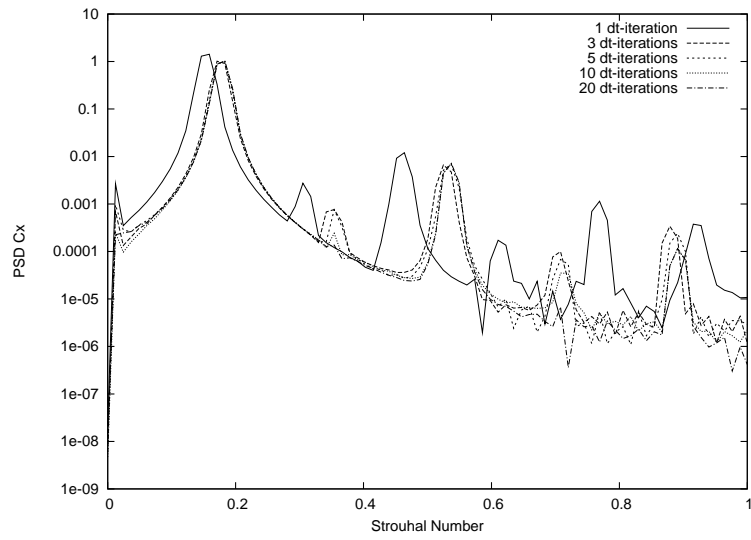


Figure 112: PSD of St for Lift - Roe - 2nd Order Temporal

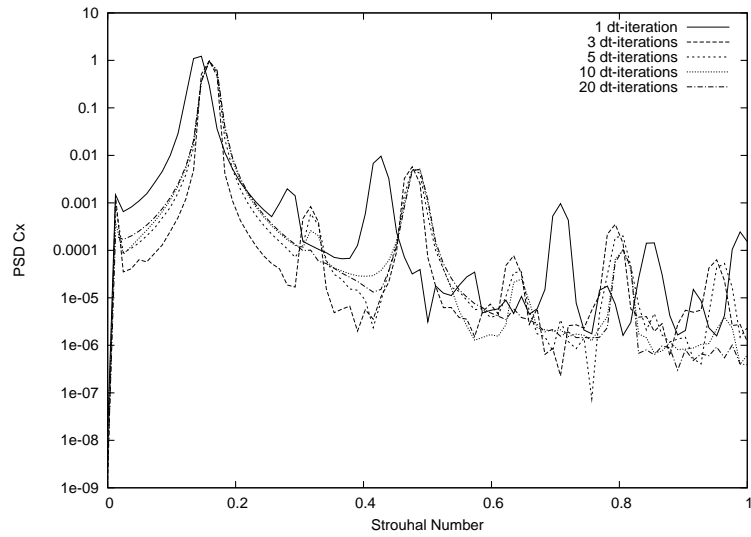


Figure 113: PSD of St for Lift - Steger-Warming - 1st Order Temporal

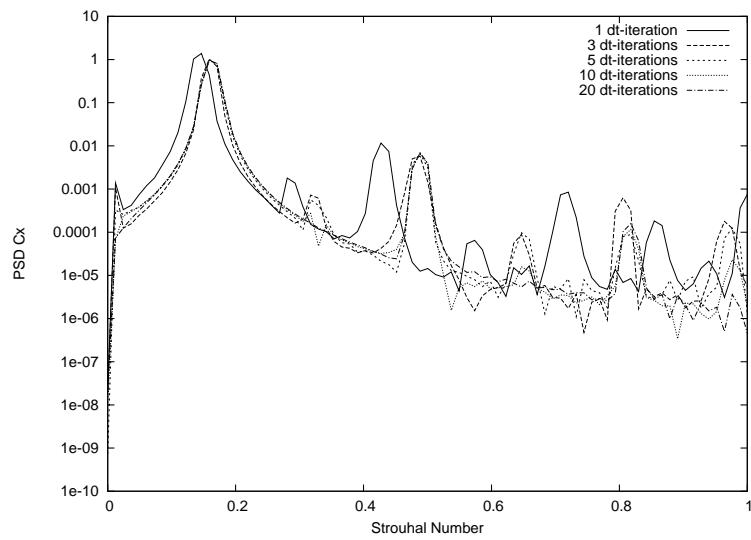


Figure 114: PSD of St for Lift - Steger-Warming - 2nd Order Temporal

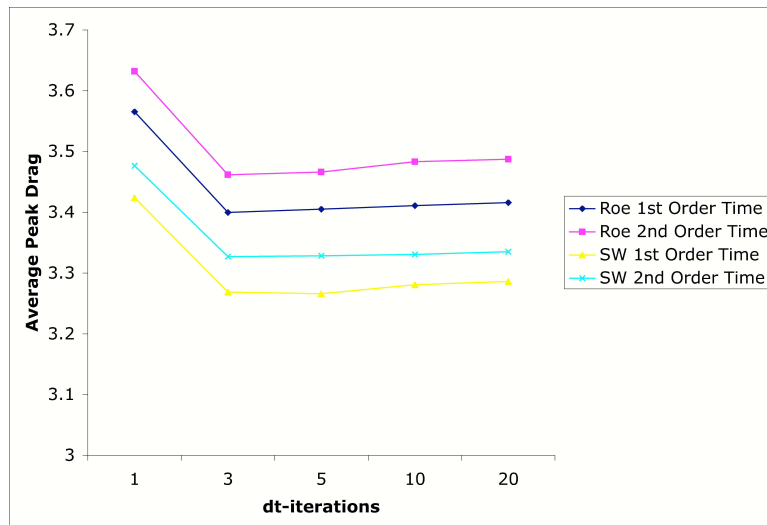


Figure 115: Average Peak Drag vs dt-iteration

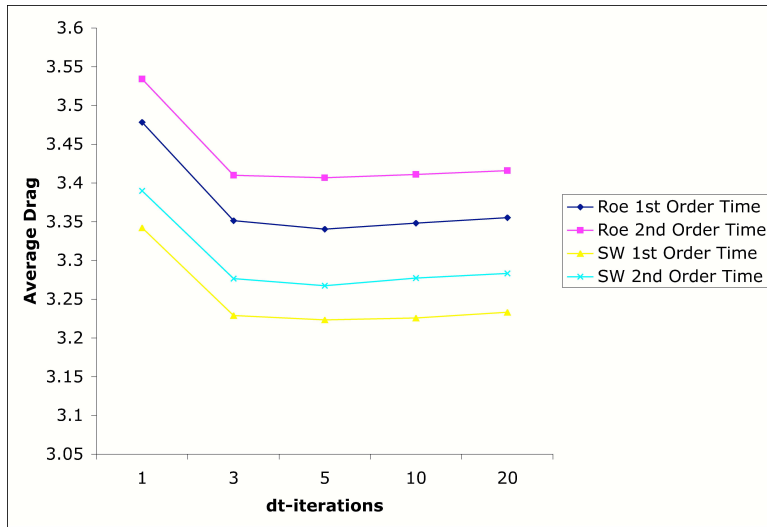


Figure 116: Average Drag vs dt-iteration

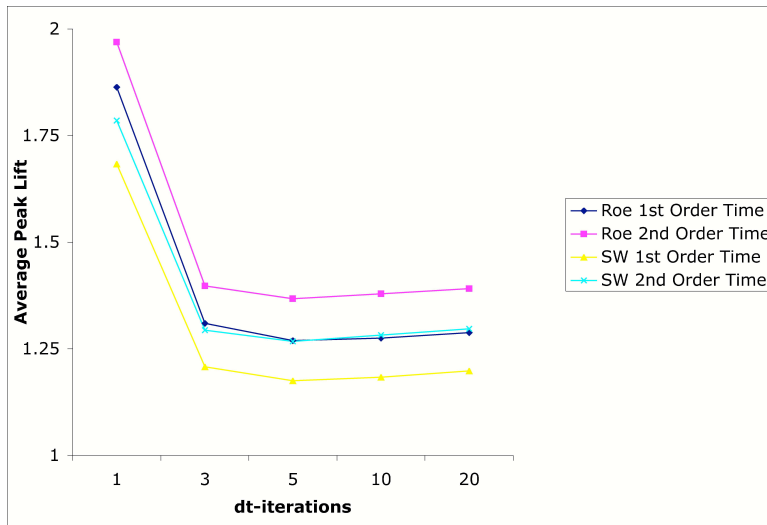


Figure 117: Average Peak Lift vs dt-iteration

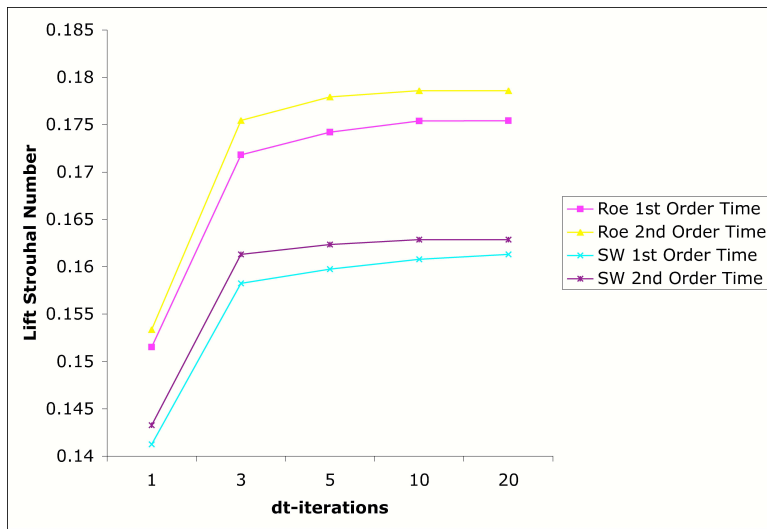


Figure 118: Average Strouhal Number from Lift vs dt-iteration

Appendix B. Results from Turbulent Cases

B.1 Turbulent Cavity

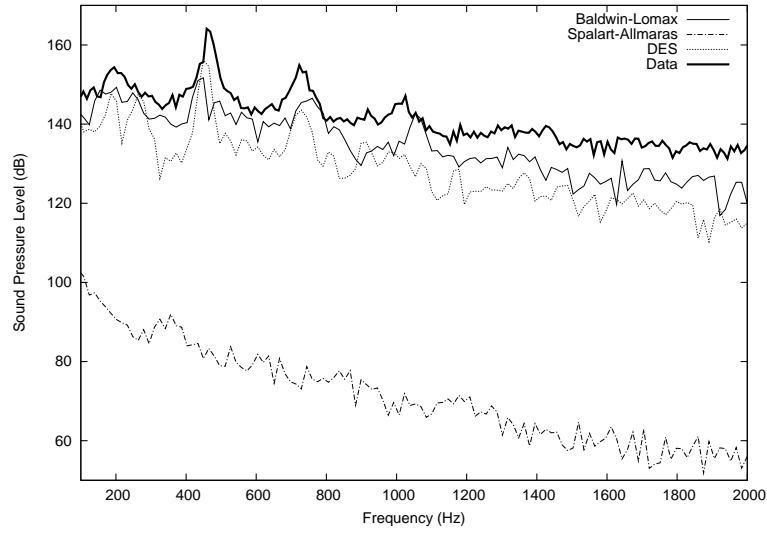


Figure 119: Sound Pressure Level Spectrum at the K16 Location - Coarse Grid

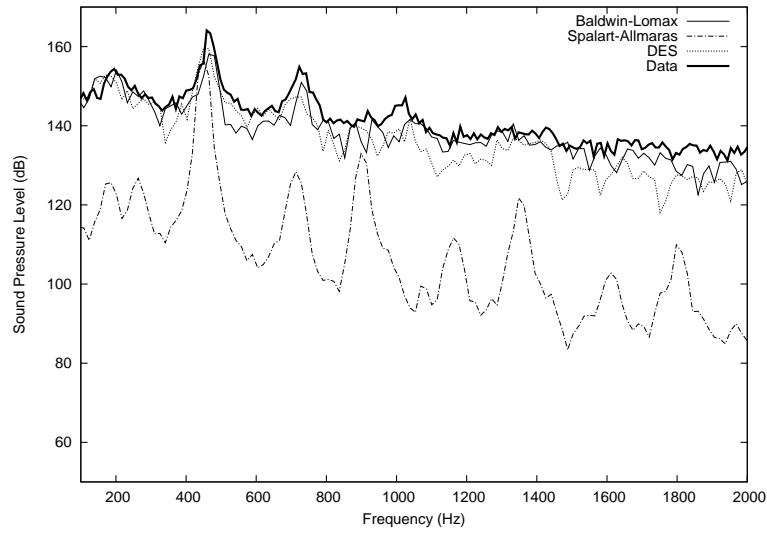


Figure 120: Sound Pressure Level Spectrum at the K16 Location - Medium Grid

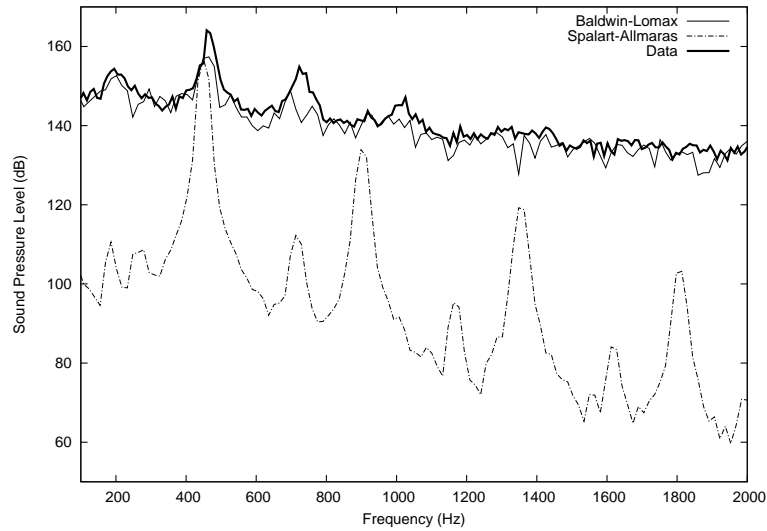


Figure 121: Sound Pressure Level Spectrum at the K16 Location - Fine Grid

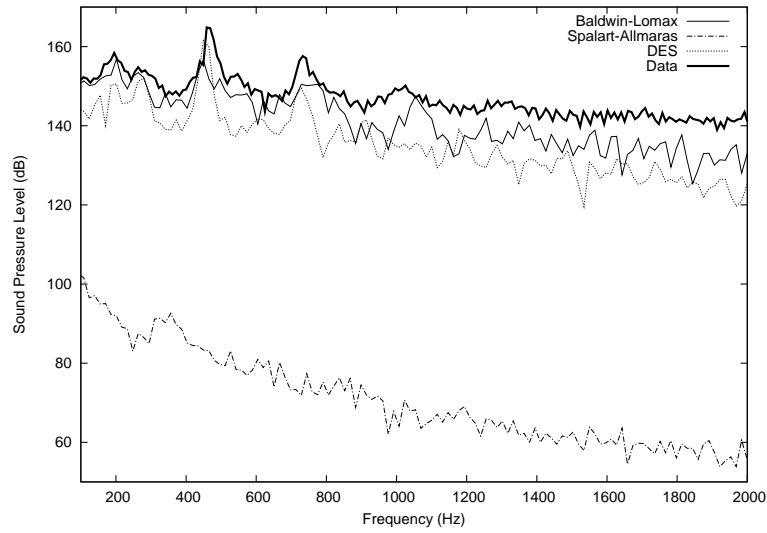


Figure 122: Sound Pressure Level Spectrum at the K18 Location - Coarse Grid

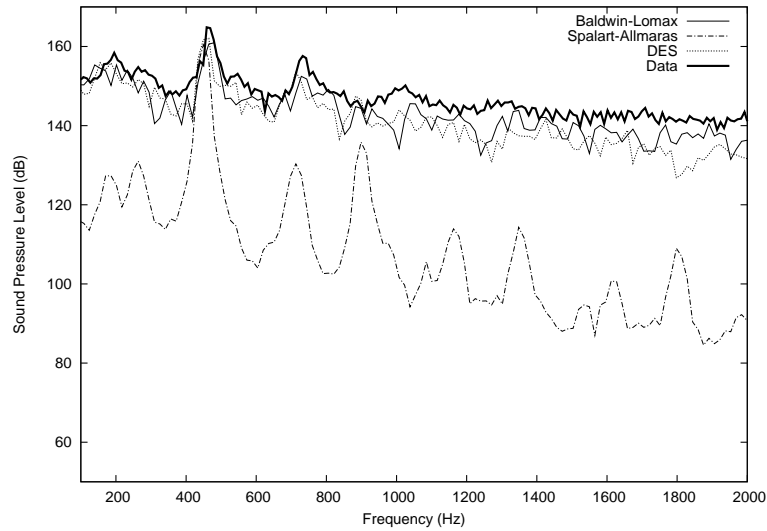


Figure 123: Sound Pressure Level Spectrum at the K18 Location - Medium Grid

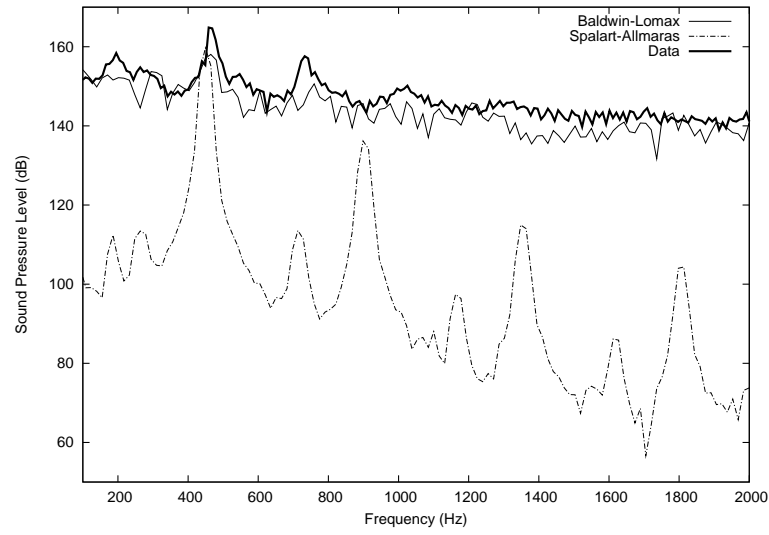


Figure 124: Sound Pressure Level Spectrum at the K18 Location - Fine Grid

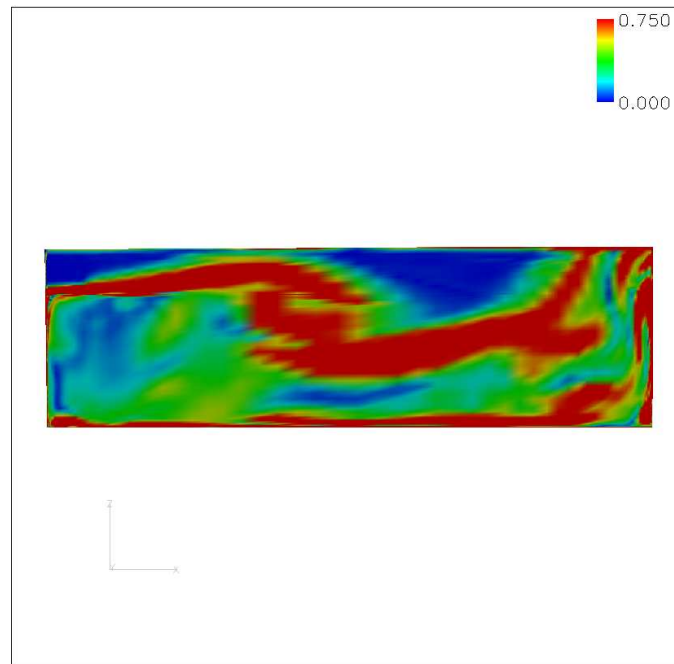


Figure 125: Vorticity - Baldwin-Lomax - Medium Cavity Grid

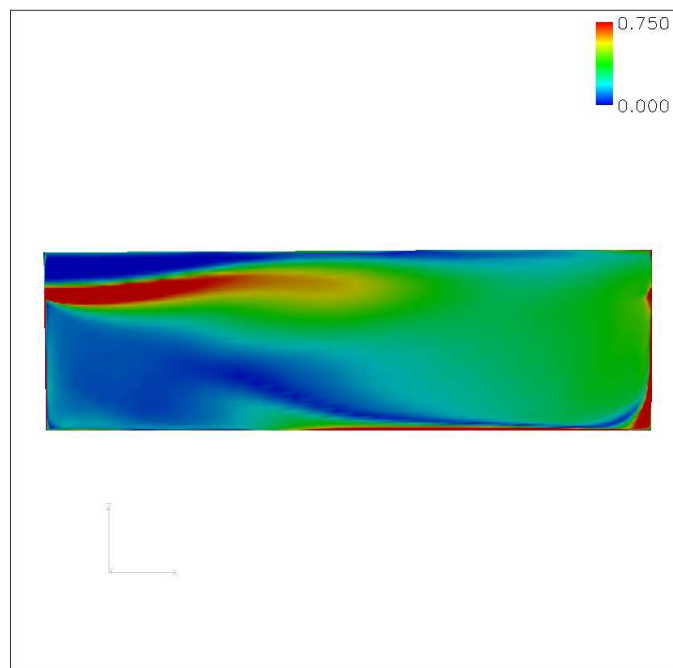


Figure 126: Vorticity - Spalart-Allmaras - Medium Cavity Grid

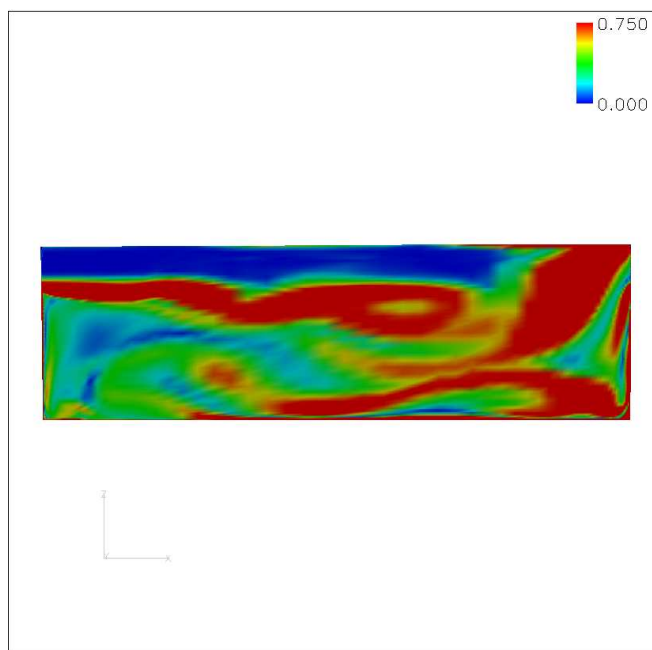


Figure 127: Vorticity - DES - Medium Cavity Grid

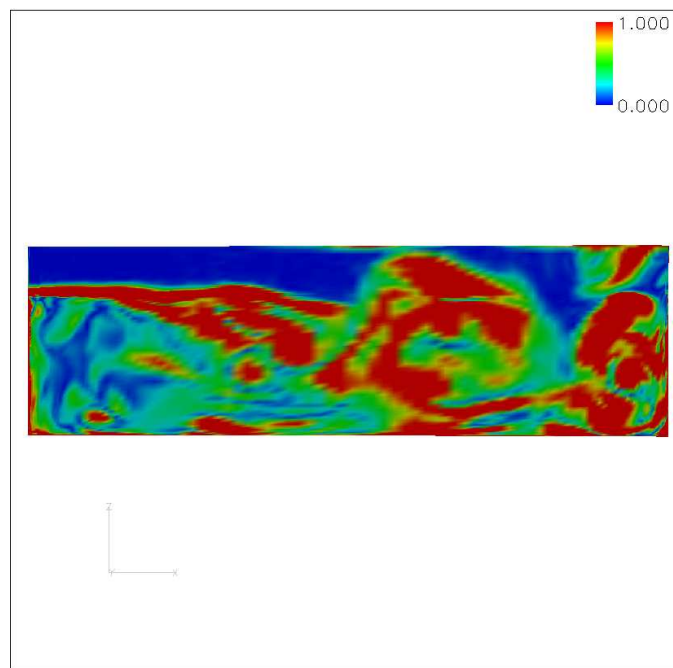


Figure 128: Vorticity - Baldwin-Lomax - Fine Cavity Grid

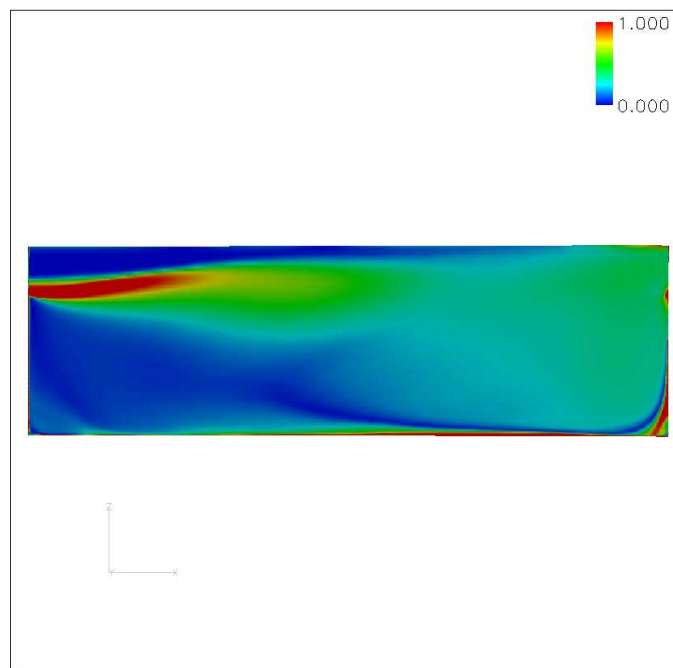


Figure 129: Vorticity - Spalart-Allmaras - Fine Cavity Grid

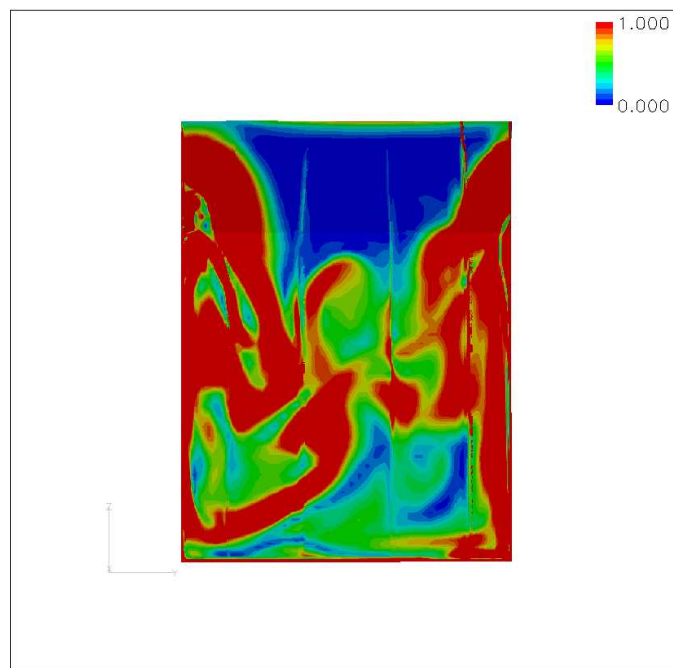


Figure 130: Vorticity - Baldwin-Lomax - Fine Cavity Grid - Front

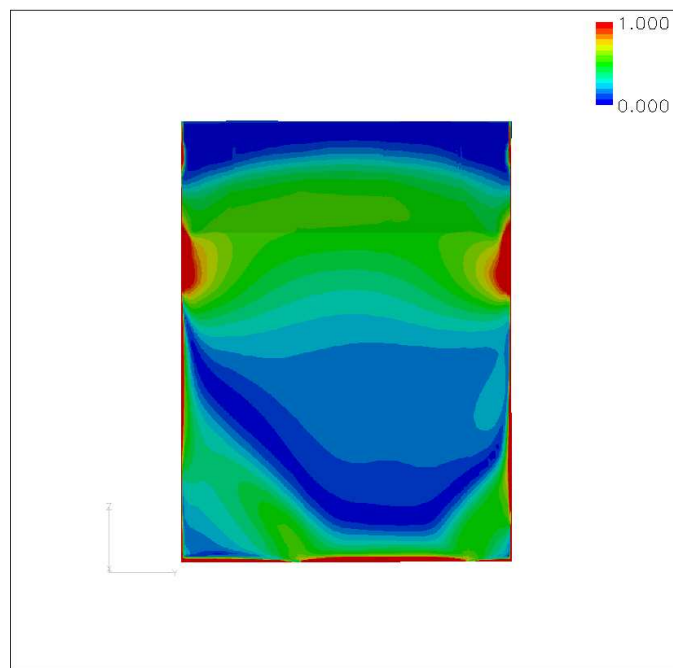


Figure 131: Vorticity - Spalart-Allmaras - Fine Cavity Grid - Front

Bibliography

1. Baldwin, B.S. and H. Lomax. "Thin Layer Approximation and Algebraic Model for Separated Turbulent Flows." *AIAA 16th Aerospace Sciences Meeting*. Number 78-257. AIAA, January 1978.
2. Blazek, J. *Computational Fluid Dynamics: Principles and Applications*. Elsevier, 2001.
3. Camelli, F. E. and R. Löhner. "Combining the Baldwin Lomax and Smagorinsky turbulence models to calculate flows with separated regions." *40th AIAA Aerospace Sciences Meeting & Exhibit*. Number 2002-0426. AIAA, January 2002.
4. Coleman, Larry A. and Bruce Jolly. "Numerical Simulation of a Store Separation Event From an F-15E Aircraft." *AIAA Atmospheric Flight Mechanics Conference*. Number 1996-3385. July 1996.
5. Dix, R.E. and R.C. Bauer. *Experimental and Theoretical Study of Cavity Acoustics*. Technical Report AEDC TR 99-4, May 2000.
6. Dunworth, Kevin S., et al. "CFD Investigation of Plastic Practice Bomb (PPB) Separation from F16/TER-9A Configuration." *21st AIAA Applied Aerodynamics Conference*. Number 2003-4224. June 2003.
7. Fluent Inc. *Fluent 5 Users Guide Volume 2*, July 1998.
8. Hoffmann, K.A. and S.T. Chiang. *Computational Fluid Dynamics Volume I*. Engineering Education System, 2000.
9. Hoffmann, K.A. and S.T. Chiang. *Computational Fluid Dynamics Volume III*. Engineering Education System, 2000.
10. Jones, G. W., et al. "Aerodynamic Forces on a Stationary and Oscillating Cylinder at High Reynolds Number." Number NASA-TR-R-300. October 1968.
11. Jr., James M. Brock and Bruce Jolly. "Application of Computational Fluid Dynamics at Eglin Air Force Base." *1998 World Aviation Conference*. Number 2000-0794. January 2000.
12. Keen, Joseph and Bruce Jolly. "Evaluation of CFD for Simulating a GBU-27 Separation From an F-15E Inboard Station." *AIAA Applied Aerodynamics Conference*. Number 1998-5500. September 1998.
13. Ko, Sungho and W.J. McCroskey. "Computations of Unsteady Separating Flows Over an Oscillating Airfoil." *33rd Aerospace Sciences Meeting and Exhibit*. Number 95-0312. January 1995.
14. Lee, J., et al. "Studies of Combined Use of CFD and Wind Tunnel Test Approaches to Simulate a Store Separation from F-15E Using Efficient CFD Database Generation." *22nd Applied Aerodynamics Conference and Exhibit*. Number 2004-4724. August 2004.
15. Maple, Raymond C. "AERO753 Class Notes." Air Force Institute of Technology, 2004.

16. Mathieu, Jean and Julian Scott. *An Introduction to Turbulent Flow*. Cambridge University Press, 2000.
17. Murman, Scott M. and Neal M. Chaderjian. "Application of Turbulence Models to Separated High-Angle-of-Attack Flows." Number 98-4519. AIAA, 1998.
18. Nelson, C.C. and R.H. Nichols. "Evaluation of Hybrid RANS/LES Turbulence Models Using an LES Code," *AIAA*, (2003-3552) (2003).
19. Nichols, B.H. *Turbulence Models and Their Application to Complex Flows*. Technical Report, Mississippi State University, 2002.
20. Nichols, R.H. "Development and Validation of a Two-Equation Turbulence Model with Wall Functions For Compressible Flow." *14th AIAA Applied Aerodynamics Conference*. June 1996.
21. Nichols, R.H. "Comparison of Hybrid RANS/LES Turbulence Models on a Circular Cylinder at High Reynolds Number," *AIAA*, (2005-0498) (2005).
22. Nichols, R.H. and B.D. Heikkinen. "Validation of Implicit Algorithms for Unsteady Flows Including Moving and Deforming Grids," *AIAA*, (2005-0683) (2005).
23. Nichols, R.H. and C.C. Nelson. "Application of Hybrid RANS/LES Turbulence Models." *41st Aerospace Sciences Meeting and Exhibit*. Number 2003-0083. January 2003.
24. Nichols, Robert. "Vortex Initial Q-file Generation Fortran Program."
25. Nichols, Robert H. "Validation of Hybrid RANS/LES Turbulence Models for Unsteady Flows." To Be Published.
26. Noack, Ralph W. and Bruce Jolly. "Fully Time Accurate CFD Simulations of JDAM Separation From an F-18C Aircraft." *38th Aerospace Sciences Meeting and Exhibit*. Number 2000-0794. January 2000.
27. Piziali, R.A. "2D and 3D Oscillating Wing Aerodynamics for a Range of Angles of Attack Including Stall." Number NASA TM 4632. September 1994.
28. Rizk, M. H. "The Use of Finite-Differenced Jacobians for Solving the Euler Equations and for Evaluating Sensitivity Derivatives." *Fluid Dynamics Conference*. Number 1994-2213. June 1994.
29. Rizk, M. H. "CFD Optimization by Sensitivity Derivatives Evaluated From Finite-Differenced Jacobians." *AIAA Computational Fluid Dynamics Conference*. Number 1995-1691. June 1995.
30. Rizk, Magdi, et al. "Beggart - A Store Separation Predictive Tool." *AIAA 32nd Fluid Dynamics Conference and Exhibit*. Number 02-3190. AIAA, June 2002.
31. Roe, P.L. "Approximate Riemann Solvers, Parameter Vectors, and Difference Schemes," *Journal of Computational Physics*, 43:357-372 (October 1981).
32. Séror, Stéphane, et al. "Implementation and Validation of the Spalart-Allmaras Turbulence Model for Parallel Processing on PC's Cluster," *AIAA*, (2003-3404) (2003).
33. Spalart, P. "Trends in Turbulence Treatments," *AIAA*, (2000-2306) (2000).

34. Spalart, P.R. and S.R. Allmaras. "A One-Equation Turbulence Model for Aerodynamic Flows." *AIAA 30th Aerospace Sciences Meeting*. Number 92-439. AIAA, January 1992.
35. Srinivasan, G.R., et al. "Evaluation of Turbulence Models for Unsteady Flows of an Oscillating Airfoil," *Computers and Fluids*, 24(7):833–861 (1995).
36. Steger, Joseph L and R.F. Warming. "Flux Vector Splitting of the Inviscid Gasdynamic Equations with Application to Finite-Difference Methods," *Journal of Computational Physics*, 40:263–293 (April 1981).
37. Suhs, N.E. "Unsteady Flow Computations for a Three-Dimensional Cavity With and Without an Acoustic Suppression Device." Number 93-3402. AIAA, 1993.
38. Swanson, R.C. and E. Turkel. *Multistage Schemes With Multigrid for Euler and Navier-Stokes Equations*. Technical Report 3631, NASA, August 1997.
39. Tannehill, J.C. Anderson, D.A. and R.H. Pletcher. *Computational Fluid Mechanics and Heat Transfer*, chapter 5. Taylor & Francis, 1997.
40. Versteeg, H.K. and W. Malalasekera. *An introduction to Computational Fluid Dynamics: The Finite Volume Method*. Prentice Hall, 1995.
41. Visbal, M.R. and D.V. Gaitonde. "High-Order-Accurate Methods for Complex Unsteady Subsonic Flows," *AIAA Journal*, (37):1231–1239 (1999).
42. Westmoreland, Shawn. "A Comparison of Inviscid and Viscous Approaches for Store Separations." *20th AIAA Applied Aerodynamics Conference*. Number 2002-1413. June 2002.
43. White, F.M. *Viscous Fluid Flow* (Second Edition), chapter 1. McGraw Hill, 1991.
44. Whitfield, David L. and L. K. Taylor. "Discretized Newton-Relaxation Solution of High Resolution Flux-Difference Split Schemes." *AIAA Paper*. Number 91-1539. AIAA, June 1991.
45. Wilcox, D. "Turbulence Modeling: An Overview." *AIAA 39th Aerospace Sciences Meeting*. Number 0724 in 2001. AIAA, January 2001.
46. Wilcox, D.C. *Turbulence Modeling for CFD. 2nd Ed.*. DCW Ind., 1998.
47. Yoder, D. and N. Georgiadis. "Implementation and Validation of the Chien k- ϵ Turbulence Model in the WIND Navier-Stokes Code," *NASA/TM*, (209080) (1999).

Vita

Kevin Gregory Storm graduated from Waterford Union High School in Waterford, Wisconsin, and then attended the University of Wisconsin - Madison in Madison, Wisconsin. He was commissioned as a second lieutenant on 18 May 2003. Immediately after graduation from the University of Wisconsin he was assigned to the Air Force Institute of Technology where he earned the degree of Master of Science in Aeronautical Engineering in March 2005. Upon graduation, he was assigned to Space and Missile Systems Center, Los Angeles Air Force Base, California.

Permanent address: 2950 Hobson Way
Air Force Institute of Technology
Wright-Patterson AFB, OH 45433

REPORT DOCUMENTATION PAGE					Form Approved OMB No. 0704-0188	
The public reporting burden for this collection of information is estimated to average 1 hour per response, including the time for reviewing instructions, searching existing data sources, gathering and maintaining the data needed, and completing and reviewing the collection of information. Send comments regarding this burden estimate or any other aspect of this collection of information, including suggestions for reducing this burden to Department of Defense, Washington Headquarters Services, Directorate for Information Operations and Reports (0704-0188), 1215 Jefferson Davis Highway, Suite 1204, Arlington, VA 22202-4302. Respondents should be aware that notwithstanding any other provision of law, no person shall be subject to any penalty for failing to comply with a collection of information if it does not display a currently valid OMB control number. PLEASE DO NOT RETURN YOUR FORM TO THE ABOVE ADDRESS.						
1. REPORT DATE (DD-MM-YYYY) 21-03-2005		2. REPORT TYPE Master's Thesis			3. DATES COVERED (From — To) Sept 2003 — Mar 2005	
4. TITLE AND SUBTITLE Validation of Turbulence Models in the Beggar Code for Unsteady Flow					5a. CONTRACT NUMBER 5b. GRANT NUMBER 5c. PROGRAM ELEMENT NUMBER	
6. AUTHOR(S) Storm, Kevin G., 2Lt, USAF					5d. PROJECT NUMBER 2004-060 5e. TASK NUMBER 5f. WORK UNIT NUMBER	
7. PERFORMING ORGANIZATION NAME(S) AND ADDRESS(ES) Air Force Institute of Technology Graduate School of Engineering and Management 2950 Hobson Way WPAFB OH 45433-7765					8. PERFORMING ORGANIZATION REPORT NUMBER AFIT/GAE/ENY/05-M22	
9. SPONSORING / MONITORING AGENCY NAME(S) AND ADDRESS(ES) 46 SK/SKE Capt Jacob Freeman 205 West D. Avenue, Suite 348 Eglin Air Force Base, FL 32542					10. SPONSOR/MONITOR'S ACRONYM(S) 11. SPONSOR/MONITOR'S REPORT NUMBER(S)	
12. DISTRIBUTION / AVAILABILITY STATEMENT Approval for public release; distribution is unlimited.						
13. SUPPLEMENTARY NOTES						
14. ABSTRACT Validation of the turbulence models in the CFD code Beggar for unsteady turbulent flow are discussed. Six validation cases of the code are considered, three cases with the intent of validating the code without the turbulence model and three cases to validate the turbulence model itself. Finally, a more realistic simulation of a simplified store is examined. The turbulence models considered are the Baldwin-Lomax, Spalart-Allmaras, and a DES model. The conclusions made deal with necessary prerequisites to properly simulating unsteady turbulent flow and model selection. The prerequisites necessary in the Beggar code are a second order temporal discretization and the calculation of at least three Newton dt-iterations per time step. Baldwin-Lomax overpredicts unsteady effects. The Spalart-Allmaras model was found to not properly simulate unsteady turbulent flow and is possible written incorrectly in Beggar. A recommendation of whether to use the DES model or not cannot be made due to time and computational constraints and temporary problems within the Beggar code.						
15. SUBJECT TERMS Beggar, CFD, Turbulence Model, Validation, Spalart-Allmaras, Baldwin-Lomax						
16. SECURITY CLASSIFICATION OF:			17. LIMITATION OF ABSTRACT		18. NUMBER OF PAGES	
a. REPORT U	b. ABSTRACT U	c. THIS PAGE U	 UU		 148	
					19a. NAME OF RESPONSIBLE PERSON LtCol Raymond Maple	
					19b. TELEPHONE NUMBER (include area code) (937) 255-3636, ext 4577	